

UC Davis

UC Davis Electronic Theses and Dissertations

Title

Longitudinal Beam Structure Simulations with Impedance Studies and Ferrite Characterization for the Mu2e Experiment

Permalink

<https://escholarship.org/uc/item/0qt0390p>

Author

Harrig, Keegan

Publication Date

2024

Peer reviewed|Thesis/dissertation

Longitudinal Beam Structure Simulations with Impedance Studies and
Ferrite Characterization for the Mu2e Experiment

By

KEEGAN PEARL HARRIG

DISSERTATION

Submitted in partial satisfaction of the requirements for the degree of

DOCTOR OF PHILOSOPHY

in

Physics

in the

OFFICE OF GRADUATE STUDIES

of the

UNIVERSITY OF CALIFORNIA

DAVIS

Approved:

Eric Prebys, Chair

Robert Svoboda

Robin Erbacher

Committee in Charge

2024

Copyright © 2024 by
Keegan Pearl Harrig
All rights reserved.

CONTENTS

List of Figures	v
List of Tables	xiii
Abstract	xiv
Acknowledgments	xv
1 Introduction	1
2 Charged Lepton Flavor Violation	5
2.1 Theory Overview	5
2.1.1 $\mu^+ \rightarrow e^+\gamma$	13
2.1.2 $\mu^+ \rightarrow e^+e^+e^-$	14
2.1.3 $\mu^- N \rightarrow e^- N$	15
2.2 Limitations of Previous Experiments and Driving Consideration for Mu2e	16
3 Mu2e Experiment	18
3.1 Backgrounds	19
3.1.1 Decay In Orbit	19
3.1.2 Radiative Pion Capture	20
3.1.3 Decay in Flight	21
3.1.4 Antiproton	21
3.1.5 Cosmic Ray	22
3.2 Solenoids and Detectors	22
3.2.1 Production Solenoid and Target	24
3.2.2 Transport Solenoid	25
3.2.3 Detector Solenoid and Target	27
3.2.4 Tracker and Calorimeter	28
3.2.5 Stopping Target Monitor	29
3.2.6 Cosmic Ray Veto	30

4	Quick Primer in Accelerator Physics	31
4.1	Transverse Motion	31
4.1.1	Thin Lens Quadrupole	32
4.1.2	Equation of Motion	34
4.1.3	Closed Form Solution	36
4.2	Longitudinal Motion	40
4.2.1	Impedance	40
4.2.2	RF Cavities	41
4.2.3	Equation of Motion	43
4.2.4	Particle Trajectories	46
5	Mu2e and the Fermilab Accelerator Complex	48
5.1	Fermilab Accelerator Complex	49
5.1.1	Ion source, Preaccelerator and Linac	50
5.1.2	Booster	52
5.1.3	Recycler Ring	53
5.1.4	Delivery Ring	54
5.1.5	M4 Beamline	56
6	Extinction	58
6.1	Bunch Formation	59
6.2	Beam Line Extinction	61
7	AC Dipole	63
7.1	Extinction System	63
7.1.1	AC Dipole Design	65
7.1.2	Prototypes	68
8	Ferrite Characterization	72
9	BLoND Simulations	79
9.1	Current State	79

9.2	Simulations	83
9.2.1	Frequency Mismatch	84
9.2.2	Impedance and Space Charge	86
9.3	M4DA Direct Measurement	91
10	Conclusion	94

LIST OF FIGURES

2.1	Λ as a function of κ for a muon to electron conversion experiment with a sensitivity in the range of $10^{-16} - 10^{-17}$ is compared to that for a $\mu \rightarrow e\gamma$ experiment with a sensitivity in the range of $10^{-13} - 10^{-14}$. The current and projected exclusion regions of parameter space for $\mu \rightarrow e\gamma$ are indicated by red contours, those for $\mu \rightarrow e$ conversion by blue contours.	11
2.2	Feynman diagrams describing the SINDRUM II and MEG experiments parameter space, highlighted in blue and red in Figure 2.1. These shaded regions are the extremes of the parameter space.	12
2.3	General Feynman diagrams describing higher order loop and tree level diagrams.	12
2.4	Feynman diagram of $\mu^+ \rightarrow e^+\gamma$ via neutrino mixing.	12
2.5	Feynman diagram of $\mu^+ \rightarrow e^+\gamma$ via SUSY.	13
2.6	Feynman diagrams for the $\mu^+ \rightarrow e^+e^+e^-$ decay in different theoretical models[1].	14
2.7	Diagram of the recoiling nucleus, captured muon and the mono-energetic electron produced in the Mu2e experiment. The energy of the electron can be calculated exactly and results in a very clean experimental signature. .	15
3.1	Sensitivity as a function of year, each data point represents an experiment, past or projected [2].	18
3.2	Decay-in-orbit electron spectrum in aluminum near the endpoint, normalized to the free-muon decay rate Γ_0 . The left-hand plot is on a linear scale, the right a logarithmic one [3].	20
3.3	Histogram of the tail of the DOI spectrum overlaid with the expected conversion signal for the given statistics as a function of particle momentum [4].	20

3.4	The Mu2e beam timing. Shown here are the time distributions for the following processes: pions and muons arriving at the detector solenoid and the decay or capture time of said muons. The “Selection window” is the period of time for which Mu2e will analyze data, the live gate will take data as early as about 500 ns, with the final accepted region determined through analysis [5].	21
3.5	Pulse structure required by the Mu2e Experiment. The requirement that there be no protons outside of the nominal pulse width above the 10^{-10} fractional level is referred to as “Extinction” [6].	23
3.6	Cartoon of the solenoid layout and magnetic field strengths in Tesla for the Mu2e experiment. The Production Solenoid reverses direction of pions and some muons and cuts out electrons, neutrons and photons that would otherwise overwhelm the Mu2e detectors. The Transport Solenoid allows pions time to decay, reducing the RPC background. High momentum muons run into the walls of the TS and the positive muons are reduced using a collimator system. The Detector Solenoid carefully deflects conversion electrons into the tracker while allowing harmful backgrounds to pass through to a beam dump [2].	24
3.7	The Mu2e target area and components in relation to the M4 beamline and the TS [2].	25
3.8	The Mu2e Transport Solenoid [7].	26
3.9	A zoomed in section of the Transport Solenoid with a selection collimator. μ^- paths are shown in red and μ^+ are shown in blue [7].	27
3.10	Rough illustration of the stopping target. 37 100 μm thick aluminum foils with a hole in the center large enough to allow electrons with momentum $< 53 \text{ MeV}/c$ to pass through untouched [2].	28
3.11	Schematic of the tracker. The red and blue portions are the straw tubes and the circles represent the area in which Mu2e expects to see a signal for given electron energies [8].	29

3.12	The Mu2e CRV system with neutron rates as seen by the counters [2]. . .	30
4.1	Coordinate system for a particle following the ideal path around a circular accelerator assuming a homogeneous dipole field [9].	32
4.2	Convex lens with focal length f , bending a light ray initially parallel to the optical axis [10].	33
4.3	An ellipse in transverse phase space of the coordinate x . Courant-Snyder parameters can be used to parametrize the ellipse.	39
4.4	Longitudinal focusing of beam particles depending on their position relative to the center of the non-conducting gap indicated by the yellow rectangle in the top image. Proton A is decelerated and proton C is accelerated, effectively condensing the beam in the longitudinal direction [6].	42
5.1	Fermilab accelerator complex.	49
5.2	FNAL Magnetron schematic (left) and actual installation (right). The cathode runs down the central axis of the anode [11].	51
5.3	Cutout of a four-pole RFQ.	51
5.4	Close up of the RFQ vane tip with the longitudinal component of the electric field indicated by E_z	52
5.5	Picture of the Debuncher (outer ring) and the Accumulator (inner ring) [12].	54
5.6	Schematic of the electrostatic septum. The beam is shown in red and the cathode is held at -100 kV [13].	55
5.7	Transverse beam line optics as simulated by MADX for the M4 line Where β is the beta function and D is the dispersion function. FF is the final focus area [4].	56
5.8	Physical layout of the beam line components in the M4 beamline. $\Delta\mu_x$ is the horizontal betatron phase [6].	57
5.9	Pulse structure required by the Mu2e Experiment. The requirement that there be no protons outside of the nominal pulse width above the 10^{-10} fractional level is referred to as “Extinction” [6].	57

6.1	Simulated Recycler 2.5 MHz bunch in longitudinal phase space at the time of the last extraction. Each color corresponds to a 53 MHz bunch from the Booster. The dotted lines indicate the ± 125 ns window defining in-time beam [6].	59
6.2	Simplistic view of a charged particle passing through a shaped cavity with electromagnetic field lines [14].	60
6.3	Time profile of the AC dipole field overlaid with the expected proton pulses separated by $1.7 \mu\text{s}$. The excitation of the AC dipole is achieved by sine waves at 300 kHz and 4.4 MHz [6].	61
7.1	The phase space effects of the extinction system [6].	64
7.2	Effects of the AC Dipole in the bend plane phase space, where x' is the derivative of x as described in Section 4.1.3. The beam line admittance is indicated by the ellipse [15].	64
7.3	Normalized deflection amplitude as a function of time. The solid green line indicates the amplitude corresponding to total extinction, Equation 7.1, and the dotted green line indicates half this deflection. The black line represents a close up view at the zero crossing of the dual harmonic waveform used as the excitation [16].	65
7.4	Beam optics in the region of the AC dipole and collimator [15].	67
7.5	Technical drawings of the AC Dipole prototype with (a) and without (b) the vacuum box. The four copper tubes on either side of the box act as the magnet coil and the water leads that cool the ferrites inside the box [17].	68
7.6	Beam-eye view of the AC Dipole prototype interior. The ferrites are in blue, the gap is 1.8 cm [17].	69
7.7	Volumetric loss density in Watts per cubic meter at 300 kHz as function of length in the one-meter magnet prototype simulation [18].	70
7.8	Magnetic flux density in Gauss as function of length at 300 kHz in the one-meter magnet prototype simulation [18].	71

7.9	The real part of the measured permeability as a function of field strength for three different ferrite samples. The color coordinated dotted lines represent the lines through which the permeability may intersect only once [18].	71
8.1	Circuit diagram for ferrite characterization.	72
8.2	Overview of “dipole mode” circuit setup for ferrite characterization. A voltage, and two current probes in conjunction with an oscilloscope are used to measure the voltage across the capacitor bank, the current through the copper coil and the current into the circuit respectively.	73
8.3	Dipole mode losses at 300 kHz, with 26.4 nF capacitance. The bricks were measured in groups of four and an labeled by their manufacturing number and date measured. At the field strength required by the magnet the ferrites will experience losses $\sim 15.000 \text{ W/m}^3$	74
8.4	Dipole mode losses at 4.4 MHz, with 68 pF capacitance. The bricks were measured in groups of four and an labeled by their manufacturing number and date measured. At the field strength required by the magnet the ferrites will experience losses $\sim 1.000 \text{ W/m}^3$	75
8.5	Measurement apparatus that is used in toroid mode measurements. The ends of the litz wire were stripped and coated in solder for connection to the capacitor bank; which is located along with the current and voltage probes at the front of the apparatus.	76
8.6	Sample of loss measurements at 300 kHz. The bricks were measured in groups of two in “toroid mode” and labeled by their manufacturing number. The reference brick was number 9. These measurements are in agreement.	77
8.7	Sample of loss measurements at 4.4 MHz. The bricks were measured in groups of two in “toroid mode” and an labeled by their manufacturing number. The reference brick was number 9. These measurements are in agreement.	77

8.8	Sample of magnetic permeability measurements at 300 kHz. The bricks were measured in groups of two in “toroid mode” and are labeled by their manufacturing number. The flat almost concave shape clearly satisfies the stability criterion previously described in Section 7.1.2.	78
9.1	8 bunches are extracted from the DR and then injected into the g-2 storage ring. The plots above show the time profile of these 3 GeV muon bunches just before they enter the storage ring as measured by the T0 detector. The detector consists of a scintillator attached to two vertically aligned PMTs. The y-axis is the PMT amplitude on log scale. The logarithmic scale better shows the magnitude of the out-of-time beam, which is indicated by the counts lying outside of the vertical dotted lines in each histogram. Each histogram has 11 traces overlaid [19] [20].	81
9.2	The T0 detector location. Just before entering the g-2 storage ring the muons will encounter the T0 detector [19].	82
9.3	Diagram of the T0 detector [21]. Particles entering the ring pass through the scintillator (in green). Light guides on either side of the scintillator transport the scintillation light to the PMTs on each end.	82
9.4	Picture of the T0 detector [21].	83
9.5	Waterfall plot showing the longitudinal time profile and intensity of proton bunches in the Recycler over time. Two batches consisting of four bunches each are present as well as additional “ghost” bunches that can be seen bordering Batch 2. While this bunch structure is satisfactory for g-2, it could potentially be detrimental to Mu2e [6].	83
9.6	Re-bunching sequence of the Recycler [6].	84
9.7	Initial distribution for input into the BLonD simulation of the Recycler. The green window depicts a zoomed in view of one 2.5 MHz bucket, the separatrix of which is drawn in red, where the individual 53 MHz Booster bunches can be discerned.	85

9.8	A view of the simulated eighth bunch in the Recycler in longitudinal phase space after the re-bunching sequence has been executed. In longitudinal phase space protons tend to rotate about the center of the RF bucket. Rotation near the center of the bucket is faster than that the near the edge of the bucket. This gives rise to a filamenting of the beam in longitudinal phase space as the beam makes repeated revolutions around the bucket. This filamenting is clearly visible in the above plot.	86
9.9	Circuit model for RF cavity including beam effects. The cavity presents itself as an RLC circuit that is excited by both the RF drive current (I_g) and the current induced by the beam (I_b). The shunt impedance of the cavity is characterized by an inductance, capacitance, and resistance given by L_s , C_s , and R_s respectively. For excitations at the resonant frequency the cavity impedance is only the resistance with $R_s = 84\text{ k}\Omega$ for 53 MHz. V_c is the resultant voltage across the cavity [6].	88
9.10	A simulation using BLoND of the re-bunching sequence in the Recycler with no space charge or impedance effects included. The y-axis is the number of turns through the Recycler, the x-axis is the longitudinal time coordinate and the z-axis is the number of protons. The z-axis on the right plot is on log scale and the left has a linear scale. Ghost bunches can be seen on either side of each batch which consists of 4 bunches.	89
9.11	A simulation using BLoND of the re-bunching sequence in the Recycler with space charge and impedance effects included. Impedance was calculated using $6\times$ the shunt resistance. The y-axis is the number of turns through the Recycler, the x-axis is the longitudinal time coordinate and the z-axis is the number of protons. The z-axis on the right plot is on log scale and the left has a linear scale. Ghost bunches can be seen on either side of each batch which consists of 4 bunches.	89

9.12	Histograms comparing the longitudinal time profile of the eighth bunch just prior to extraction. The y-axis has units of counts per 2 ns bin. As the impedance is increased, the irregular profile of the beam as well as increasing out-of-time beam are apparent.	90
9.13	Location of the M4 diagnostic absorber (M4DA) relative to the M4 line, which contains the extinction components including the AC Dipole [13]. .	92
9.14	The Upstream Extinction Monitor (UEM) prototype arm with mounted PMTs attached to quartz crystals [13].	93
9.15	Pictures of the detector setup that include a quartz crystal in Figure (a) and PMT with metallic housing and quartz crystal mount on an endcap in Figure (b).	93

LIST OF TABLES

8.1	Two-brick toroid mode setup dimensions.	78
9.1	Recycler 53 MHz shunt impedance with Q correction [22].	88

ABSTRACT

Longitudinal Beam Structure Simulations with Impedance Studies and Ferrite Characterization for the Mu2e Experiment

I present extinction beam studies, simulation and characterization of ferrite material in aid of the commissioning of the Extinction system for the Mu2e experiment. Mu2e will search for the neutrinoless-conversion of a stopped muon to an electron in the field of a nucleus with never before seen sensitivity. The background level required for a single-event-sensitivity of 3×10^{-17} is 10^{-10} , meaning out-of-time particles on the production target must be at or below this fractional level (extinction level) to achieve the experimental goal. Presented here is work on the design and evaluation process of the novel AC Dipole magnet responsible for the majority of the extinction process, with special focus on the loss characterization process of the ferrite material used. Longitudinal beam structure and impedance studies with the Beam Longitudinal Dynamics (BLonD) simulation framework for the Mu2e experiment are also presented here, along with corroborating beam studies.

ACKNOWLEDGMENTS

Words cannot express my gratitude to my professor, Eric Prebys for his continued support and patience, and for giving me the opportunity to carry out my research under his supervision. His guidance and advice, alongside with his invaluable research experience, provided me with the motivation and inspiration to accomplish this work. I am forever indebted to my mentor at Fermilab, Steve Werkema, for shepherding me through my time at Fermilab and allowing me to participate in this research. His unwavering kindness and priceless experience in leadership and research have empowered me to complete the work presented here and will no doubt continue to inspire me throughout my career. Additionally, this endeavor would not have been possible without the generous support from Luciano Elementi, Howard Pfeffer, and the entirety of the AC Dipole group at Fermilab for allowing me to work on this project and sharing their love of science and teamwork with me. I am also forever indebted to Robert Ainsworth and Robert Kutschke for taking time to get me started using computing resources and for introducing to me to the simulation framework presented here. I also owe a huge thanks to Robert Zawaska and all the committee members of the Fermilab PhD program who have allowed me to work on this project and have played a large role in enabling my success as a graduate student. I also could not have undertaken this journey without my thesis committee, who generously provided knowledge and expertise. And a special thanks to Brendan Casey and the g-2 experiment for allowing me to use their analysis and data from the g-2 T0 detector.

I am also grateful to my classmates and cohort members, for their unconditional moral support. And special thanks to my partner for coming on this journey with me and supporting me through the tough times.

Lastly, I would be remiss in not mentioning my family, especially my parents. Their belief in me has kept my spirits and motivation high during this process. I would also like to thank my two cats for all the entertainment and emotional support.

Chapter 1

Introduction

Since Röntgen's use of a cathode ray tube to discover x-rays in 1895 and Lawrence's construction of the first Cyclotron in 1930, the artificial acceleration of particles has been a fundamental tool for probing the governing principles that make up our universe. This is because accelerators can achieve energy, pressure, time and spatial resolutions that no other experimental tool can approach. Circular accelerators such as the Tevatron, LEP and HERA have been used to establish perhaps the most successful theory in physics today, the Standard Model (SM) [23]. A more recent example of these SM affirming experiments include discovery of the top quark in 1995 at the Fermi National Accelerator Laboratory (FNAL) Tevatron [24, 25]. A second example is the discovery of the bottom quark in 1977, which took place before the construction of the Tevatron at the Main Ring at Fermilab [26]. The Tevatron is a proton-antiproton collider that was used to confirm Kobayashi's and Maskawa's predictions of a third generation of quarks [27]. Verifying the existence of a fundamental building block of the SM. The third and final example, and perhaps the most notable block to be added, is the Higgs mechanism, which is used to explain the origin of mass in fundamental particles, and was confirmed by the discovery of the Higgs boson using the Large Hadron Collider (LHC) at CERN in 2012 [28, 29].

The science that the LHC enables is a premier example of what has become to be known as Energy Frontier science, or science that relies on accelerating particles to the highest-energies humanly possible and colliding them to produce and study the fundamental constituents of matter [30]. While the Higgs boson was a groundbreaking discovery, it is

one of many that have been and will be made at CERN, there can be no question that Energy Frontier science has encountered a threshold [23]. The effective energy that can be achieved at the LHC is around 14 TeV. The original energy of the LHC was chosen specifically to target the discovery of the Higgs particle using indirect evidence. Now that the Higgs has been discovered, no energy exists such that a discovery or non-discovery can be assured. To increase this threshold either drastic hardware upgrades must be undertaken [31] or different indirect experimental techniques using existing machines must be employed. This is where Intensity Frontier experiments such as Mu2e and COMET, that rely more on the quantity rather than the kinetic energy of accelerated particles, become vital tools in the investigation of the larger experimental picture. The two experiments mentioned here are future muon experiments that will test the SM by indirectly probing a charged lepton flavor-violating (CLFV) process. Experiments like these can probe new physics (NP) mass scales up to $10^4 - 10^5$ TeV/ c^2 [32].

CLFV is a natural extension to the already established Lepton Flavor Violation (LFV) in the SNO [33], Super-Kamiokande [34] and KamLAND [35] experiments. Instead of confirming existing theory, these discoveries have poked holes in our understanding of the SM. Before these experiments, SM neutrinos were considered massless, and therefore SM neutrino mixing was forbidden. These are not the only holes in the SM, in fact the very composition and intrinsic properties of our Universe point to a large hole via the matter-antimatter asymmetry, the existence of dark matter and the accelerating rate of the expansion of the Universe.

While there are many avenues available for studying the SM, the muon perhaps offers one of the best opportunities for discovery. At $2.2 \mu s$ the muon lifetime is much longer than the tau lepton or Z boson, other candidates in which CLFV processes can occur. In addition, intense beams of muons can be produced via the decay of pions which can be created using existing proton sources [2].

Unlike LFV, CLFV has yet to be observed and the rate at which it occurs is model dependent. The rate for LFV processes in neutrinos is constrained by the neutrino mixing parameters. Extensions to the SM predict a wide, order of magnitude range for the rate

of CLFV processes. However, in the SM with neutrino masses and oscillations, this rate is highly suppressed and inaccessible to experimental methods today. An observation of CLFV would be incontrovertible evidence of beyond the standard model (BSM) physics. Furthermore, due to the highly suppressed rate of CLFV, a non-observation would set important rate limits that could rule out other NP extensions to the SM [36].

The normal decay mode for a negative muon, $\mu^- \rightarrow e^- \bar{\nu}_e \nu_\mu$, conserves lepton flavor number. In this process, a decaying negative muon with lepton flavor number, $L_\mu = 1$, results in the creation of a muon neutrino, $L_\mu = 1$, and the creation of an electron, $L_e = 1$, which is accompanied by the creation of an electron antineutrino, $L_e = -1$; conserving both total lepton number and lepton flavor number. The positively charged muon has two potential CLFV decay modes: $\mu^+ \rightarrow e^+ \gamma$ (a direct decay) and $\mu^+ \rightarrow e^+ e^+ e^-$. The CLFV decay mode for the negative muon that Mu2e is interested in specifically is $\mu^- N \rightarrow e^- N$. This process is the neutrinoless-conversion of a stopped muon to an electron in the field of a nucleus. For the branching ratio of the first process mentioned, the MEG experiment at the Paul Scherrer Institute (PSI) has set a limit of 4.2×10^{-13} (at 90% CL) [37] and the SINDRUM collaboration has set the limit of 1×10^{-12} (at 90% CL) for $\mu^+ \rightarrow e^+ e^+ e^-$ [38]. Future experiments MEG-II [39] and Mu3e [40] will probe both $\mu^+ \rightarrow e^+ \gamma$ and $\mu^+ \rightarrow e^+ e^+ e^-$ at an expected level of 6×10^{-14} and $\sim 10^{-15}$, respectively. SINDRUM-II also at PSI has set the best limits to date on the rate of the final process mentioned above, $\mu^- N \rightarrow e^- N$, on three nuclei. The rate is defined as:

$$R_{\mu e} = \frac{\mu^- + A(Z, N) \rightarrow e^- + A(Z, N)}{\mu^- + A(Z, N) \rightarrow \nu_\mu + A(Z, N)} \quad (1.1)$$

$R_{\mu e}(Au) = 7 \times 10^{-13}$ (90% C.L.) [41], $R_{\mu e}(Ti) = 4.3 \times 10^{-12}$ (90% C.L.) [42] and, $R_{\mu e}(Pb) = 4.6 \times 10^{-11}$ (90% C.L.) [43]. Mu2e at FNAL and COMET at JPARC expect to set a limit of 10^{-17} on this same process using an aluminium nucleus.

This dissertation will focus on the Mu2e experiment, the proton source and associated hardware used to create conditions necessary for the measurement of this rate at extremely sensitive levels. To reduce unnecessary backgrounds while maintaining intensity the proton beam must conform to strict requirements including short intense pulses and low inter-pulse particles. These conditions are in part achieved by understanding

the proton source itself and in part by a series of collimators and a set of novel dipole magnets.

Chapter 2

Charged Lepton Flavor Violation

The Super Kamiokande experiment in 1998 was the first to conclusively established that the disappearance of ν_μ was consistent with the process $\nu_\mu \rightarrow \nu_\tau$ [34]. These results were combined with that from solar, beam and reactor neutrino experiments, providing clear evidence for oscillations in flight between neutrinos and antineutrinos of different flavors.

Prior to this discovery, lepton flavor numbers were assumed to be conserved. Mixing between the lepton families has since shown that LFV is a very real process whose rate is governed by neutrino mixing parameters. However, this still does not mandate the existence of CLFV. The rate of CLFV is model dependent and therefore has discovery potential over a wide range of physics models that extend the standard model.

2.1 Theory Overview

CLFV can occur in lepton processes such as tau decays, meson decays and the decay of the Z boson. However, muon decays are favored for experimental applications because they are the most sensitive to CLFV processes. However, the rate of CLFV is largely dependent on the model chosen to extend the SM. In the minimal extension to the standard model, which this section will discuss in greater detail, the amplitude for $\mu \rightarrow e\gamma$, shown in Figure 2.4, is proportional $(\Delta m_{ij}^2/M_W^2)^2$ where Δm_{ij}^2 is the mass-squared difference between the *i*th and *j*th neutrino mass eigenstates and M_W is the mass of the W-boson. This results in a conversion rate on the order of 10^{-50} , because the neutrino mass differences are so small relative to M_W . This rate is well beyond experimental limits today. While

this is a virtually zero rate, other extensions to the standard model produce amplitudes comparable to the quoted conversion rate [2].

To understand these rare muon processes, a firm understanding of the flavor structure of the SM and LFV phenomenology is needed. The standard model Lagrangian defines three fundamental interactions: the strong, electromagnetic and weak forces, which are in turn described by gauge theory of quarks and leptons. As was alluded to earlier, there are three generations of quarks and leptons: three quarks of $\frac{2}{3}e$ electric charge including the aforementioned top quark, and three of $\frac{1}{3}e$ charge. Correspondingly, there are three charged leptons of $e-$ electric charge including the muon, and three species of neutrinos of neutral charge: electron neutrino (ν_e), muon neutrino (ν_μ) and tau neutrino (ν_τ). The SM Lagrangian that governs the interactions between these particles can be summarized as follows,

$$L = L_{\text{gauge}} + L_{\text{Higgs}} + L_{\text{Yukawa}} \quad (2.1)$$

It is important to understand the Yukawa interaction because this describes the flavor couplings. These couplings arise through the fermion mass generation from the spontaneous symmetry breaking of the $SU(2)_L \times U(1)_Y$ symmetry. These are generally represented by square matrices with complex values whose eigenvalues are lepton and quark masses. The differences of these eigenstates to those of weak interactions define favor mixing [44]. The Yukawa interaction can be written as follows,

$$L_{\text{Yukawa}} = (y_e)_{ij} H^+ \bar{e}_{iR} l_{jL} + (y_d)_{ij} H^+ \bar{d}_{iR} q_{jL} + (y_u)_{ij} \tilde{H}^+ \bar{u}_{iR} q_{jL} + H.c. \quad (2.2)$$

where $(y_e)_{ij}$, $(y_d)_{ij}$ and $(y_u)_{ij}$, are Yukawa coupling constants for charged leptons (e.g. e), the down-type quarks (d), and the up-type quarks (u), respectively. Subscripts L and R represent left and right handed chirality. q_{jL} and l_{jL} represent doublet fields where the j subscript refers to the generation. These fields are written as follows,

$$q_{jL} = \begin{pmatrix} u_{jL} \\ d_{jL} \end{pmatrix}, \quad l_{jL} = \begin{pmatrix} \nu_{jL} \\ e_{jL} \end{pmatrix} \quad (2.3)$$

and finally H is the higgs doublet field represented as follows,

$$H = \begin{pmatrix} \phi^+ \\ \phi^0 \end{pmatrix} \quad (2.4)$$

and \tilde{H} ,

$$\tilde{H} = \begin{pmatrix} \phi^{0*} \\ -\phi^- \end{pmatrix}. \quad (2.5)$$

We can also write the Higgs potential or the potential energy of the Higgs field as,

$$V(\phi) = \mu^2 \phi^+ \phi + \lambda (\phi^+ \phi)^2 \quad (2.6)$$

This potential is a scalar field that is symmetric under rotations in ϕ space. The minimum of this potential, or the vacuum expectation value, is not at $\phi = 0$ - in fact it is $v = \frac{|\mu|}{\sqrt{\lambda}}$. The fluctuation around this value is what breaks the rotational symmetry of the potential. By choosing the value of μ we can choose the direction of the fluctuation so that the Higgs vacuum field becomes,

$$\phi^0 = \begin{pmatrix} 0 \\ \frac{v}{2} \end{pmatrix} \quad (2.7)$$

Substituting the Higgs field back into the potential, the mass term for quarks and leptons can be seen to emerge,

$$L_{mass} = -\left(\bar{e}_{iR}(m_e)_{ij}e_{jL} + \bar{d}_{iR}(m_d)_{ij} + \bar{u}_{iR}(m_u)_{ij}u_{jL}\right) + H.c. \quad (2.8)$$

where $(m_e)_{ij} = -(y_e)_{ij}(v/\sqrt{2})$, $(m_d)_{ij} = -(y_d)_{ij}(v/\sqrt{2})$ and $(m_u)_{ij} = -(y_u)_{ij}(v/\sqrt{2})$. Now noting that each mass matrix is diagonalized by unitary transformation on the lepton doublet (l_{iL}) and singlet fields (e_{jR}), the charged weak current interaction for leptons can be written in this basis as,

$$L_{W\bar{\nu}e} = -\frac{g}{\sqrt{2}}\left(\bar{\nu}_{iL}\gamma^\mu e_{iL}W_\mu^+ + \bar{e}_{iL}\gamma^\mu \nu_{iL}W_\mu^-\right). \quad (2.9)$$

The lepton flavors, L_e , L_μ , L_τ , are shown to be conserved [36].

To introduce CLFV into the picture of the SM presented here, LFV must first be understood, because LFV SM extensions allow for CLFV through oscillations in loops that

can produce the extremely suppressed rates introduced earlier. As described, these rates are often dependent on the neutrino masses themselves, so the mass generating mechanism must be carefully considered. Extending the SM using non-zero neutrino masses and neutrino flavor mixing is necessary. The observed neutrino mixing in solar and atmospheric experiments such as SNO and IceCube, as well as other types of neutrino experiments like reactor and accelerator experiments (see KamLAND and MINOS as examples) have brought to light many vital parameters such as the mass-squared differences in neutrinos, but scientists have yet to pin down an exact mass for each neutrino. Their absolute values do, however, have upper limits that were set using a variety of experimental techniques [45]: $< 0.8 \text{ eV}/c^2$ for the electron neutrino mass, measured by studying the shape of the beta decay spectrum [46], and $< 170 \text{ eV}/c^2$ for the muon neutrino mass measured at PSI using muons from the decay of pions produced by a proton beam [47], and finally, $< 18.2 \text{ MeV}/c^2$ the tau neutrino mass was constrained using LEP, an electron-positron collider at CERN [48].

Flavor violation in neutrinos can be described by the the Pontecorvo-Maki-Nakagawa-Sakata (PMNS) matrix. This matrix diagonalizes the neutrino mass matrix connecting the flavor and mass eigenstates of the neutrino as follows,

$$\nu_\alpha = \sum_i U_{\alpha i} \nu_i \quad (2.10)$$

where ν_α is a neutrino eigenstate and ν_i is a neutrino mass eigenstate and U is the unitary mixing matrix, the PMNS matrix. The Dirac phase δ and the mixing angles θ_{ij} which parameterize this matrix can be used to calculate the probability of neutrino oscillation over a distance,

$$P(\nu_\alpha \rightarrow \nu_\beta) = \left(\sum_{ij} U_{\alpha i} U_{\beta j}^* e^{i\Delta m_{ij}^2 L/(2E)} \right)^2 \quad (2.11)$$

Where L is the distance traveled, Δm_{ij}^2 is the mass-square difference of the neutrinos and E is the energy [49].

To see how this matrix appears in the description of the SM so far, we must go back to the Lagrangian. Perhaps the simplest way to generate neutrino masses in the SM is

by adding the following Dirac extension to equation 2.2,

$$L_{\nu R} = (y_\nu)_{ij} \tilde{H}^+ \nu_{iR} l_{jL} + H.c. \quad (2.12)$$

$(y_\nu)_{ij}$ is the Yukawa coupling for neutrinos, which if very small, $O(10^{11})$, produces neutrino masses within the experimental limits. This addition does however allow for lepton flavor violation but lepton number conservation.

Another popular mass-generating mechanism for neutrinos is the “see-saw mechanism” [36]. To write this down, adding the Majorana mass term is necessary. The Majorana mechanism allows for mass generation of left-handed fermions, without needing to add a right-handed counterpart. This requires the neutrino to be its own anti-particle. The new mass term with the Majorana mechanism is written as follows,

$$L_{\nu mass} = -\frac{1}{2} \left(\overline{(\nu_{iL})^c}, \bar{\nu}_{iR} \right) \begin{pmatrix} 0 & m_D^T \\ m_D & M_R \end{pmatrix} \begin{pmatrix} \nu_{jL} \\ (\nu_{jR})^c \end{pmatrix} + H.c. \quad (2.13)$$

where the Dirac mass term is m_D . M_R is the Majorana neutrino matrix. When the Majorana mass scale is much larger than the Dirac masses, simplifications can be made and the lighter neutrino masses are given by,

$$m_\nu = m_D^T (M_R)^{-1} m_D. \quad (2.14)$$

If M_R is 10^{15} GeV and the Dirac masses are near 100 GeV the neutrino mass becomes $O(10^{-2})$ eV, hence the name “see-saw” [36]. While both of the scenarios described here are plausible, careful experimentation will reveal weather the Dirac or Majorana or perhaps both approaches to the mass-generating mechanism describe reality.

Another popular theory is supersymmetry (SUSY) specifically supersymmetric grand unification theories (SUSY GUT). The reason for their popularity is not only because they predict larger rates for the rare muon processes discussed here, but their predictions of the gauge couplings are consistent with measurement. LFV is introduced into the SM through the mass matrices of the of supersymmetric partner of the leptons and quarks, the sleptons and squarks. In particular, CLFV can be seen in the slepton mass matrix at the GUT scale (10^{16} GeV) or on the mass scale of the Majorana neutrino via the “see-saw mechanism” as we have already seen.

In the minimal supersymmetric Standard Model (MSSM), off diagonal elements in the slepton mass matrix after it has been written in a basis where it can be diagonalized is where LFV is introduced. The upper limit for $\mu^+ \rightarrow e^+\gamma$ places a limit on an off diagonal term in this matrix,

$$\frac{\Delta m_{\mu\bar{e}}^2}{m_{\tilde{l}}^2} \lesssim 10^{-3} \left(\frac{m_{\tilde{l}}}{100\text{GeV}} \right)^2 \quad (2.15)$$

where $m_{\mu\bar{e}}$ is the off diagonal matrix element, and $m_{\tilde{l}}$ is the mass of a slepton [36]. MSSM is unfavorable though, because it suggests that only a very limited number of symmetry breaking scenarios will produce the required parameters that satisfy the constraints already imposed by the MSSM [50]. Many SUSY GUT models remedy this issue and provide avenues for the largest CLFV branching ratios through radiative corrections to the slepton mass matrices [36].

While CLFV rates are model specific, a general Lagrangian can be parameterized and is useful in understanding the scope of the effect rare muon searches will have on the theoretical landscape [51],

$$L_{CLFV} = \frac{m_\mu}{(1+\kappa)\Lambda^2} \bar{\mu}_R \sigma_{\mu\nu} e_L F^{\mu\nu} + \frac{\kappa}{(1+\kappa)\Lambda^2} \bar{\mu}_L \gamma_\mu e_L (\Sigma \bar{q}_L \gamma^\mu q_L) \quad (2.16)$$

Where Λ is the effective mass scale and κ is a dimensionless parameter that controls the relative contribution of the two terms. $F_{\mu\nu}$ is the photon field strength and m_μ is the muon mass. The first term, or the dipole term, mediates process such as $\mu \rightarrow e\gamma$, $\mu \rightarrow eee$ and $\mu N \rightarrow eN$. This term arises from charged loops that exchange real or virtual photons. Figure 2.3 shows the two diagrams that describe the terms in equation 2.16. The first term is described by Figure 2.3(a). This term includes $\mu \rightarrow e\gamma$ and always occurs at the loop level. Figure 2.2(a) shows the process probed in the MEG experiment. The second term, pictured in Figure 2.3(b), is the four-fermion operator, which mediates at the leading order, muon into electron conversion and $\mu \rightarrow eee$ and $\mu N \rightarrow eN$. This operator occurs at tree level and involves the exchange of a massive neutral boson. Figure 2.2(b) shows the process probed in the SINDRUM II experiment. While the conversion rate can constrain the dipole operator, the $\mu \rightarrow e\gamma$ rate does not constrain the four-fermion operator. Figure 2.1 shows the the mass scale in TeV, Λ , as a function of κ . The left

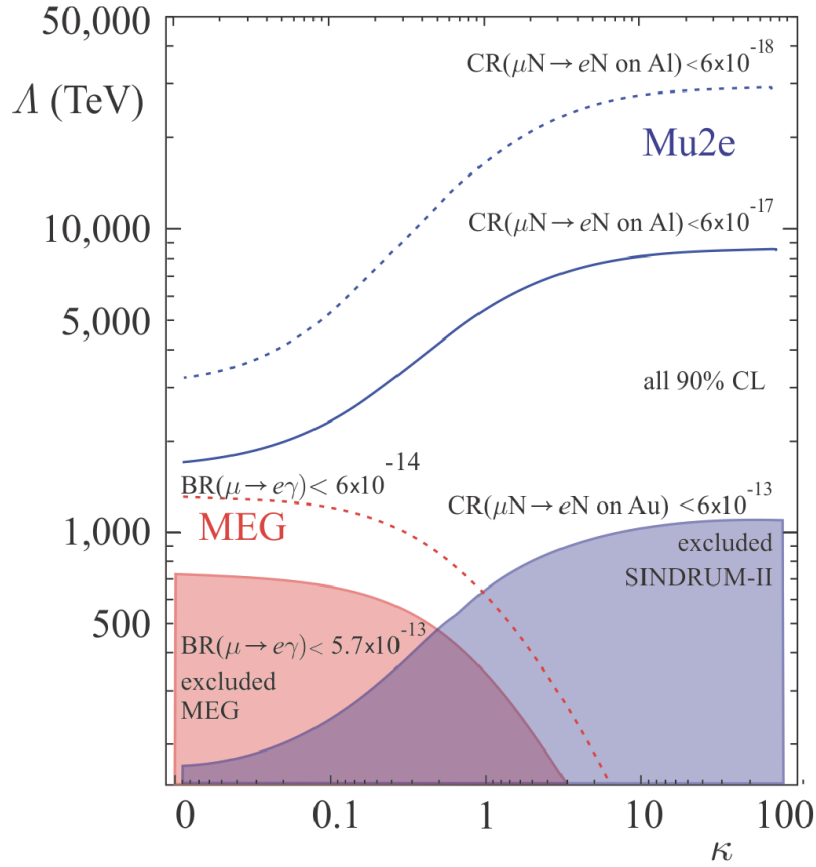
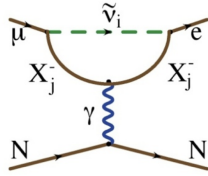


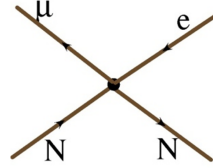
Figure 2.1: Λ as a function of κ for a muon to electron conversion experiment with a sensitivity in the range of $10^{-16} - 10^{-17}$ is compared to that for a $\mu \rightarrow e\gamma$ experiment with a sensitivity in the range of $10^{-13} - 10^{-14}$. The current and projected exclusion regions of parameter space for $\mu \rightarrow e\gamma$ are indicated by red contours, those for $\mu \rightarrow e$ conversion by blue contours.

side of Figure 2.1 corresponds to decays or conversion events that include photons and the right side corresponds to those involving heavy bosons.

Figure 2.1 implies that if a $\mu \rightarrow e\gamma$ signal is observed a conversion signal should also be observed. While if a $\mu \rightarrow e\gamma$ signal is not observed, there is still potential to find a $\mu \rightarrow e$ conversion signal. It is also important to note that while Λ is an effective mass scale, it is on the order of 10^4 Tev in Figure 2.1, which as mentioned is beyond what we can currently probe directly with colliders [2].

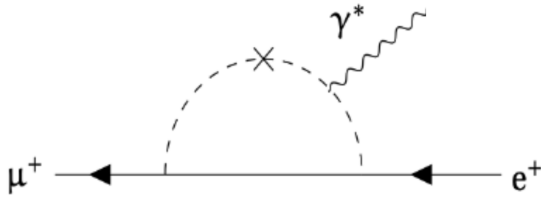


(a) Feynman diagram of $\mu^+ \rightarrow e^+\gamma$ as probed by the MEG experiment.

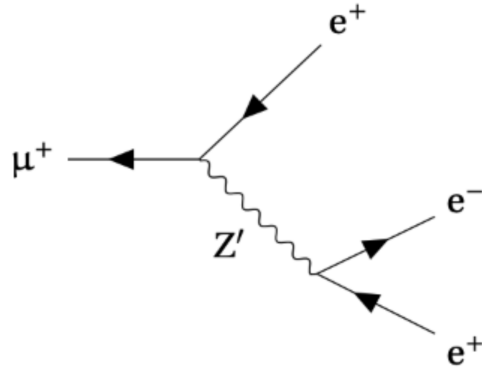


(b) Feynman diagram of $\mu^+ \rightarrow e^+e^-e^+$ as probed by the SINDRUM II experiment.

Figure 2.2: Feynman diagrams describing the SINDRUM II and MEG experiments parameter space, highlighted in blue and red in Figure 2.1. These shaded regions are the extremes of the parameter space.



(a) General Feynman diagram of $\mu^+ \rightarrow e^+\gamma$. This diagram will always have a loop in it.



(b) General Feynman diagram of $\mu^+ \rightarrow e^+e^-e^+$.

Figure 2.3: General Feynman diagrams describing higher order loop and tree level diagrams.

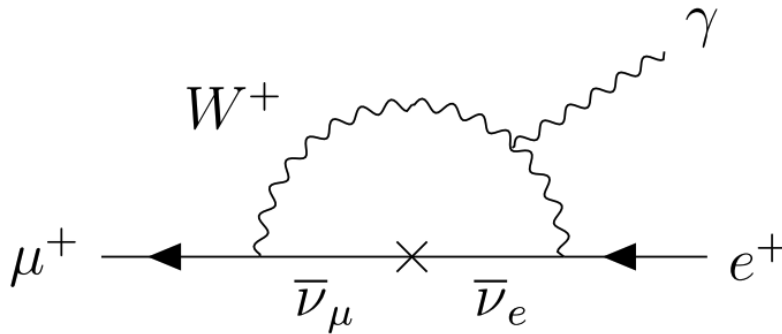


Figure 2.4: Feynman diagram of $\mu^+ \rightarrow e^+\gamma$ via neutrino mixing.

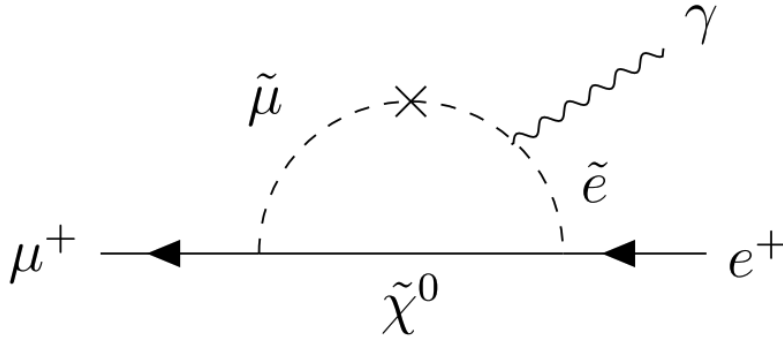
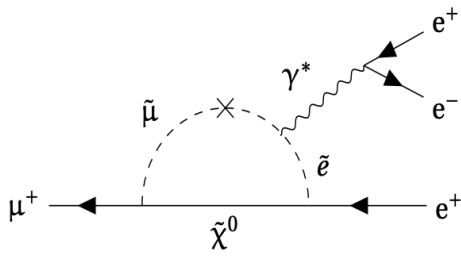


Figure 2.5: Feynman diagram of $\mu^+ \rightarrow e^+\gamma$ via SUSY.

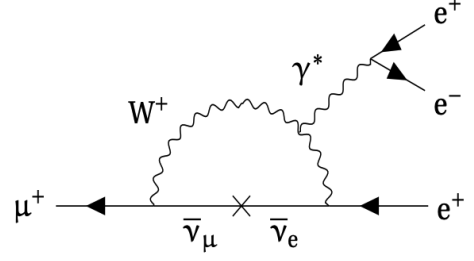
2.1.1 $\mu^+ \rightarrow e^+\gamma$

As mentioned previously, the MEG experiment has set a limit for the rate of the $\mu^+ \rightarrow e^+\gamma$ to the rate of regular muon decay $\mu^+ \rightarrow e^+\nu\bar{\nu}$ of 4.2×10^{-13} (at 90% CL) [37]. The first term in equation 2.16 parameterizes this interaction and arises through loops with an emitted photon that in this case is real, as shown in Figures 2.5 and 2.4. The process described by the latter diagram is entirely possible in the current standard model with massive neutrinos, whereas Figure 2.5 involves previously the mentioned SUSY theoretical framework.

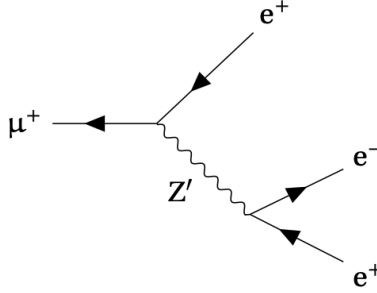
MEG used a continuous surface muon beam at an intensity of $> 10^8 \mu/s$ that was produced via the decay of pions created using the high-intensity proton accelerator facility (HIPA) and a stopping target at PSI. The signal is a two body decay of the muon at rest where the energy of the photon and momentum of the positron and their relative angle and timing are the measured quantities. The most prominent backgrounds come from radiative muon decays (RMD), $\mu^+ \rightarrow e^+\nu\bar{\nu}\gamma$ or from a regular muon decay that coincides with a photon from RMD, annihilation of two positrons or bremsstrahlung. Unfortunately, a higher sensitivity is not linearly dependent on higher statistics, because the background created by the intense muon beam eventually overwhelms the signal. MEG-II will use the same beamline with major upgrades to the rate capability of all detectors involved, to push the intensity frontier to its limits once again [52]. MEG-II will increase this sensitivity to about 6×10^{-14} .



(a) Feynman diagram of $\mu^+ \rightarrow e^+e^+e^-$ via SUSY.



(b) Feynman diagram of $\mu^+ \rightarrow e^+e^+e^-$ via neutrino mixing.



(c) Feynman diagram of $\mu^+ \rightarrow e^+e^+e^-$ at tree level via Z' .

Figure 2.6: Feynman diagrams for the $\mu^+ \rightarrow e^+e^+e^-$ decay in different theoretical models[1].

2.1.2 $\mu^+ \rightarrow e^+e^+e^-$

Figure 2.6 shows the $\mu^+ \rightarrow e^+e^+e^-$ process in three channels in extensions to the SM. This process is highly suppressed at branching ratios of $O(10^{-54})$ for the process shown in figure 2.6a. The first term in equation 2.16 mediates the interaction shown in figure 2.6a and the second term mediates the process in figure 2.6c. With $\kappa \gtrsim 10$, SINDRUM best constrains this tree level interaction [40].

The SINDRUM experiment has set the limit of 1×10^{-12} (at 90% CL) [38] for the $\mu^+ \rightarrow e^+e^+e^-$ process branching ratio. SINDRUM used a continuous muon beam at $\sim 5 \times 10^6 \mu/s$ produced at PSI. The main reducible backgrounds include that from accidental coincidences between low invariant mass electron-positron pairs mainly from Bhabha scattering and photon conversion, and uncorrelated regular decay positrons. This can be limited by placing relative timing and momentum constraints on the constituents. The irreducible background comes from the $\mu^+ \rightarrow e^+e^+e^-\bar{\nu}_\mu\nu_e$ interaction, which ultimately

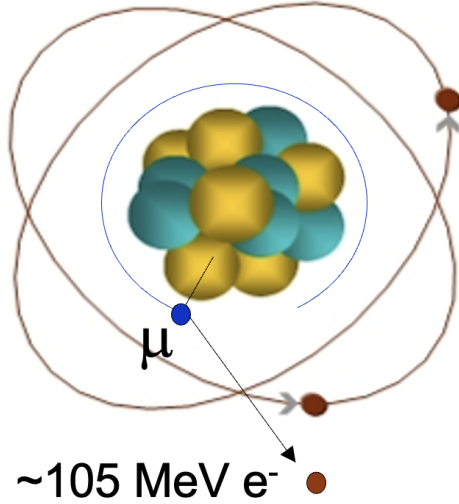


Figure 2.7: Diagram of the recoiling nucleus, captured muon and the mono-energetic electron produced in the Mu2e experiment. The energy of the electron can be calculated exactly and results in a very clean experimental signature.

limits the sensitivity by the detector momentum resolution. MEG-II [39] and Mu3e [40] at PSI will probe both $\mu^+ \rightarrow e^+\gamma$ and $\mu^+ \rightarrow e^+e^+e^-$ at an expected level of 6×10^{-14} and $\sim 10^{-15}$, respectively. These experiments expect to see a muon beam at an intensity of $> 10^8 \mu/s$.

2.1.3 $\mu^- N \rightarrow e^- N$

Similar to $\mu^+ \rightarrow e^+e^+e^-$, the conversion process is described by both terms in equation 2.16, relevant across all values of κ , and will be sensitive to new physics regardless of the relative contribution of the two terms. This is the primary motivation for the experiment. This process also includes the exchange of a virtual photon or a virtual neutral boson, and if a signal is observed the presence or absence of a signal in the $\mu \rightarrow e\gamma$ process will be the biggest clue as to its nature. While searches for $\mu^+ \rightarrow e^+e^+e^-$ and $\mu^+ \rightarrow e^+\gamma$ have so far employed similar experimental techniques, $\mu^- N \rightarrow e^- N$ searches rely on the clear signature of monochromatic electrons and for this reason uses a pulsed muon beam to reduce backgrounds primarily from radiative pion capture (RPC). The pulsed structure also allows Mu2e and COMET experiments to take advantage of a factor of $\sim 10,000$ increase in total muon intensity over previous experiments. Other backgrounds include that from regular decay of muons captured by the target nucleus, or decay in orbit (DIO)

muons. In the Mu2e experiment the muon is captured by an aluminium nucleus and converts to an electron in the field of the nucleus as pictured in Figure 2.7. The final energy of the electron is slightly lower than the muon rest mass,

$$E_e = E_\mu - B - E_{recoil} \quad (2.17)$$

where B is the binding energy and E_{recoil} is the recoil energy of the nucleus. The final energy of the electron is monochromatic because the nucleus recoils coherently. The mass of the target plays a part in reducing the background from radiative muon capture. This process can produce a photon that could potentially pair produce, resulting in an electron that would mimic the Mu2e conversion signal. If the difference between the mass of the daughter nucleus and the parent nucleus is greater than 2 MeV, the resulting photon will be below the energy threshold for pair production to occur. The binding energy depends on the number of protons in the target nucleus as well. The final energy of the electron is 104.973 MeV well above the endpoint of the Michel spectrum at 52.8 MeV, which describes the electron spectrum from a freely decaying muon. However, when the freely decaying muon gets captured by the nucleus the resulting electron can exchange a photon with the nucleus which brings the tail of this spectrum up to the conversion energy of the electron of interest ultimately limiting the achievable single-event-sensitivity [5].

2.2 Limitations of Previous Experiments and Driving Consideration for Mu2e

To motivate the following chapter it is important to point out the limitations faced by previous experiments and the solutions Mu2e uses to overcome these obstacles. Mu2e's increase in sensitivity is enabled by two experimental techniques: the use of a graded field solenoid system to transport and select muons, and the use of a pulsed proton beam.

Using a concept first proposed some 25 years ago [53], Mu2e will place the primary production target in a graded solenoidal magnetic field. This will serve to increase the muon production efficiency. Muons are then sent to spiral down the Transport Solenoid field which will further select low energy muons. The muons will finally encounter the aluminium target, which is placed in a uniform solenoid field precisely selected to optimize

the muons capture on the target. This allows Mu2e to surpass the current most intense muon production facility, PSI, by almost three orders of magnitude while simultaneously reducing the proton beam intensity [54].

A large limiting factor of past experiments, such as SINDRUM-II as previously stated, was background events from pions. The SINDRUM-II experiment used the PSI muon beam, which was effectively a continuous stream of intense muons. This did not allow for the separation of the prompt background from the measurement and was the ultimately the limitation of the SINDRUM-II experimental method, which could not go to higher beam intensity without being overwhelmed by the pion background [54]. The Mu2e experiment will use a pulsed beam and will be introduced in more detail in the next section.

Chapter 3

Mu2e Experiment

Upcoming experiments that probe the same parameter space as Mu2e are: the MEG experiment, cited in Section 2.1.1 for the branching ratio of $\mu^+ \rightarrow e^+\gamma$, which is currently being upgraded to an expected sensitivity of 6×10^{-14} [52], COMET [55] an experiment at JPARC, which aims to measure the same ratio as Mu2e, $R_{\mu e}(Al)$, at a similar sensitivity. The sensitivity as a function of year for each experiment is shown in Figure 3.1.

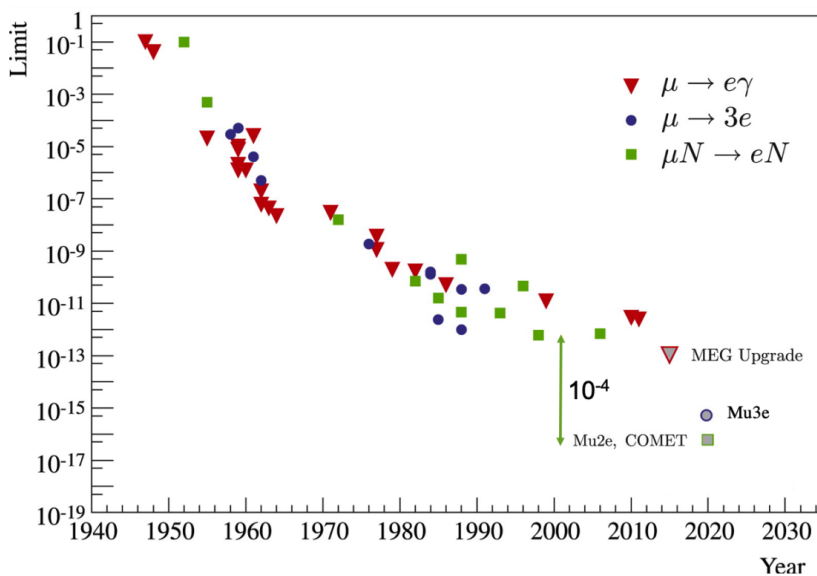


Figure 3.1: Sensitivity as a function of year, each data point represents an experiment, past or projected [2].

Achieving an increase in sensitivity of four orders of magnitude requires a thorough understanding of all the expected backgrounds in Mu2e. The next section will detail each

background in general terms.

3.1 Backgrounds

As with any experiment, the main challenge confronting Mu2e is mitigating the background processes that may overwhelm the signal. The design of the experiment is based largely around this concept and therefore motivates the following sections. The energy of the final signal electron is given by Equation 2.17 and for a coherently-recoiling aluminum nucleus has been calculated to be 104.973 MeV [3]. Some of these mono-energetic events will however be smeared downward into the various background regions from energy loss in target and detector material via dE/dx . The backgrounds for the Mu2e experiment scale with the number of observed muons and therefore the number of protons. To achieve a single-event-sensitivity of 10^{-17} , Mu2e must observe 10^{17} muons at a resolution limited by several backgrounds discussed here.

3.1.1 Decay In Orbit

The most obvious background is that from muons freely decaying and those decaying in the orbit of the stopping target Al nucleus, or DOI electrons. Freely decaying muons can produce electrons as high as 53 MeV which is well below the energy region of the signal electron. However, the electrons produced in the orbit of a nucleus receive a boost in energy from the exchange of a virtual photon. The resultant DOI spectrum is shown in Figure 3.2. The tail of this spectrum overlaps with the signal space and therefore defines the resolution of the detectors shown in Figure 3.3.

The muons decaying in orbit also have a lifetime of 864 ns, compared to 2.2 μ s for freely decaying muons. This DOI spectrum drives both the acceptance requirement for the detector and the resolution requirement for the tracker. The time between proton pulses is 1.7 μ s. If the level of protons inside this window is kept low, meaning there are very few out-of-time protons, this allows for the majority of the backgrounds to decay away before any of the detectors start taking data. The data taking period is called the live or selection window. This window starts around 700 ns after a given pulse, at this point the majority of the DOI muons have decayed away. Figure 3.4 shows the relative timing

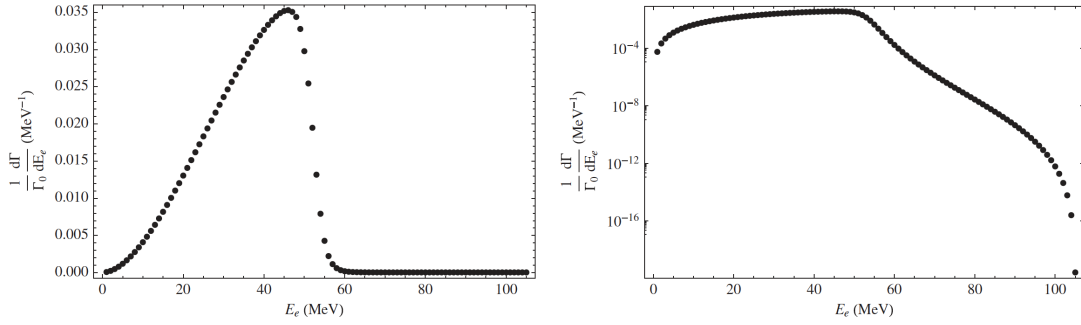


Figure 3.2: Decay-in-orbit electron spectrum in aluminum near the endpoint, normalized to the free-muon decay rate Γ_o . The left-hand plot is on a linear scale, the right a logarithmic one [3].

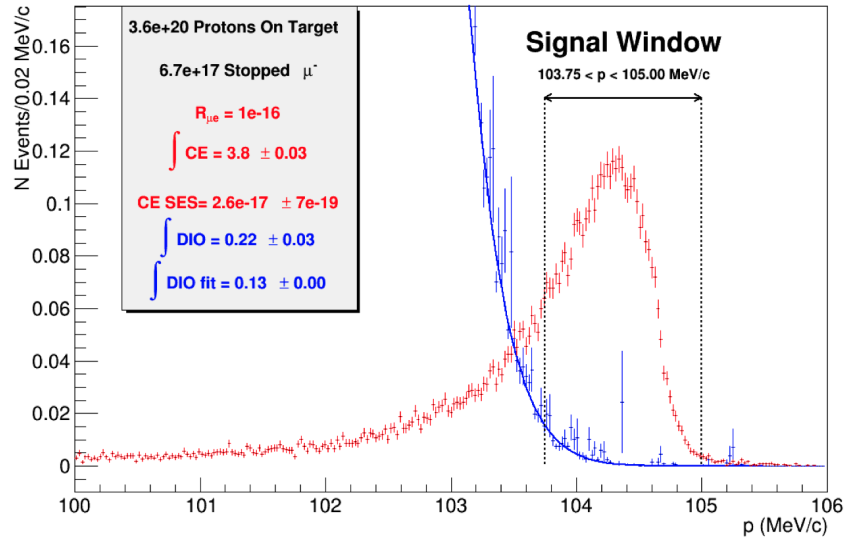


Figure 3.3: Histogram of the tail of the DOI spectrum overlaid with the expected conversion signal for the given statistics as a function of particle momentum [4].

structure of the proton pulse distribution with the background distributions described here.

3.1.2 Radiative Pion Capture

RPC is the process $\pi^- N \rightarrow \gamma N'$, where N' is an excited nuclear state. This occurs when pions reach a stopping target nucleus and produce a virtual or on-shell photon which through internal conversion or pair-production can lead to an electron being produced near the conversion energy. The energy of the photon depends on the final state of the nucleus which is unique and can assume many states, smearing the resulting photon

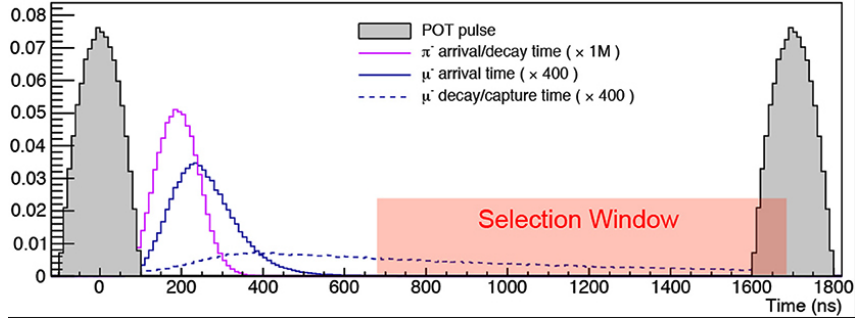


Figure 3.4: The Mu2e beam timing. Shown here are the time distributions for the following processes: pions and muons arriving at the detector solenoid and the decay or capture time of said muons. The “Selection window” is the period of time for which Mu2e will analyze data, the live gate will take data as early as about 500 ns, with the final accepted region determined through analysis [5].

energy. Pions however have a short lifetime of 26 ns compared to muons captured on aluminium, this prompt background can therefore be eliminated almost entirely by the pulsed beam structure.

3.1.3 Decay in Flight

Pions and muons can also decay-in-flight, $\pi^- \rightarrow \bar{\nu}_e e^-$, which can produce a 105 MeV electron if the initial momentum of the pion is near 58 MeV. Again, proton beam cleanliness is the key to reducing this background. With the current beam structure, a muon or pion with sufficient energy to produce an electron in the signal region would arrive before 500 ns relative to the previous proton pulse, this is 200 ns before the live window shown in Figure 3.4 [5].

3.1.4 Antiproton

Antiprotons are an important and unfortunately constant background for Mu2e as they do not decay and can travel very slowly. Antiprotons are produced at and before the production target as the protons travel down the beam pipe and are often much lower in momentum than the other particles. The issue arises when antiprotons annihilate on nuclei and produce a significant number of secondary particles at the stopping target. Their production threshold is near 4.1 GeV and not well understood for backward production. Ultimately, antiprotons can annihilate on nuclei and produce a significant number of

secondary particles at the stopping target. The antiprotons themselves are mitigated using a number of thin absorber windows along the transport solenoid.

3.1.5 Cosmic Ray

Finally, the background from cosmic rays can either produce muons that can decay in the solenoid system and mimic the conversion signal or they can interact with the stopping target or any other part of the solenoid system and produce an electron at the conversion energy. These electrons are indistinguishable from the signal electron and are mitigated using the CRV, which will be described in Section 3.2.6.

3.2 Solenoids and Detectors

Increasing the sensitivity of the previous experiment by four orders of magnitude places very challenging requirements on the proton beam used to create the muons, because many major backgrounds for the experiment are prompt with respect to the production protons. In fact, the SINUNDRUM II experiment was largely limited by the prompt backgrounds discussed here. These backgrounds include electrons from RPC and those from muons/pions decaying in flight (μ/π - DIF). It is therefore critical that there be no protons outside of the nominal pulse width at the 10^{-10} fractional level. This requirement is known as “Extinction” [56].

The experiment will use an 8 GeV proton beam consisting of short (~ 250 ns) pulses of protons, separated by $1.7 \mu\text{s}$, as illustrated in Figure 5.9. The muons will be created via the decay of pions created by 8 GeV protons impinging on a tungsten target. The out-of-time protons will be eliminated using the extinction system located on the M4 beamline just before the tungsten production target. The resulting muons will then be transported through a series of solenoids: the Production Solenoid (PS) takes the brunt of the proton beam and therefore requires the most shielding in addition to the strength to redirect the resulting pions nearly 180 degrees, the Transport Solenoid (TS), s-shaped and where the majority of the pions will decay away, and the Detector Solenoid (DS), a graded magnetic field solenoid that redirects beam-related backgrounds to produce the cleanest signal possible. The muons will be captured on an aluminium nucleus in the stopping target

housed in the Detector Solenoid and the resulting position and momentum of the electrons will be measured using a straw tube tracker oriented transverse to the solenoid axis. The crystal calorimeter is located downstream of the tracker, oriented similarly and will allow for particle discrimination as well as a check on the tracker measurement. Finally, the Cosmic Ray Veto (CRV) detector, made of plastic scintillators, will surround the entire DS and TS and will provide coincidence measurements for backgrounds associated with high energy charged particles that come from the atmosphere [2]. An illustration of the solenoid system is shown in Figure 3.6

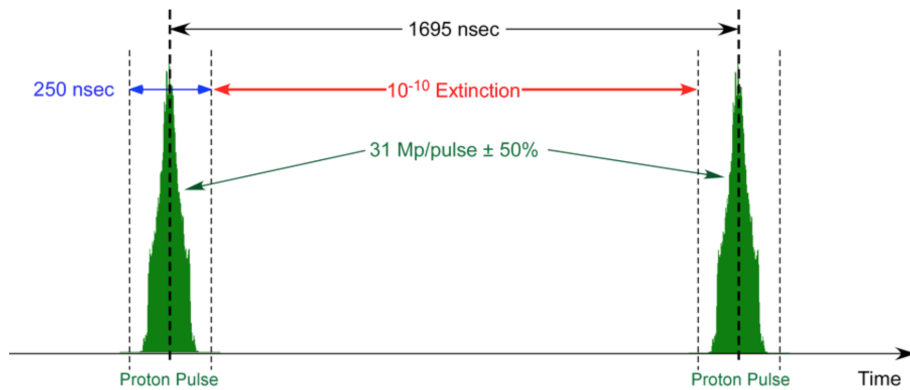


Figure 3.5: Pulse structure required by the Mu2e Experiment. The requirement that there be no protons outside of the nominal pulse width above the 10^{-10} fractional level is referred to as “Extinction” [6].

The Mu2e final state of the muon beam is formed while passing through the solenoid system shown in Figure 3.6. The solenoids are used to transport muons from the production target to the stopping target all while minimizing the transmission of other particles and maximizing the muon beam intensity. The solenoid fields range from uniform to complex gradients that reach up to 4.6 Tesla, and are specifically designed for situations encountered in each step of the muon production and transport process.

A basic summary of the three general requirements in order to achieve reasonable background levels given the sensitivity requirement are:

- The muon beam transport must be optimized to accept low energy, negative muons.
- The tracking detector must be blind to muons that decay-in-flight.

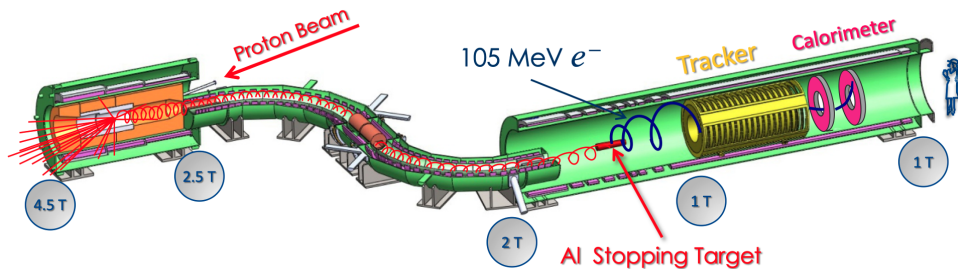


Figure 3.6: Cartoon of the solenoid layout and magnetic field strengths in Tesla for the Mu2e experiment. The Production Solenoid reverses direction of pions and some muons and cuts out electrons, neutrons and photons that would otherwise overwhelm the Mu2e detectors. The Transport Solenoid allows pions time to decay, reducing the RPC background. High momentum muons run into the walls of the TS and the positive muons are reduced using a collimator system. The Detector Solenoid carefully deflects conversion electrons into the tracker while allowing harmful backgrounds to pass through to a beam dump [2].

- The detectors must be able to resolve the decay-in-orbit signal, meaning a low mass tracker and thin, segmented target is necessary.

3.2.1 Production Solenoid and Target

The production solenoid (PS) contains the production target which is a radiatively cooled tungsten rod. The protons enter the solenoid at a 17° angle to its axis and the pions exit the in the backwards direction guided by a gradient magnetic field as they decay into muons. A schematic view of the M4 beamline, the PS and other components can be seen in Figure 3.7. The magnetic field reaches a peak of 4.6 Tesla at the target and drops off at about 0.28 T m^{-1} . Backward production of the muon beam filters the beam down to low energy muons as well as reflected forward muons with a high probability of being captured by the aluminium target. A nice side effect of this production method is that the upstream detectors do not get overwhelmed with the leftover flux from the proton beams interaction with the target. While negative pions are not the only product in this interaction, backward pions and pions that are reflected via pinch confinement are slow enough to be captured in the aluminum target. Neutrons, photons, electrons and positrons are among some of the other leftover particles that are directed into the beam dump past the production solenoid. In addition to these leftovers, a portion of the proton beam is scattered and directed though a port in the production solenoid that leads to a detector

called the extinction monitor. The extinction monitor will see a 4 GeV proton beam and use this to statistically measure the fractional out-of-time beam (extinction level), that will verify that the extinction system in the M4 beamline is working as expected [5, 57].

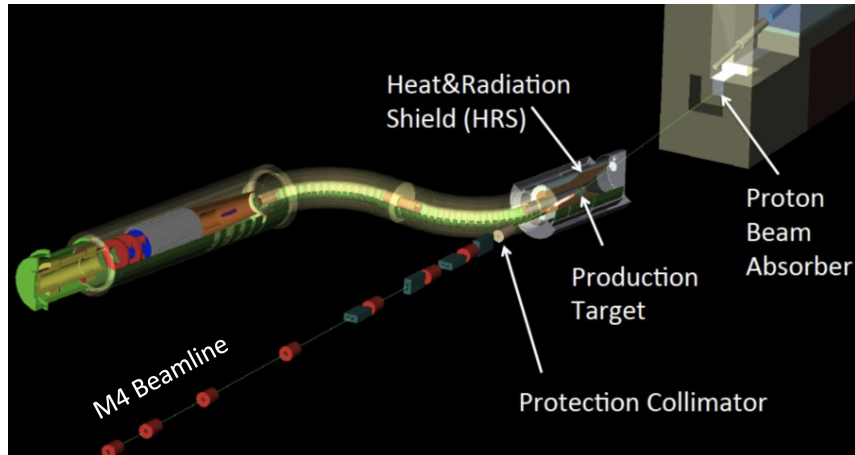


Figure 3.7: The Mu2e target area and components in relation to the M4 beamline and the TS [2].

One of the most challenging features in the PS is the design of the heat and radiation shield (HRS), which surrounds the production target. It's location is pictured in Figure 3.7. The HRS in conjunction with a liquid helium cooling system protects the superconducting solenoid from quenching due to the extreme heat from the target and intense flux from the proton beam. The beam at the PS has 8 kW of power and a flux of 3.9×10^7 . The tungsten target is radiatively cooled meaning it releases heat through thermal radiation and into the HRS [5, 2].

3.2.2 Transport Solenoid

The “S” shaped Transport Solenoid (TS) shown in Figure 3.8 is mainly used to clean and shape the muon beam. The shape does not allow for photons and positive muons to be transmitted. The positive muons are separated out, because the vertical displacement of the muons as they wind their way to the DS depends on the charge of the particles. As horizontal displacement of the muons increases so does the vertical separation. This can be seen if we look at the equation for the velocity of the muons in the vertical direction,

v_{vert} ,

$$v_{vert} = \frac{\rho v_0}{2B^2} (B \times \nabla B) \quad (3.1)$$

Where $\rho = \frac{p}{qB}$ and B is the solenoid field which is perpendicular to the drift velocity. The drift of the muons as they wind their way down the TS is clearly dependent on the charge, q [7]. The positive muons are stopped by a collimator halfway through the TS. The collimator effectively selects low energy negative muons. See Figure 3.9 for a diagram of the muon paths and the location of the collimator.

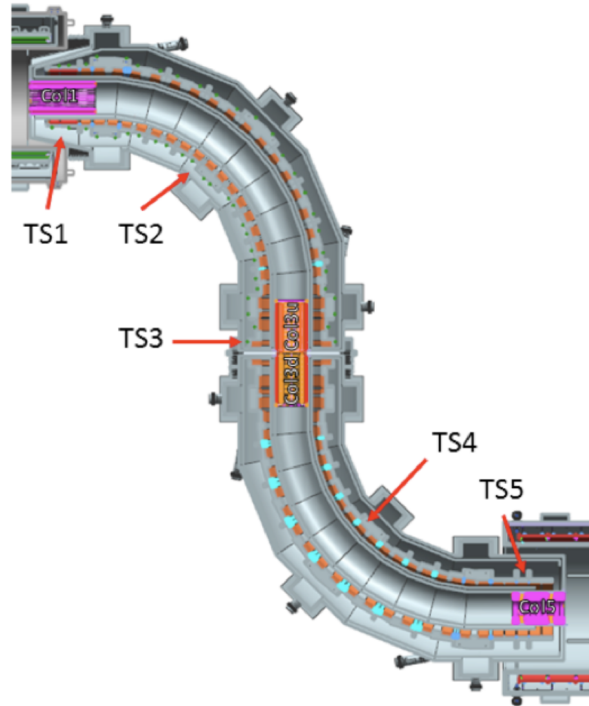


Figure 3.8: The Mu2e Transport Solenoid [7].

The field of the TS is also set such that high momentum particles with momentum greater than 90 MeV run into the sides of the solenoid. The radius of gyration is given by,

$$r = \frac{P_{\perp}}{0.3B} \quad (3.2)$$

Where P_{\perp} is the component of momentum perpendicular to the solenoid axis and B is the magnetic field. The length of the solenoid is also important as it allows pions time to decay away before reaching the DS, further suppressing the background from RPC [5].

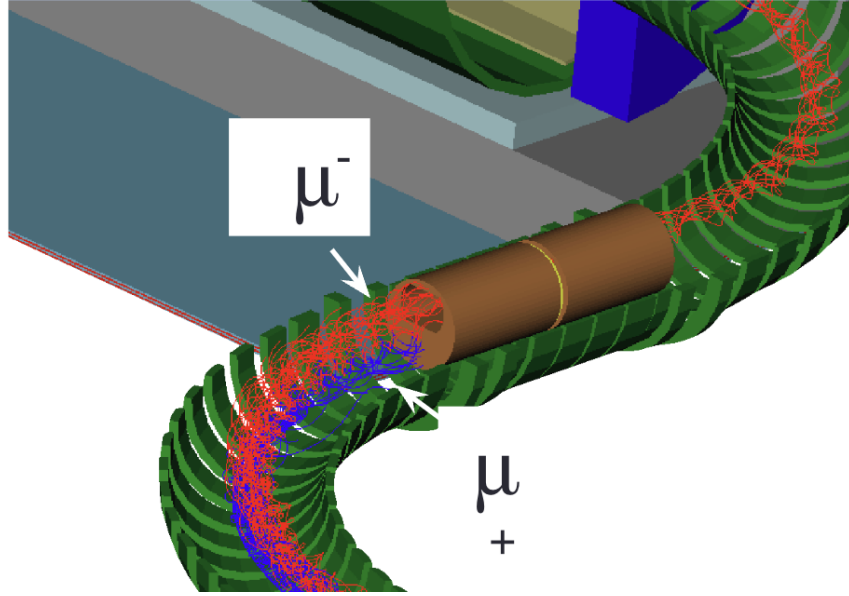


Figure 3.9: A zoomed in section of the Transport Solenoid with a selection collimator. μ^- paths are shown in red and μ^+ are shown in blue [7].

3.2.3 Detector Solenoid and Target

The Detector Solenoid contains the aluminum stopping target, calorimeter and tracker. The orientation of the detector system and the DS is shown in Figure 3.6. The annular arrangement is necessary to select the momentum of the detected muons, effectively removing low-momentum and DOI electrons. In addition, the annular design allows particles produced by the beam flash, and the remnants of the muon beam that may cause additional backgrounds, to pass untouched through the middle of the system into a beam dump. The gradient of the DS goes from 2.5 T at the TS juncture to about 1 T at the detector region, such that the electrons are pitched forward into the detectors acceptance region.

The stopping target consists of thin aluminum foils stacked longitudinally with a hole in the center whose radius allows low momenta muons ($< 53 \text{ Mc}^{-1}$) to pass through to the beam dump. A mock up of the design is shown in Figure 3.10. The reason for thin stacked foils is to reduce energy loss through dE/dx of the resulting electrons. This energy loss can push the electrons down into the DOI spectrum tail. The number and thickness of the foils was carefully selected to reduce energy loss as these electrons travel to the tracker.

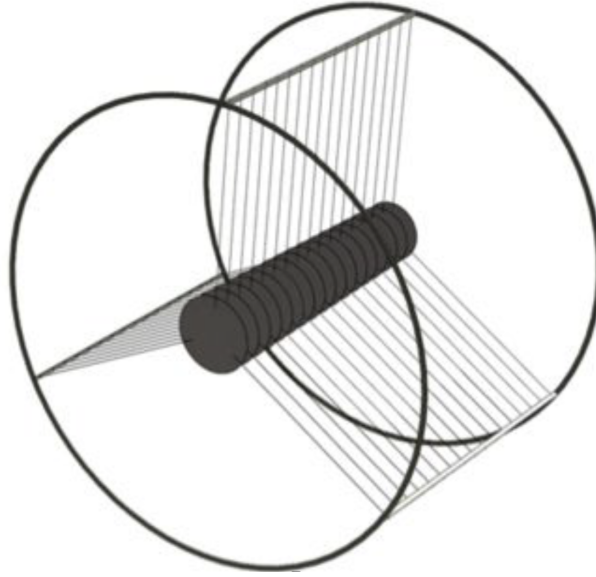


Figure 3.10: Rough illustration of the stopping target. 37 100 μm thick aluminum foils with a hole in the center large enough to allow electrons with momentum $< 53 \text{ MeV}/c$ to pass through untouched [2].

3.2.4 Tracker and Calorimeter

The tracker is a straw tube tracker shown in Figure 3.11, chosen for its low mass and excellent resolution. The hole in the middle of the tracker is designed to allow electrons from Michel decay to pass through untouched. As mentioned previously the detector resolutions is a major limiting factor to the single-event sensitivity because the DOI spectrum tail overlaps with the narrow expected conversion signal. The low mass of the tubes allows the majority of the electrons produced to be detected using as little material as possible, as these electrons have already been smeared downward in energy by the interaction with material in the stopping target. The tubes or straws are aluminum and gold coated Mylar sheets surrounding a gold plated tungsten sense wire. The electrons enter the tube, which acts as a cathode held at 1,500 Volts, and ionize the 80% argon and 20% CO_2 gas held inside the straw. The resulting ions drift to the tungsten wire where they are counted and their timing is measured to reconstruct the longitudinal position of the electron track. Given this information and a precise measurement of the magnetic field of the DS, Mu2e can reconstruct the electron momentum.

The calorimeter consists of two flat rings composed of CsI crystals and is located

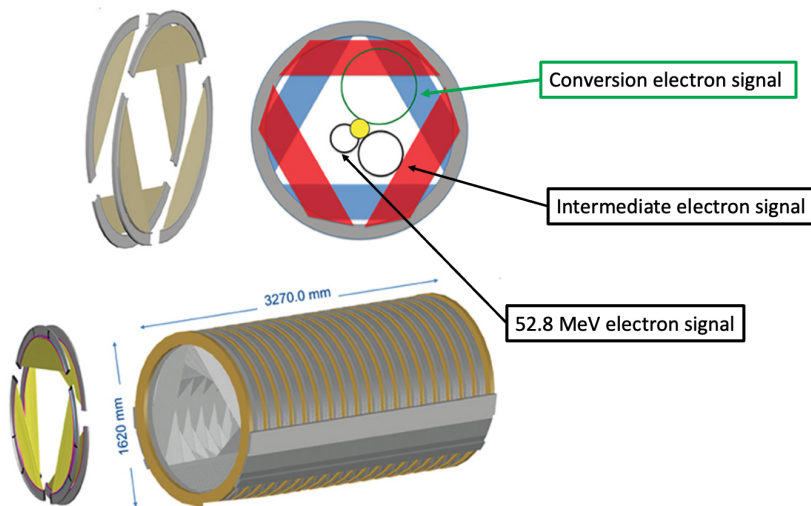


Figure 3.11: Schematic of the tracker. The red and blue portions are the straw tubes and the circles represent the area in which Mu2e expects to see a signal for given electron energies [8].

downstream from the tracker with the same annular geometry. The signals from electrons and muons interacting with the crystals are read out by silicon photomultiplier tubes (SiPMs). The calorimeter measures the energy of each particle and acts as a check to the tracker measurement. It also provides information that allows for separation of electron and muon signals with similar energy in post-analysis [5].

3.2.5 Stopping Target Monitor

In addition to the conversion signal, Mu2e will need to measure the denominator of the ratio $R_{\mu e}$ which, given the geometry of the DS, can be measured by monitoring the x-ray signal emitted when a captured muon enters the $s1$ state. Muon-to-electron conversion can occur incoherently and from higher states, but these are both small effects. In addition, the coherent conversion signal has been shown to be amplified by the Z of the nucleus as Z^5 [58].

The X-ray detected will be that from the $2p \rightarrow 1s$ transition as well as $3p \rightarrow 1s$ and $4p \rightarrow 1s$. A high purity germanium detector is the usual choice to detect these transitions. However, these detectors are too slow to count each and every X-ray at Mu2e's required intensity. In addition, high energy photons pair producing and resulting in electrons at harmful energies to the detector make it impossible to place even a heavily shielded

detector closer than 35 m from the stopping target. A statistical measurement approach may also be considered by waiting for a long pause in the beam timing structure and measuring the gamma rays from the $^{27}\text{Al} \rightarrow ^{27}\text{Mg}$ decay [5].

3.2.6 Cosmic Ray Veto

As discussed previously in Section 3.1.5, cosmic rays can produce signal-like events in many ways that are indistinguishable from conversion signals. These events can originate in any part of the Mu2e solenoid system so the CRV must ideally cover the majority. However, the resultant neutron flux from the proton beam limits the coverage because neutrons cause significant deadtime and radiation damage in the detector. Figure 3.12 shows the neutron rates over the body of the CRV. The CRV will use extruded scintillator with embedded wavelength-shifting fibers as counters because they are well studied and simple to operate [5]. The CRV must operate with an excellent efficiency, about 0.9999, in an intense radiation environment [59].

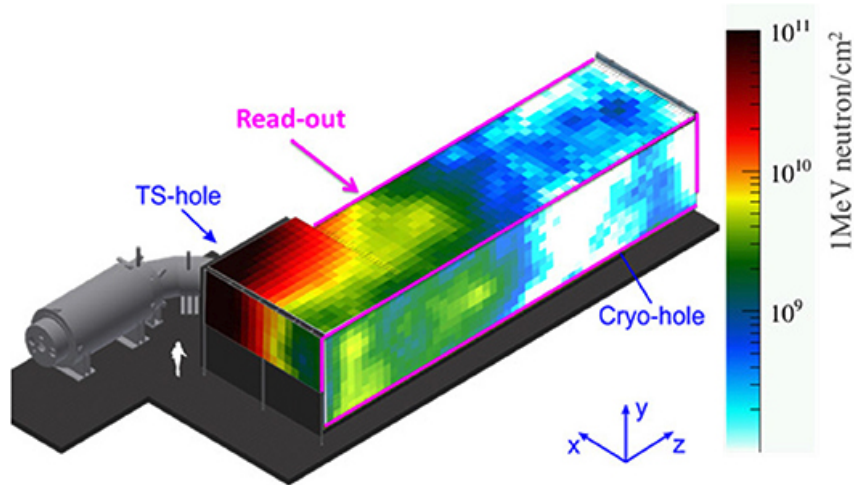


Figure 3.12: The Mu2e CRV system with neutron rates as seen by the counters [2].

Chapter 4

Quick Primer in Accelerator Physics

The following chapters will include terms and concepts commonly used in accelerator physics to describe the longitudinal and transverse motion of particles in phase space. These concepts are not commonly taught in physics courses and so will be defined here for reference.

4.1 Transverse Motion

The following chapters are largely motivated by the beams transverse shape and size making the equations of motion in the transverse direction indispensable to this discussion.

The coordinate system that will be used for the following derivation is pictured in Figure 4.1. The vertical coordinate, describing the displacement of a particle with respect to the ideal orbit is indicated by y , the corresponding horizontal coordinate is x , and the coordinate that is pointing into the direction of the longitudinal motion and that is moving with the particles around the ring is called s [9].

The condition for a circular orbit can be expressed mathematically by the equality between the Lorentz force and the centrifugal force. While magnetic fields are not the only way to focus particles along their journey, electric fields at low energies and field gaps in RF cavities can also provide a focusing force, at high energies they offer the only solution. So, neglecting any electrostatic field we get,

$$evB = \frac{\gamma m v^2}{\rho} \quad (4.1)$$

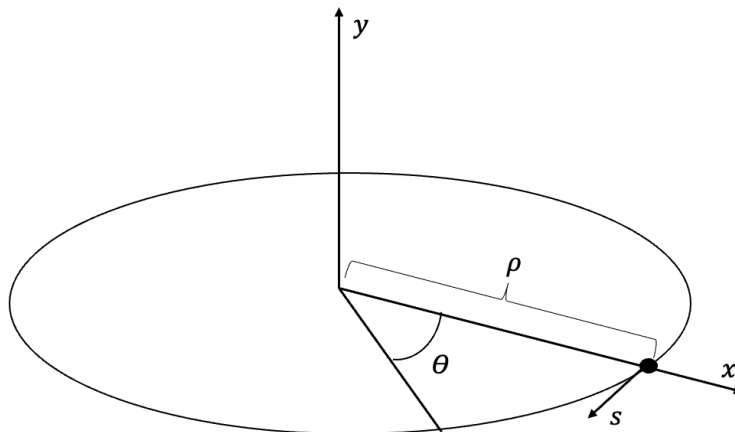


Figure 4.1: Coordinate system for a particle following the ideal path around a circular accelerator assuming a homogeneous dipole field [9].

where we assume a homogeneous field, B , and a charged particle with momentum $p = mv$ and charge e . The beam rigidity can be expressed as,

$$B\rho = \frac{p}{e} \quad (4.2)$$

This quantity can be conceptualized as the possible momentum of a particle given a field strength in a circular accelerator for bounded motion. While the homogeneous dipole field will keep an ideal particle in place as it travels around the orbit in Figure 4.1, this is not true for the rest of the particles in the bunch. These particles will be displaced slightly by $\rho + x$, and given only bending magnets, will fall into its own stable orbit or worse be lost all together, destroying the final bunch intensity. To keep these particles from straying too far from the ideal orbit, focusing magnets must be used. There are two types of focusing: weak and strong. Strong focusing will be referenced for the rest of this section as it is the most common type of focusing used in accelerators today. In addition, we will be assuming linear restoring forces in the transverse directions. This means the transverse and longitudinal motion can be treated separately, and the two degrees of freedom in the transverse direction remain uncoupled [10].

4.1.1 Thin Lens Quadrupole

The strong focusing magnets are often a series of gradient quadrupoles that act as a series of focusing and defocusing lenses. It is useful to think about the focusing magnets as

lenses so we may construct a methodology that describes the restoring forces a particle feels as it travels through a focusing section using well studied and simple optical concepts. Using Maxwell's equation $\nabla \times B = j + \frac{dE}{dt}$ and a few assumptions it is possible to derive the following relationship for the restoring forces,

$$\frac{\partial B_y}{\partial x} = \frac{\partial B_x}{\partial y} \quad (4.3)$$

These assumptions are that there are no changing electric fields and no magnetic current density, j , through the center of the quadrupole allowing us to set the cross product to zero [9].

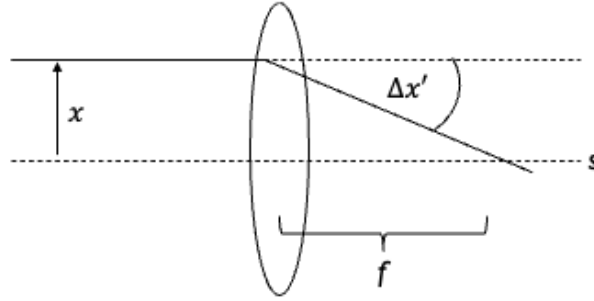


Figure 4.2: Convex lens with focal length f , bending a light ray initially parallel to the optical axis [10].

Note that the quadrupole is focusing in one direction and defocusing in the other making it necessary to have a series of quadrupoles as the total focusing element. Assuming a thin lens, making $B_y = \frac{\partial B_y}{\partial x} x = B' x$ constant, we can approximate a quadrupoles focal length,

$$\frac{1}{f} = -\frac{\Delta x'}{x} \quad (4.4)$$

Where Figure 4.2 depicts these variables, and the change in x as a function of the longitudinal coordinate, s , is $x' = dx/ds$ or the slope of the particles trajectory. $\Delta x'$ may be written as,

$$\Delta x' = -\frac{l}{\rho} = -l \frac{eB_y}{p} = -\left(\frac{eB'l}{p}\right)x \quad (4.5)$$

Where we have used Equation 4.1 to replace the curvature of the trajectory through the lens, ρ . The focal length becomes,

$$\frac{1}{f} = \frac{eB'l}{p} = \frac{B'l}{B\rho} \quad (4.6)$$

Where we have used Equation 4.2 to simplify. It is useful to describe multiple focusing elements using a series of matrices, and as discussed earlier, multiple elements are necessary to produce a net focusing effect across both transverse planes. Rewriting the change in the particles x coordinate in matrix form after passing through a convex lens,

$$\begin{pmatrix} x \\ x' \end{pmatrix}_{out} = \begin{pmatrix} 1 & 0 \\ -\frac{1}{f} & 1 \end{pmatrix} \begin{pmatrix} x \\ x' \end{pmatrix}_{in} \quad (4.7)$$

The difference between concave and convex lens is the sign of the focal length. There will also be space between each lens which can be described as a drift length, L , and written in matrix form as,

$$\begin{pmatrix} x \\ x' \end{pmatrix}_{out} = \begin{pmatrix} 1 & L \\ 0 & 1 \end{pmatrix} \begin{pmatrix} x \\ x' \end{pmatrix}_{in} \quad (4.8)$$

Where a duo of concave and convex lens' with a drift in between can be described as,

$$\begin{pmatrix} 1 & 0 \\ -\frac{1}{f} & 1 \end{pmatrix} \begin{pmatrix} 1 & L \\ 0 & 1 \end{pmatrix} \begin{pmatrix} 1 & 0 \\ \frac{1}{f} & 1 \end{pmatrix} = \begin{pmatrix} 1 + \frac{L}{f} & L \\ -\frac{L}{f^2} & 1 - \frac{L}{f} \end{pmatrix} \quad (4.9)$$

Assuming L is much smaller than f this arrangement would produce a net focusing effect, demonstrating that it is possible to focus in two degrees of freedom at once. It is crucial to an accelerators design to understand the effect of many elements such as the one presented here, placed around the accelerator ring for a given L and f . The series of these elements that make up the full ring is called the lattice [10].

4.1.2 Equation of Motion

Now that we have introduced the concept of a lattice and how this can be described in matrix form, we will provide a more concrete derivation of the particles' motion through the lattice. Although we used the thin lens approximation in the previous section, it should be noted that this solution is generally applicable to any field described by a constant plus a gradient. Starting from the particles position in our coordinate system in Figure 4.1 the position of a particle can be expressed as $R = (\rho + x)\hat{x} + y\hat{y}$. Where ρ describes the radial coordinate and direction, and $\rho + x$ is the radial displacement. R is a vector comprised of components in the \hat{x} and \hat{y} directions. The acceleration, d^2R/dt^2 ,

must be balanced by the Lorentz force $\vec{F} = e\vec{v} \times \vec{B}$ felt by the particle in the non-ideal orbit. First, we must write down the velocity,

$$\frac{dR}{dt} = \dot{r}\hat{x} + r\frac{d\hat{x}}{dt} + \dot{y}\hat{y} \quad (4.10)$$

where $r = \rho + x$ and \hat{x} is the unit vector in the radial direction. If the particle is moving in the \hat{s} direction, the unit vector in the radial direction should have a derivative that can be related to the angular coordinate in Figure 4.1. The change in the angular coordinate $\Delta\theta$ is equal to the difference in longitudinal position, s , divided by the curvature of the given path, ρ . Given this geometrical argument, we can write the time derivative of the unit vector in the radial direction as $(d\hat{x}/dt) = \dot{\theta}\hat{s}$. Substituting this, we can write,

$$\frac{dR}{dt} = \dot{r}\hat{x} + r\dot{\theta}\hat{s} + \dot{y}\hat{y} \quad (4.11)$$

Now to get the acceleration take the time derivative again, minding the unit vectors and the chain rule,

$$\frac{d^2R}{dt^2} = \ddot{r}\hat{x} - r\dot{\theta}^2\hat{x} + 2\dot{r}\dot{\theta}\hat{s} + r\ddot{\theta}\hat{s} + \ddot{y}\hat{y} \quad (4.12)$$

Noting that the Lorentz force in the \hat{x} and \hat{y} directions (assuming no magnetic field in the \hat{s} direction) is the derivative of the particle momentum,

$$\frac{dp}{dt} = m\gamma\frac{dv}{dt} = ev \times B \quad (4.13)$$

Where γ is the Lorentz definition and m is the mass of the particle. Setting the part of Equation 4.12 in the \hat{x} direction equal to Equation 4.13 we obtain,

$$(\ddot{r} - r\dot{\theta}^2) = -\frac{ev_s B_y}{m\gamma} \quad (4.14)$$

Similarly, for the y direction,

$$\ddot{y} = \frac{ev_s B_y}{m\gamma} \quad (4.15)$$

To switch coordinates for convenience we write d/dt as $(ds/dt)(d/ds)$. Taylor expanding the magnetic field $B_y = B_0 + x\frac{\partial B_y}{\partial x}$, making use of Equation 4.3 and replacing r with $\rho + x$ we can finally write down the transverse equations of motion [10],

$$\frac{d^2x}{ds^2} + \left[\frac{1}{\rho^2} + \frac{1}{B\rho} \frac{\partial B_y}{\partial x} \right] x = 0 \quad (4.16)$$

$$\frac{d^2y}{ds^2} - \frac{1}{B\rho} \frac{\partial B_y}{\partial x} y = 0 \quad (4.17)$$

Where we have used the fact that the velocity in the \hat{x} and \hat{y} directions are much smaller than that in the \hat{s} direction, to write the total momentum as $\gamma m v_s$, which from Equation 4.2 can be written in terms of the beam rigidity, $(B\rho)$.

4.1.3 Closed Form Solution

Assuming the coupling between the two transverse planes can be ignored, these equations can be viewed as analogs of the simple harmonic oscillator and therefore have similar solutions. In this analogy the spring constant k is $\left[\frac{1}{\rho^2} + \frac{1}{B\rho} \frac{\partial B_y}{\partial x} \right]$ which describes the focusing strength of the quadrupole and the weak focusing of the dipole. However, this analogy can only be taken so far, it is important to remember that particles in an accelerator operate in a unique multi-periodic system. Minimally, one system is needed to describe the oscillation around a particles ideal orbit and one must describe the changes to its motion on a turn-by-turn basis as a function of s . In fact, the focusing strength of the quadrupoles can be written as a periodic function of s such that $k(s+L) = k(s)$ where L is one turn around the accelerator. Equations 4.16 and 4.17 are examples of Hill's equation, which describes this turn by turn motion, and the solutions can then be written as,

$$x = Aw(s) \cos(\psi(s) + \delta) \quad (4.18)$$

where A and δ are constants of integration that reflect the initial conditions and $w(s)$ is a periodic function with period L . Noting similarities between this solution and the harmonic oscillator solution, we can write $\psi = \sqrt{K}s$. To determine $w(s)$ and $\psi(s)$, substitute Equation 4.18 into Equation 4.16,

$$x'' + Kx = A(2w'\psi' + w\psi'') \sin(\psi + \delta) + A(w'' - w\psi'^2 + Kw) \cos(\psi + \delta) = 0 \quad (4.19)$$

Requiring that the coefficients of the sine and cosine vanish, and multiplying the sine term by w we can write,

$$2ww'\psi' + w^2\psi'' = (w^2\psi')' = 0 \quad (4.20)$$

Rewriting ψ' in terms of an arbitrary constant of integration, ϕ , we have,

$$\psi' = \frac{\phi}{w(s)^2} \quad (4.21)$$

And we can extract a differential equation for $w(s)$,

$$w^3(w'' + Kw) = \phi^2 \quad (4.22)$$

Since we are describing a particles motion through a periodic accelerator system we can restrict the solution to only those that have $w(s)$ that are periodic in L . In addition, we can re-write the solution from in Equation 4.18 as a product of matrices that represent basic components of an accelerator as in Section 4.1.1,

$$x = w(s)(A_1 \cos \psi + A_2 \sin \psi) \quad (4.23)$$

And,

$$x' = (A_1 w' + \frac{A_2 \phi}{w}) \cos \psi + (A_2 w' - \frac{A_1 \phi}{w}) \sin \psi \quad (4.24)$$

The initial conditions can be defined as: x_0 and x'_0 at s_0 , where the initial conditions in y and w become, $y(0) = 0$ and $w = w(s_0)$. Using these definitions we can write,

$$A_1 = \frac{x_0}{w} \quad (4.25)$$

$$A_2 = \frac{x'_0 w - x_0 w'}{\phi} \quad (4.26)$$

So the full matrix describing the particle motion in the periodic system becomes,

$$\begin{pmatrix} x(s_0 + L) \\ x'(s_0 + L) \end{pmatrix} = \begin{pmatrix} \cos \Delta\psi_L - \frac{ww'}{\phi} \sin \Delta\psi_L & \frac{w^2}{\phi} \sin \Delta\psi_L \\ -\frac{1+(ww'/\phi)^2}{(w^2/\phi)} \sin \Delta\psi_L & \cos \Delta\psi_L + \frac{ww'}{\phi} \sin \Delta\psi_L \end{pmatrix} \begin{pmatrix} x(s_0) \\ x'(s_0) \end{pmatrix} \quad (4.27)$$

where $\Delta\psi_L = \int_{s_0}^{s_0+L} \frac{\phi ds}{w^2(s)}$. It should be noted that Equation 4.27 only holds if L is the circumference of the accelerator. Defining conventional and more physically meaningful variables using the Courant-Snyder Parameters we can write out the beta function, β , and it's counterparts α and γ (not to be confused with the Lorentz definitions),

$$\beta(s) = \frac{w^2(s)}{\phi} \quad (4.28)$$

$$\alpha(s) = -\frac{1}{2} \frac{d\beta(s)}{ds} \quad (4.29)$$

$$\gamma = \frac{1 + \alpha^2}{\beta} \quad (4.30)$$

Writing our original solution with these parameters and absorbing ϕ into the constant ϵ ,

$$x(s) = \sqrt{\beta\epsilon} \cos(\psi(s) + \delta) \quad (4.31)$$

Here β describes the motion of the transverse oscillation and therefore the size of the beam, and ϵ is the emittance of the beam. Noting that $\beta(s) = \beta(s + L)$ and rewriting $\Delta\psi_L$ we can further evaluate the physical significance of the beta function,

$$\Delta\psi_L = \int_{s_0}^{s_0+L} \frac{ds}{\beta(s)} \quad (4.32)$$

$\Delta\psi_L$ is the phase advance of the oscillation. The smaller the amplitude of the beta function the larger the phase advance. Rewriting Equation 4.27 in terms of the Courant-Snyder parameters,

$$\begin{pmatrix} x(s_0 + L) \\ x'(s_0 + L) \end{pmatrix} = \begin{pmatrix} \cos \Delta\psi_L + \alpha \sin \Delta\psi_L & \beta \sin \Delta\psi_L \\ -\gamma \sin \Delta\psi_L & \cos \Delta\psi_L - \alpha \sin \Delta\psi_L \end{pmatrix} \begin{pmatrix} x(s_0) \\ x'(s_0) \end{pmatrix} \quad (4.33)$$

Equation 4.33 can now be simplified even further in the following notation,

$$M = I \cos \Delta\psi_L + J \sin \Delta\psi_L = e^{J\Delta\psi_L} \quad (4.34)$$

Where I is the identity matrix and J is,

$$\begin{pmatrix} \alpha & \beta \\ -\gamma & -\alpha \end{pmatrix} \quad (4.35)$$

With the help of Equation 4.9 which described the particles motion through two quadrupoles and a drift, M describes the elements through which the particle traverses as it makes it's way around the entire accelerator.

To evaluate the significance of ϵ we take the derivative of the transverse solution,

$$x'(s) = -\frac{\sqrt{\epsilon}}{\sqrt{\beta(s)}} [\alpha(s) \cos(\psi(s) + \delta) + \sin(\psi(s) + \delta)] \quad (4.36)$$

Noting the following relation,

$$\alpha(s)x(s) + \beta(s)x'(s) = -\sqrt{\epsilon\beta(s)} \sin(\psi(s) + \delta) \quad (4.37)$$

We can eliminate the trigonometric functions in the transverse solution and its derivative by squaring and summing Equations 4.31 and the equation above. Rearranging, the emittance for a single particle as a function of x and x' becomes,

$$\epsilon = \gamma x^2 + 2\alpha x x' + \beta x'^2 \quad (4.38)$$

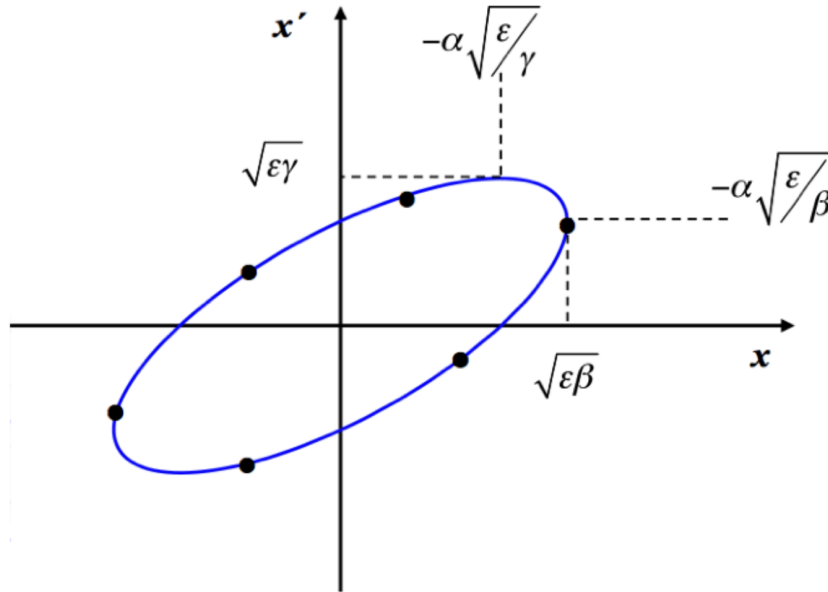


Figure 4.3: An ellipse in transverse phase space of the coordinate x . Courant-Snyder parameters can be used to parametrize the ellipse.

This defines an ellipse in transverse phase space that a particle will travel on a turn-by-turn basis, called the betatron oscillation. Figure 4.3 shows the phase space trajectory of a particle. According to Liouville's theorem, ϵ is a constant of motion, analogous to the total energy of a harmonic oscillator. For each point in the lattice there exists an ellipse that changes shape moment to moment, but the value of ϵ remains the same, preserving the area.

So far we have considered only particles with the same total momentum. As the beam accelerates, however, the emittance will decrease. This phenomenon is known as adiabatic

damping. Generally, Liouville's theorem states that for a coordinate variable q and its conjugate momentum p , the integral of pdq over the region in p - q phase space containing all particles will be a constant of the motion. That is $\int pdq = \text{constant}$. In an accelerator, in x - x' phase space $p_x = x'p = x'(\beta\gamma mc)$. The expression of Liouville's theorem becomes $\int p_x dx = \int x'(\beta\gamma mc) dx = \pi\epsilon\beta\gamma mc = \text{constant}$. Thus, the constant of the motion is the invariant emittance, which is $\beta\gamma\epsilon$. Note that all of the β above take the relativistic definition (i.e. v/c). We can see that the the change in the emittance is proportional to the fractional change in the momentum.

To understand the collective properties of the beam that we will be using in the following discussion, it is useful to derive parameters that define the maximum size of the beam. In x the maximum size is given by $\sqrt{\epsilon\beta}$ and in x' the max size is $\sqrt{\epsilon\gamma}$. ϵ depends on the area over which the particles are distributed, different particle distributions will give different 95% emittances. For Mu2e we assume a Gaussian beam distribution in the horizontal plane with 95% of the beam contained within this ellipse [9].

4.2 Longitudinal Motion

In addition to transverse motion, we must also consider longitudinal motion and will, in the following sections, describe the equations of motion as well as the important concepts surrounding this discussion. Concepts such as impedance and space charge will feature in the later chapters when we discuss beam line simulations.

4.2.1 Impedance

Impedance describes the interaction of the charged particles circulating in the accelerator with the surrounding conducting beam line elements. These effects are referred to here as impedance or collective effects. The effects manifests as a decelerating voltage as the beam passes through or by conducting elements.

As a charged particle passes through a perfectly shaped and perfectly conducting tube an image charge is created on the conductors surface. In a perfect conductor this charge is equal and opposite. As the particle moves beyond this conducting tube the image charge disappears. However, in a real beam line the conducting elements namely the accelerating

structures are not perfectly shaped conductors nor are they perfectly conducting. These imperfections can cause secondary fields that linger after the initial particle has passed by the conducting element. Given that a common beam structure is bunches of charged particles slightly separated in time and space, the bunch arriving after one has already passed will see the aforementioned fields, often resulting in deceleration and increased instabilities which can increase overall beam loss.

The most general description of impedance can be likened to an RLC circuit with a driving voltage where the impedance is given by,

$$Z = \left[\frac{1}{R} + \frac{1}{iLw} + iCw \right]^{-1} \quad (4.39)$$

Where R is the resistance, C is the capacitance, L is the inductance and w is the frequency of the voltage.

The main elements that contribute to the impedance effects are often the acceleration structures know as RF (Radio Frequency) cavities [60], and so is the focus of the simulations in the subsequent chapters. The next section will further introduce and explain the function of RF Cavities.

4.2.2 RF Cavities

To begin we must recall our discussion surrounding Equation 4.1. Specifically that we were able to neglect the electrostatic field in the Lorentz force equation, and that the magnetic field does not accelerate or decelerate the beam. In this section we will do the opposite and focus on the contribution of the electric field. To do this we must introduce the main mechanism of beam acceleration, RF (Radio Frequency) cavities.

The first type of larger scale beam acceleration was simply using an electric field produced by a changing magnetic field in an accelerator called the betatron. The betatron could accelerate electrons up to about 300 MeV before the field in the magnetic yoke became saturated [61]. RF cavities were the answer to moving past the betatron limit. In general, to accelerate particles using an RF field a series of drift tubes with gaps in between them are excited by a time varying RF field. As particles pass through the drift tubes they are insulated from the electric field, and if the RF is synchronized with the pas-

sage of the particle bunches through these tubes, they can be made to see an accelerating electric field as they pass through the gaps [61].

The RF cavities in the Recycler Ring are resonant cavities filled with ferrites surrounding a beam pipe with a ceramic insulation gap in the center. The cavity is designed such that a uniform electric field can be applied to the ceramic gap that can either accelerate or decelerate the beam. The cavity is designed to resonate at a certain frequency and therefore the excitation across the gap is sinusoidal. Whether a particle in the cavity is accelerated depends on where it is located relative to the gap and whether the zero crossing of the RF excitation has been synchronized with the center of the bunch. Figure 4.4 illustrates this concept, commonly called longitudinal focusing. If the particle is centered on the gap it will ideally feel no force. This particle is referred to as the synchronous particle [6].

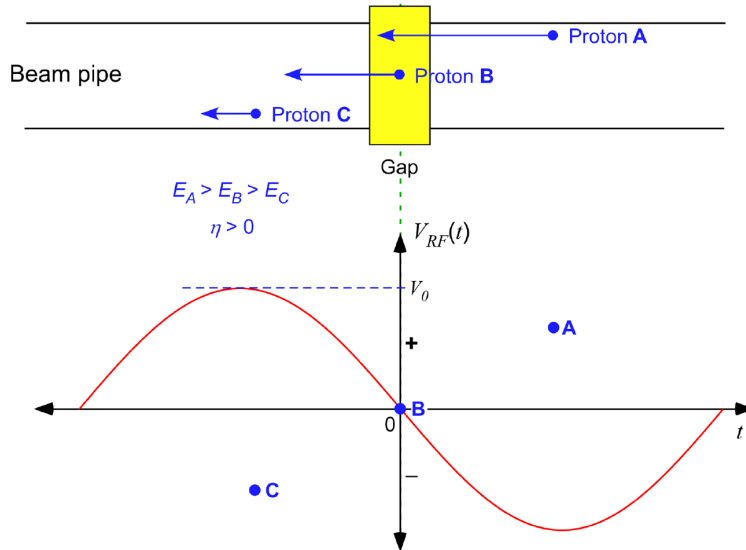


Figure 4.4: Longitudinal focusing of beam particles depending on their position relative to the center of the non-conducting gap indicated by the yellow rectangle in the top image. Proton A is decelerated and proton C is accelerated, effectively condensing the beam in the longitudinal direction [6].

The RF “bucket” is defined as a stable region formed in longitudinal phase space by the RF cavity voltage. The period of the cavity voltage describes the length in time of the bucket and the bucket height is proportional to the magnitude of the voltage signal. Particles outside the bucket are unbound and bounded particles inside the bucket are

considered a “bunch” of particles. The number of RF buckets a given system contains is determined by its harmonic number which is the ratio of the RF frequency to that of the revolution frequency,

$$h = \frac{f_{RF}}{f_{rev}} \quad (4.40)$$

The boundary defining the bucket is called the separatrix and will be mathematically described by the equations of motion in the following section.

4.2.3 Equation of Motion

The RF voltage can be described by a sine wave $V_{RF}(t) = -V_0 \sin \omega_{RF} \delta t$, where V_0 is the amplitude of the RF waveform, $\omega_{RF} = 2\pi h f_{rev}$, is the angular frequency, f_{rev} is the revolution frequency, h is the harmonic number and δt is the time of a particle relative to the time of the synchronous particle which defines $t = 0$. The energy change associated with a particle arriving δt later than the synchronous particle with momentum p and electric field E_s is,

$$\Delta E = \int \frac{dp}{dt} dt = e \int E_s dt = e V_{RF} \quad (4.41)$$

$$\Delta E = -e V_0 \sin \omega_{RF} \delta t \quad (4.42)$$

It is useful to describe this equation in n turns through the synchrotron, where $\Delta E_{n+1} = E_{n+1} - E_n$ and the RF phase for a given turn is related to the change in time as,

$$\phi_n = \omega_{RF} \delta t_n \quad (4.43)$$

The change in the energy can also be written in terms of the change in energy relative to the synchronous particle, $\Delta E_{n+1} = \delta E_{n+1} - \delta E_n$, because $E_n = E_0 + \delta E_n$. Setting this equation equal to Equation 4.42 produces the energy gain of a particle relative to the synchronous particle for a given turn through the accelerator,

$$\delta E_{n+1} = \delta E_n - e V_0 \sin \phi_n \quad (4.44)$$

In a similar fashion the time coordinate can be manipulated to show that $\delta T_{n+1} = \delta t_{n+1} - \delta t_n$, where δT_{n+1} is the change in the period of a non-synchronous particle for a given turn.

Substituting Equation 4.43 into the expression for δT_{n+1} and rearranging produces the relationship between the phase of the non-synchronous particle and its revolution period,

$$\phi_{n+1} = \phi_n + 2\pi h \frac{\delta T_{n+1}}{T_0} \quad (4.45)$$

This can be rewritten in terms of the revolution frequency if so desired.

The next step is to rewrite Equation 4.45 in terms of the energy change per turn to get a second equation like Equation 4.44. Consider the following equation from relativistic kinematics $E^2 = (E_0)^2 + p^2 c^2$, c is the speed of light and p is the particle momentum. This can be differentiated and rewritten as $dE = v dp$ where v is the velocity of the particle. Rewriting in the turn-by-turn notation and noting that $p = mv = \beta\gamma E_0/c$, where β is the velocity divided by the speed of light and γ is $1/\sqrt{1 - \beta^2}$, we can obtain a relationship between the change in energy and momentum of the non-synchronous particle,

$$\frac{\delta E_{n+1}}{E_0} = \beta_0^2 \frac{\delta p_{n+1}}{p_0} \quad (4.46)$$

To continue, momentum compaction, α , must be introduced. This describes the relationship between the length of a particles orbit and its momentum,

$$\alpha = \frac{dL/L}{dp/p} \quad (4.47)$$

If a particle is slightly shifted in momentum, it will have a different velocity and also a different orbit length, L . The revolution frequency of the beam is $f_{rev} = c\beta/L$. This can be differentiated and written as,

$$\frac{df_{rev}}{f_{rev}} = \frac{d\beta}{\beta} - \frac{dL}{L} \quad (4.48)$$

Using relativistic kinematics $p = \gamma\beta mc$. Again differentiating,

$$\frac{d\beta}{\beta} = \frac{1}{\gamma^2} \frac{dp}{p} \quad (4.49)$$

substituting Equation 4.49 into Equation 4.48,

$$\frac{df_{rev}}{f_{rev}} = \left(\frac{1}{\gamma^2} - \alpha \right) \frac{dp}{p} \quad (4.50)$$

Where α can be written as $1/\gamma_t^2$ where γ_t^2 defines the transition energy of an accelerator: $E_t = \gamma_t mc^2$. This energy marks a boundary where dp/p no longer depends on frequency. Equation 4.50 means that the change in revolution frequency depends on the particle energy and may possibly change sign during acceleration. Particles at the start of acceleration get faster in the beginning and arrive earlier at the RF cavity location (particle C in Figure 4.4), while particles that travel near the speed of light will not get faster any more but rather get more massive and, being pushed to a dispersive orbit, will arrive later at the cavity. The accelerator “slip factor” is,

$$\eta = \frac{1}{\gamma_t^2} - \frac{1}{\gamma^2} \quad (4.51)$$

The transition energy marks a boundary where η is zero, meaning there is no change in revolution frequency for particles with small momentum deviation. If η is positive the accelerator is considered to be operating above transition, and if negative it is operating below transition. Above transition, machines have a lower revolution frequency, the particles are close to the speed of light and the velocity does not change significantly anymore. Below transition, machines have a higher revolution frequency and the particles are increasing in velocity. An accelerator can also pass through transition. However at transition, particles that are not synchronous will have the same nominal turn-by-turn energy gain, and if transition is not passed quickly these particles will continue to increase in energy until they are lost and the longitudinal emittance is destroyed. The RR operates below transition and the DR operates above [6].

Now going back to Equation 4.46 and substituting in Equation 4.50

$$\frac{\delta E_{n+1}}{E_0} = -\frac{\beta_0^2}{\eta} \frac{\delta f_{n+1}}{f_0} \quad (4.52)$$

Finally using Equation 4.45 in terms of the revolution frequency and noting that $\omega_{RF} = 2\pi h f_0 = 2\pi h/T_0$, the relationship between the energy and phase can be written as,

$$\phi_{n+1} = \phi_n + \frac{2\pi h \eta}{\beta_0^2 E_0} \delta E_{n+1} \quad (4.53)$$

Converting Equation 4.53 and Equation 4.44 to time derivatives involves taking advantage of the fact that these are turn-by-turn quantities and the derivative of them with

respect to turn number are related to their time derivatives by,

$$\frac{dA}{dn} = A_{n+1} - A_n = T_0 \frac{dA}{dt} \quad (4.54)$$

because $t = nT_0$. This produces two coupled differential equations,

$$\frac{d\phi}{dt} = \frac{\omega_{RF}\eta}{\beta_0^2 E_0} \delta E \quad (4.55)$$

$$\frac{d\delta E}{dt} = -eV_0 f_0 \sin \phi \quad (4.56)$$

Differentiating Equation 4.55 and substituting the right hand side of Equation 4.56 for δE produces,

$$\frac{d^2\phi}{dt^2} - \frac{\omega_{RF}\eta}{\beta_0^2 E_0} \frac{d\delta E}{dt} = 0 \quad (4.57)$$

$$\frac{d^2\phi}{dt^2} + \frac{\omega_{RF}^2 \eta e V_0}{2\pi h \beta_0^2 E_0} \sin \phi = 0 \quad (4.58)$$

4.2.4 Particle Trajectories

To derive the particle trajectories in longitudinal phase space we must derive the Hamiltonian in terms of the equations of motion. Namely, using ϕ and $\delta E/\omega_{RF}$ as the canonical variables and we can write,

$$\frac{d\phi}{dt} = \frac{\partial H}{\partial t}, \quad \frac{d(\delta E/\omega_{RF})}{dt} = -\frac{\partial H}{\partial \phi} \quad (4.59)$$

The Hamiltonian can be written as,

$$H(\phi, \delta E) = \frac{1}{2} \frac{\omega_{RF}^2 \eta}{\beta_0^2 E_0} \left(\frac{\delta E}{\omega_{RF}} \right)^2 + \frac{eV_0}{\pi h} \sin^2 \frac{\phi}{2} \quad (4.60)$$

The trajectories of the particles in longitudinal phase space are defined by $H(\phi, \delta E) = \text{constant}$. The problem becomes determining the constant value. Defining $\delta \hat{E}$ as δE when ϕ is zero and $\hat{\phi}$ as ϕ when δE is zero, we can substitute and solve for $\delta E(\phi)$,

$$\delta E(\phi) = \pm \sqrt{\delta \hat{E}^2 - \frac{2\beta_0^2 e V_0 E_0}{\pi h \eta} \sin^2 \frac{\phi}{2}} \quad (4.61)$$

$\delta \hat{E}$ bounds the motion of a proton in a bucket relative to the synchronous energy. This can also be expressed in terms of the maximum phase deviation $\hat{\phi}$,

$$\delta \hat{E} = \beta_0 \sqrt{\frac{2eV_0 E_0}{\pi h \eta}} \sin \frac{\hat{\phi}}{2} \quad (4.62)$$

These are the equations that determine the motion of a proton inside an RF bucket and will be featured in further discussions about simulation work for the Recycler Ring presented here.

Chapter 5

Mu2e and the Fermilab Accelerator Complex

The sensitivity goal set by Mu2e requires an extremely intense muon beam. To ensure the Mu2e experiment hits this goal, the accelerator complex at Fermilab will be required to generate huge numbers of muons by colliding a proton beam with a target.

This method of producing a large number of muons, rather than focusing on accelerating them to the highest energy, marks a significant step in the Intensity Frontier. A second-phase, upgraded Mu2e experiment could utilize a proposed high-intensity upgrade to Fermilab's proton accelerator, that would increase the production of muons by one to two orders of magnitude.

However, the Fermilab accelerator complex has seen many experiments, on all the frontiers of physics, including at one time being home to the largest accelerator in the world, the Tevatron. The Tevatron required near constant production and storage of antiprotons, for which much of the current accelerator complex was solely built. However, during the Tevatron era, it would have been impossible to generate the desired beam structure for Mu2e.

At the end of the antiproton operations in 2011, the Fermilab antiproton production complex consisted of a sophisticated target system, three 8 GeV storage rings (namely the Debuncher, the Accumulator and the Recycler), 25 independent stochastic cooling systems and the world's only relativistic electron cooling system. The accelerator complex

at Fermilab supported a broad physics program including the Tevatron Collider Run II, neutrino experiments, as well as a test beam facility and other fixed target experiments using 120 GeV primary proton beams [12]. Much of this history informs the current state and operation of the complex today. In the following sections we will take a closer look at the past and specifics of each portion of the accelerator complex in the context of the Mu2e experiment.

5.1 Fermilab Accelerator Complex

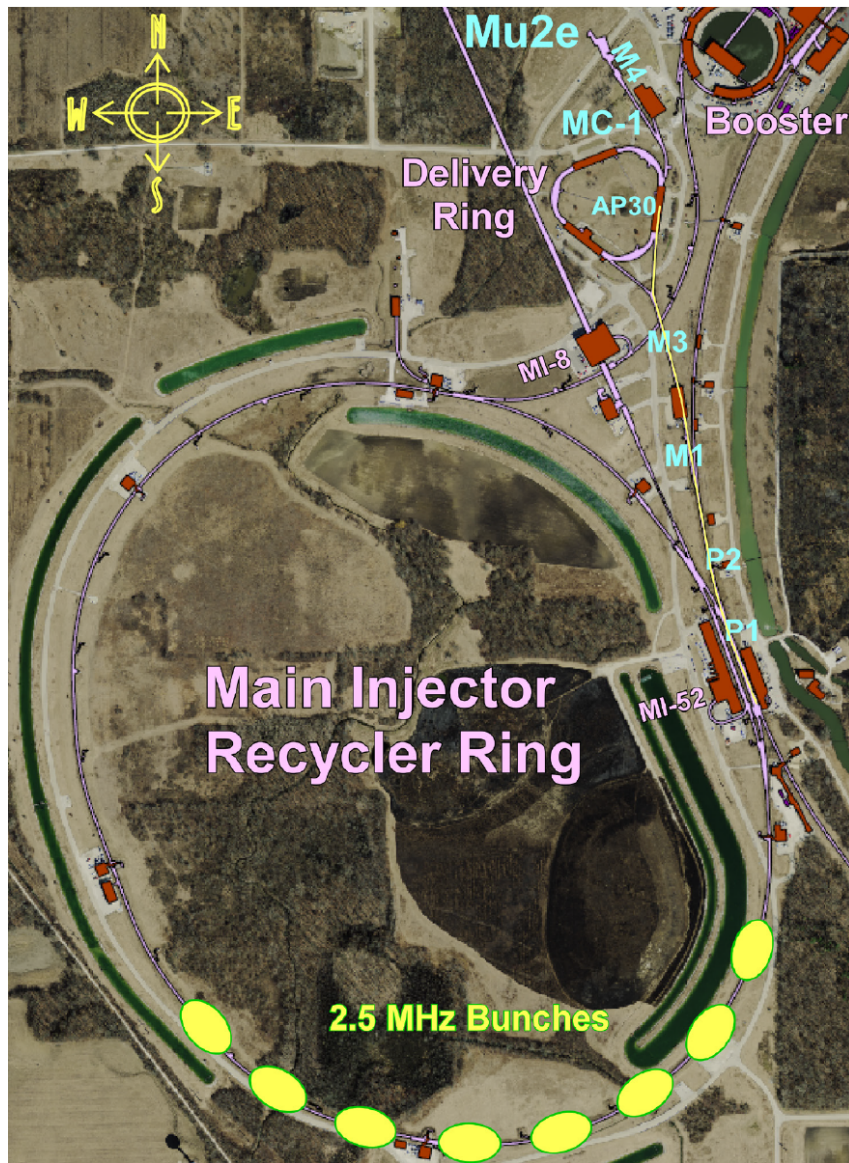


Figure 5.1: Fermilab accelerator complex.

A diagram of the accelerator complex is shown in Figure 5.1. Each step of the bunching, injection/extraction and acceleration process contributes to the end extinction goal of 10^{-10} . The protons begin their journey as hydrogen ions “sputtered” from the surface of a cathode in preaccelerators, and end their journey as an extremely short pulse of intense 8 GeV protons.

5.1.1 Ion source, Preaccelerator and Linac

The proton beam starts its life in the ion source and Preaccelerator just before being injected into the Fermilab Linac. The Preaccelerator is a Radio Frequency Quadrupole (RFQ) that accelerates and focuses low energy hydrogen ions (H^-) from the ion source using a precisely shaped electric field. These ions reach 750 keV and are chopped into bunches and injected into the Linac. The motivation for using negative ions will be discussed shortly.

5.1.1.1 Ion Source

The ion source at FNAL produces ~ 60 mA H^- ion pulses, 0.2 ms in duration, with a 15 Hz repetition rate. Figure 5.2 shows a schematic view of the FNAL Magnetron ion source. This Ion source is cesiated, in which cesium is mixed with the gas to produce hydrogen ions. FNAL has been using Magnetron ion sources to supply the LINAC with hydrogen ions since 1997 [11].

An electrical discharge in the Magnetron electrode configurations generates a plasma from which ions can be extracted. A low-pressure gas is fed into the space between the electrodes. The electrical discharge is created by applying an electric potential between the anode and cathode shown in Figure 5.2. The resultant electric field accelerates free electrons, which can ionize the gas molecules. This process is called electron impact ionization [62].

5.1.1.2 RFQ

RFQ preaccelerators have almost completely replaced their much larger Cockcroft-Walton counterpart, which Fermilab used to solely rely on for ion acceleration until 2012 [11]. RFQ accelerators require less energy to operate and boast a lower cost of maintenance than Cockcroft-Walton preaccelerators. In addition, ion sources need only to operate

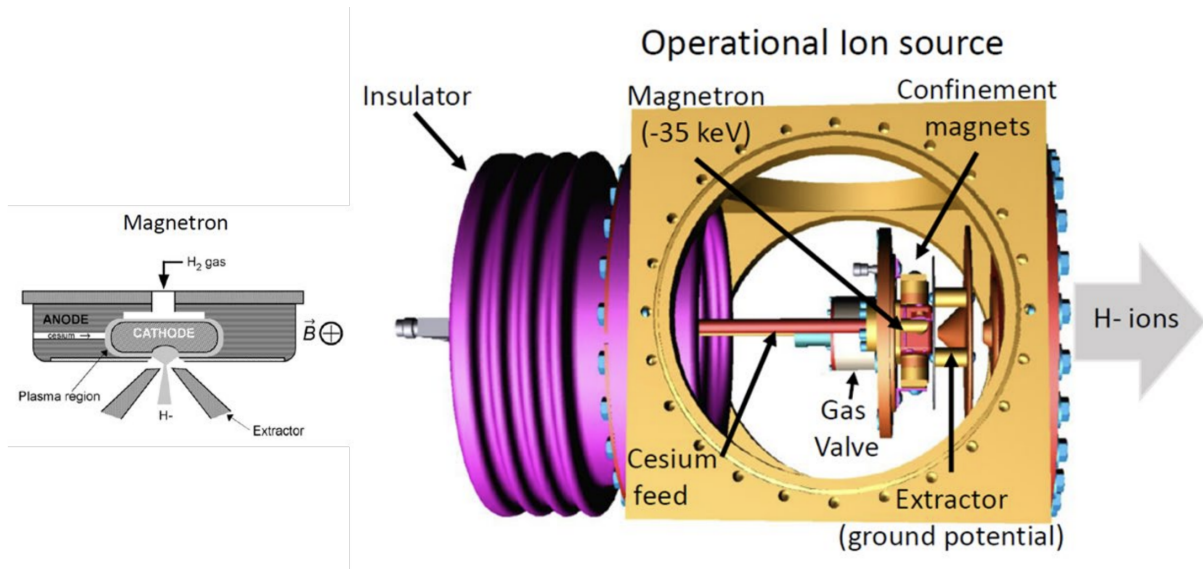


Figure 5.2: FNAL Magnetron schematic (left) and actual installation (right). The cathode runs down the central axis of the anode [11].

at relatively low extraction voltage and preacceleration voltages to inject into the RFQ. Drift-tube linacs like the one at Fermilab are well matched in energy for injection as well.

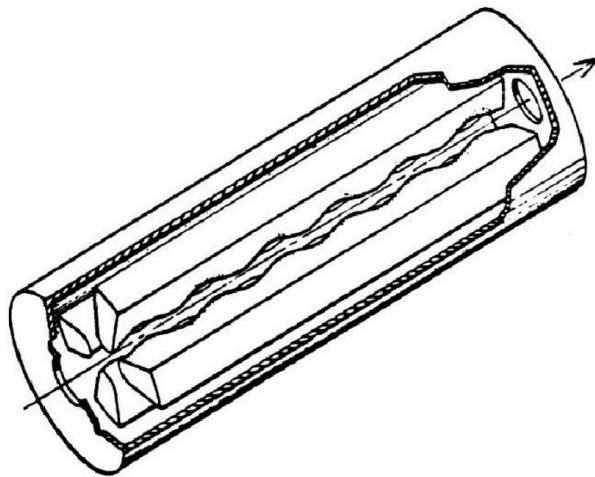


Figure 5.3: Cutout of a four-pole RFQ.

The RFQ accelerator, pictured in Figure 5.3, uses a transverse electrostatic field to focus the ions, and a longitudinal electrostatic field to accelerate the ions. The transverse alternating gradient focusing results from the changing polarity of the RF field as the ion travels down the axis. The acceleration is created by the slight perturbation to the field

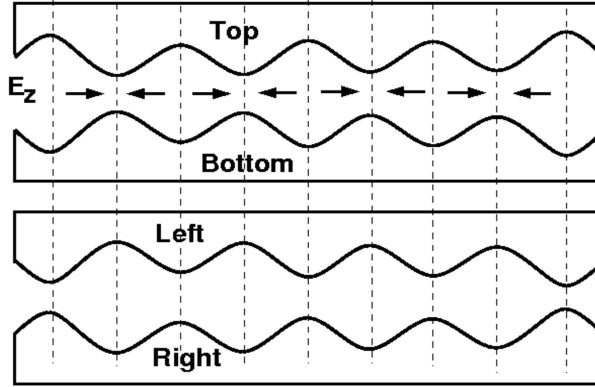


Figure 5.4: Close up of the RFQ vane tip with the longitudinal component of the electric field indicated by E_z .

provided by the ripples on the poles of the quadrupole (vane tip) as pictured in Figure 5.4. The phase of the wiggles in the top and bottom vanes are out of phase from those on the left and right vanes. This creates an alternating longitudinal field along which the ions are accelerated and injected into the Linac.

5.1.1.3 Linac

The first part of the Fermilab Linac is of the drift tube type and is based off of the original design by Luis Alvarez. The drift tubes are conducting cavities that effectively shield the beam from accelerating fields as mentioned in Section 4.2.2. The acceleration takes place in-between each tube where an electric field propels the ions into the next drift tube. The length of the tubes increases with the particle velocity. A 1993 upgrade to the Linac added on seven additional Klystron powered RF cavities capable of operating at higher accelerating gradients that produce ions at a final energy of 400 MeV. The upgraded section has a more efficient “pi-cavity” design and operates at 805 MHz as opposed to the old system which operates at 201 MHz. The particles are then injected into the Booster over multiple turns [63].

5.1.2 Booster

The Booster is a synchrotron that accelerates the 400 MeV beam to 8 GeV which it then delivers to the Recycler Ring (RR) or Main Injector (MI). The Booster was designed and built in favor of a direct injection to the MI from a Linac at the time, because the Linac

required to accelerate hydrogen ions from 400 MeV to 8 GeV would have had to be about 4 miles long. In addition, it would have been very difficult and expensive to design a MI ring with an injection energy of 400 MeV. In part due to the repercussions of adiabatic damping, discussed in Section 4.1.3. Namely as the proton beam is accelerated, the transverse size decreases, so to inject beam at low energy, you need a very large aperture, leading to very large stored energy - and therefore cost and complexity - at the highest fields. In addition magnets are designed to operate at the highest fields (currents). As the current is lowered, eventually hysteresis currents in the iron will result in magnetic anomalies, leading to instabilities in the beam. Hence the Booster was born [64].

The Booster receives negative ions over multiple turns. During injection, a set of bumping magnets move the circulating negative ions out, such that it passes through the stripping foil that removes the electrons. The Booster is designed to deliver “batches” of protons to the RR at a rate of 15 Hz. Continuously operated resonant power supplies control the RF cavities and magnets in the Booster. The Linac beam is injected at the minimum of the sinusoid excitation and extracted at the peak. In the heyday of the Tevatron, the MI accelerated this beam to 120 GeV and created anti-protons that were then injected into the Tevatron for a collision or into the RR for storage [6, 64].

5.1.3 Recycler Ring

The Recycler Ring is an 8 GeV permanent magnet storage ring located in the same tunnel as the MI. It was originally used to store and “cool” anti-protons for use in the Tevatron. The RR began circulating protons for the NuMI and NO ν A experiments for slip stacking and injection into the MI to increase the beam power from 400 kW to 700 kW [65]. Mu2e will not use the RR for slip stacking, but rather to create a high intensity beam for muon production. The RR has two RF systems one at 53 MHz and a second at 2.5 MHz. The lower frequency system is used to capture the protons injected from the Booster and is slowly turned off as the 2.5 MHz system is ramped up. Seven booster batches can fit longitudinally around the circumference of the Recycler but only two will be used in the Mu2e experiment. After re-bunching, these intense bunches of 10^{12} protons are extracted to the Delivery Ring (DR) one at a time. The fractional number of particles between

each bunch of protons needs to be at most 10^{-5} in the Recycler to satisfy the final goal of 10^{-10} . The re-bunching process as well as the machine impedance is potentially two of many causes for the degradation of the extinction requirement [6]. Currently, the fraction of the inter-bunch to total bunch particles are well above the 10^{-5} level [19]. This statement will be further discussed in Chapter 9.

5.1.4 Delivery Ring

The DR is the last synchrotron the protons in the Mu2e experiment will see. The DR is a 505 m storage ring that receives a single 2.5 MHz bunch from the Recycler every 48.1 ms. It contains a 2.36 MHz RF system that synchronously captures the transferred bunch into one of its four RF buckets. The transfer of the bunches from the RR to the DR must be carefully considered, such that each transferred bunch will be centered in a DR bucket. This is complicated by the slight discrepancy in the RF of the two rings. The DR circumference is not harmonically related to that of the RR, meaning the circumferences are not integer multiples. This potentially further degrades the fractional out-of-time beam and therefore the final intensity of the resulting proton pulse. The reason for this mismatch is due to the original purpose of the Delivery Ring, or the Debuncher Ring as it once was known, which was a crucial part of the antiproton source for the Tevatron.



Figure 5.5: Picture of the Debuncher (outer ring) and the Accumulator (inner ring) [12].

The Debuncher and Accumulator pictured in Figure 5.5 were two storage rings housed in the same tunnel that were used to cool antiprotons after their creation for storage.

Both the Debuncher and Accumulator had particular features needed for cooling and accumulating antiprotons with stochastic cooling systems. 53 MHz bunches of antiprotons would enter the Debuncher from the transport line and a 53 MHz RF system was used for the bunch rotation and debunching of the antiprotons into a continuous beam with a low momentum spread. The 2.36 MHz RF system provided a barrier bucket to allow a gap for extraction to the Accumulator [12].

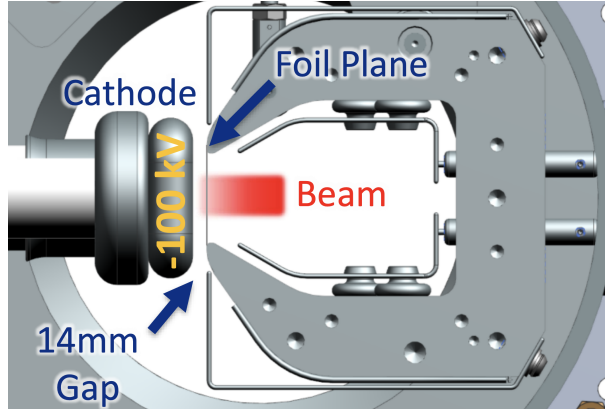


Figure 5.6: Schematic of the electrostatic septum. The beam is shown in red and the cathode is held at -100 kV [13].

The Delivery Ring also contains the resonant extraction system that produces the slow 43 ms spill of the proton beam to the M4 beamline and finally the Mu2e production target. The resonant extraction system contains two electrostatic septa (ESS) pictured in Figure 5.6, which consists of two beam channels separated by a grounded foil. The beam is driven to resonance just before entering the ESS and the high amplitude beam is sheared off between the foil and a 100 kV cathode effectively separating the beam into two. Both beams will then pass through a quadrupole which will not deflect beam on the central orbit, but that will increase the separation between the stable and unstable beam trajectories. These will then pass through a second electrostatic septum and quadrupole magnet, before entering a Lambertson magnetic septum that will eject the extracted protons into a beam line that leads to the Production target [66].

5.1.5 M4 Beamline

The M4 beamline contains the extinction system which is a series of three collimators and two dipole magnets, called the AC Dipole. This system will be responsible for reducing the fraction of out-of-time beam by an additional factor of 10^{-5} and will be discussed further in Chapter 7. The AC dipole will horizontally deflect out-of-time beam into the final downstream collimator while leaving the in-time beam untouched. A cartoon of the components in the M4 beamline are shown in Figure 5.8. The tail collimator primarily serves to remove the tail of the beam created from scattering off the ESS foil. The halo collimator removes higher amplitude beam that could otherwise be corrected into the transmission channel when the beam is deflected by the AC Dipole.

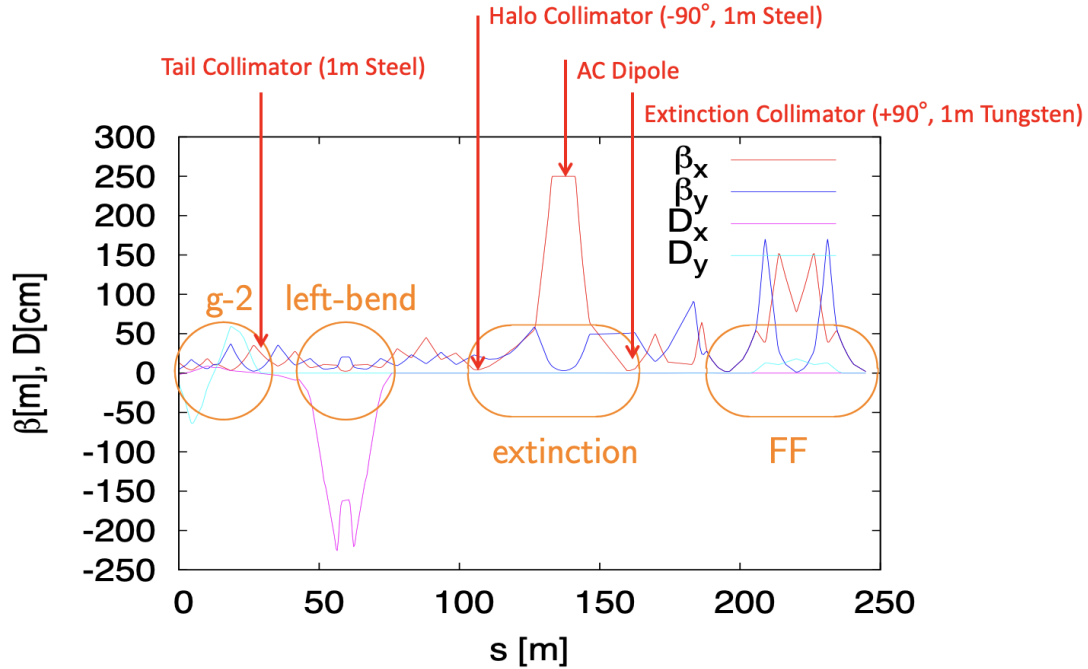


Figure 5.7: Transverse beam line optics as simulated by MADX for the M4 line Where β is the beta function and D is the dispersion function. FF is the final focus area [4].

Figure 5.7 shows the transverse optics for the M4 line. The beta function at the AC Dipole is at a maximum in the bend plane, which is around ~ 250 m. The phase advance between the AC Dipole and the two closest collimators is 90° so the beam that has been deflected by the dipole will hit the downstream collimator, the extinction collimator. After deflection the beam encounters the final focus (FF) area that consists of quadrupoles that

are used to make the bunch as small as possible before it encounters the production target.

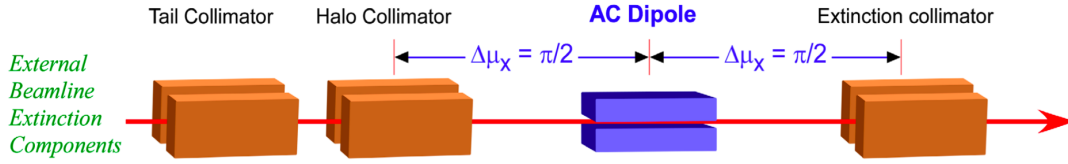


Figure 5.8: Physical layout of the beam line components in the M4 beamline. $\Delta\mu_x$ is the horizontal betatron phase [6].

The final result of all the beam extraction and cleaning described here will be realized in the form of short 250 ns pulses shown in Figure 5.9. These pulses are separated by 1.7 μs and will allow the Mu2e experiment to define a data taking window outside of which the detectors can be effectively blinded to incoming muons.

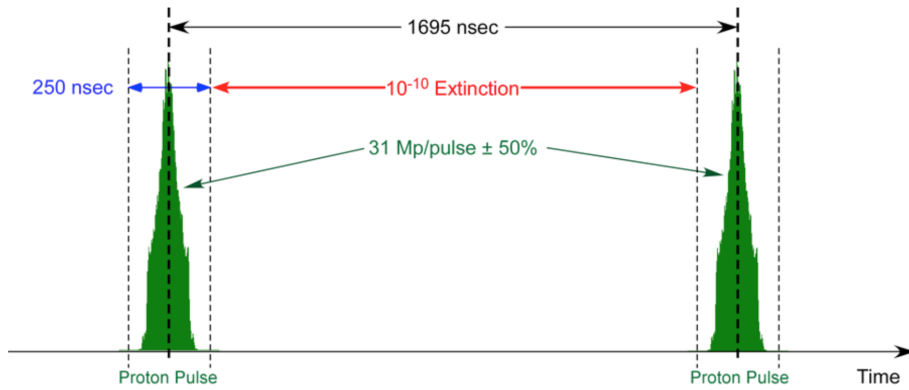


Figure 5.9: Pulse structure required by the Mu2e Experiment. The requirement that there be no protons outside of the nominal pulse width above the 10^{-10} fractional level is referred to as “Extinction” [6].

Chapter 6

Extinction

As mentioned previously the requirement that the out-of-time beam be reduced to a fractional level of at least 10^{-10} is the “Extinction” requirement. More specifically,

$$\text{Extinction} = \frac{\text{number of out - of - time protons striking the production target}}{\text{total number of protons striking the production target}} \quad (6.1)$$

where in-time protons are defined to be within ± 125 ns of the center of the proton pulse. The 10^{-10} level was determined through simulation of background events many of which are the result of out-of-time protons mimicking the conversion signal. If successful these steps will allow the resonant extraction system to produce very clean 250 ns wide pulses separated by 1.7 μ s, where the large separation in time between the pulses is to allow stray captured muons with a lifetime of 846 ns to decay away while the beam is “off”. The most likely channel for such backgrounds comes from a pion making its way down the beam line, stopping in the stopping target, and undergoing radiative pion capture (RPC), as discussed in Section 3.1.2. The photon from RPC can pair produce in the target, emitting an electron near 105 MeV that can fake a conversion electron. There are many ways in which the Extinction requirement is achieved throughout the experiment. In fact, the process starts in the accelerator itself and can be separated into two main parts:

- The technique for generating the required bunch structure in the Recycler Ring naturally leads to some amount of extinction. Altogether, an extinction of 10^{-5} is expected as the proton beam is extracted and delivered.

- The M4 beam line contains a system of resonant magnets and collimators, including the AC Dipole, that will provide an additional extinction of 10^{-7} or better. This level of extinction provides a buffer of two orders of magnitude, which is reasonable given the novelty of the system.

6.1 Bunch Formation

The 2.5 MHz system in the RR is adiabatically ramped to 80 kV in order to minimize fillamenting of the 53 MHz bunches. However the bunches still experience a significant amount of movement in the bucket. Figure 6.1 shows a simulation of the individual 53 MHz bunches in different colors in one Recycler bucket close to the extraction time. The 53 MHz bunches never have a chance to fully settle in the 2.5 MHz bucket.

Additionally, when the beam is extracted to the DR, because the circumferences of the RR and DR are not related by a whole number, aligning the injected bunch with the center of the DR bucket is nearly impossible, creating out-of-time beam beyond the required bunch level extinction of 10^{-5} [6].

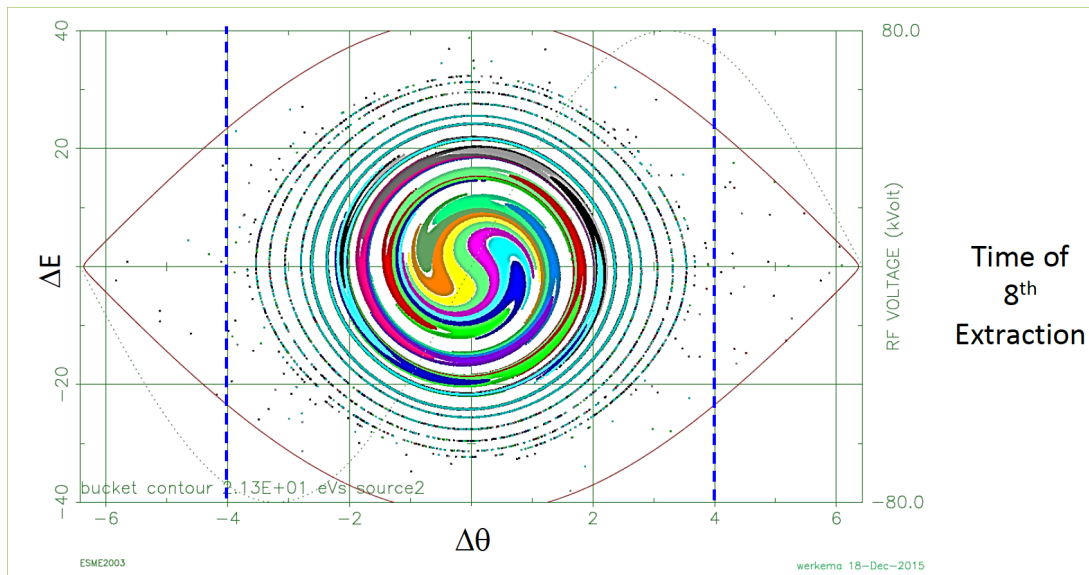


Figure 6.1: Simulated Recycler 2.5 MHz bunch in longitudinal phase space at the time of the last extraction. Each color corresponds to a 53 MHz bunch from the Booster. The dotted lines indicate the ± 125 ns window defining in-time beam [6].

The impedance or wakefields from the resonant elements along the beam line also

creates out-of-time beam. There are transverse and longitudinal wakefields, however, we will focus only on longitudinal wakefields and their effects for the following discussion. At a minimum, the beam is encased in a conducting vacuum tube as it travels through the accelerator. As a charge passes through a conducting element an image with the opposite charge is created in the surface of the conductor canceling out the field at the boundary of the conducting surface. However, if there is any variation in the chamber properties such as material or shape this perturbs the image and results in the beam losing some charge as it passes near the imperfect element. The fields produced by this left behind charge are known as wake fields. These wake fields can affect subsequent bunches that pass through that portion of the chamber resulting in the subsequent bunch seeing a beam induced voltage. Figure 6.2 shows what a wakefield created by a particle passing through a conducting element may look like.

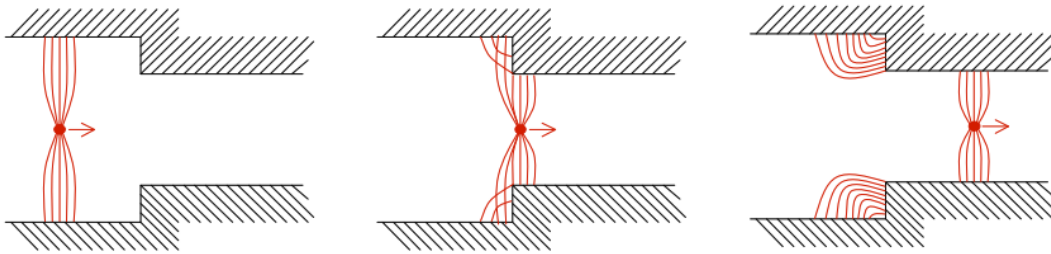


Figure 6.2: Simplistic view of a charged particle passing through a shaped cavity with electromagnetic field lines [14].

RF cavities are a large source of wakefields due to their shape, in fact they are designed such that the variation in shape produces an accelerating longitudinal field, albeit from an external excitation. These wakefields can be thought of as an impedance if converted to the frequency domain via a fourier transform. Longitudinal impedance can be conceptualized as a resonant circuit, where the cavity is an RLC circuit and the driving voltage is the RF power supply. Ultimately the impedance changes the energy of the particles in the beam causing a larger differential in accelerating voltage for some particle's, further spreading out the beam and destroying the emittance [14]. This concept is further discussed in Section 9.2.2.

Space charge is another factor in the production of out-of-time beam. This effect is

especially pronounced in intensity focused experiments such as Mu2e. Each bunch in the RR will consist of 10^{12} protons. Minimally, space charge effects arise due to inter-particle coulomb interactions. Mathematically this is realized by assuming a generic particle in the bunch experiences the collective Coulomb force due to fields generated by all the other particles in the bunch. This effect again can cause the bunch to increase in size via intrabeam scattering and will be further discussed in Section 9.2.2.

6.2 Beam Line Extinction

The beam line extinction system consists of a deflecting magnet and a collimation system, timed such that only the in-time beam makes it past the collimators. The most straightforward approach to achieve this would be a pulsed kicker magnet, which would deflect the in-time beam into the transmission channel. However, a kicker of sufficient amplitude and repetition rate is well beyond current magnet technology. The solution is a resonant system of two dipoles called the AC Dipole [67].

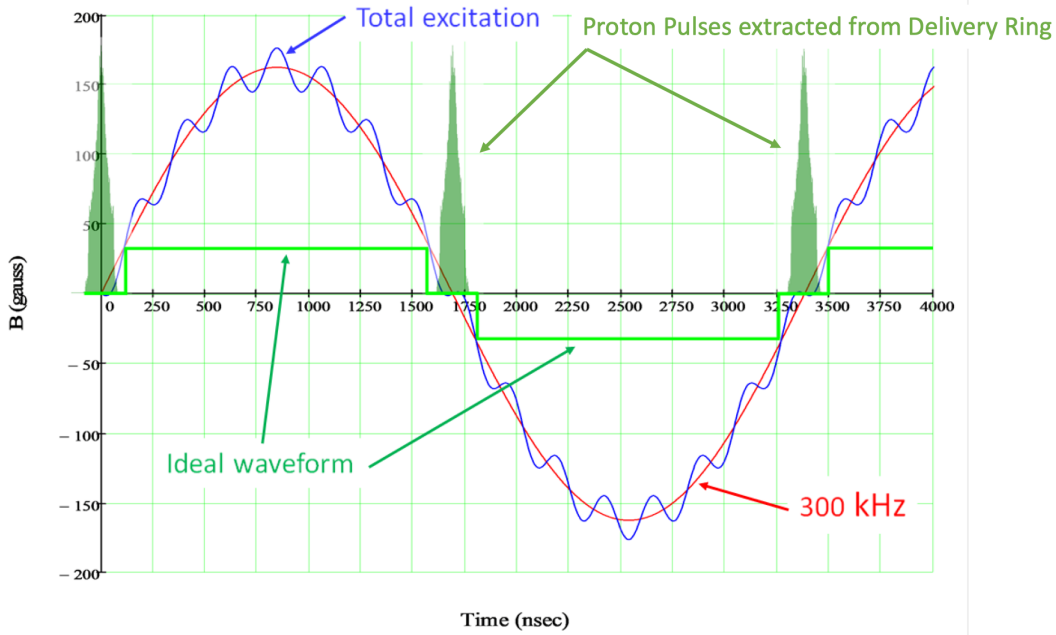


Figure 6.3: Time profile of the AC dipole field overlaid with the expected proton pulses separated by $1.7 \mu\text{s}$. The excitation of the AC dipole is achieved by sine waves at 300 kHz and 4.4 MHz [6].

The entire extinction section of the M4 beam line discussed in Section 5.1.5 is respon-

sible for sweeping and collimating the out-of-time beam to produce an additional 10^{-7} of extinction. The main portion of the extinction comes from the AC Dipole which is powered using a resonating power supply at 300 kHz and 4.4 MHz. An illustration of the excitation waveforms overlaid with the resulting proton pulses can be seen in Figure 6.3. The 300 kHz excitation deflects the majority of the out-of-time beam while the 4.4 MHz flattens out the zero crossing of the signal to ensure maximum transmission of in-time beam. The design of the dipole and the material chosen to facilitate this excitation will be further discussed in Chapter 7.

Chapter 7

AC Dipole

As previously mentioned it is expected that the delivery process of the protons will provide extinction at the 10^{-5} level [6]. A simulation presented here in Chapter 9 has attempted to reproduce this bunch structure in both in the Recycler and Delivery Ring. The remainder of the extinction will be provided by the AC dipole.

The AC Dipole will eliminate the fraction of out-of-time protons at the level of 10^{-10} or less. The magnets operate at 300 kHz and 4.4 MHz. Selection of magnetic ferrite material for construction has been carefully considered given the extremely high repetition rate and duty cycle that can lead to excess heating in conventional magnetic material.

A model of the electromagnetic and thermal properties of candidate ferrite materials has been constructed. Magnetic permeability, inductance, and power loss were measured at the two operating frequencies in toroidal ferrite samples as well as in the ferrites from which the prototype magnets were built. Additionally, the outgassing rates of the ferrite material was measured to determine vacuum compatibility. The outcome of this work, presented here, is a detailed specification of the electrical and mechanical specification of the ferrite material required for this application.

7.1 Extinction System

The effects of the extinction system in phase space are shown in Figure 7.1. As stated previously in Section 5.1.5, the AC Dipole will be responsible for kicking out-of-time beam into the extinction collimator. The requirement for total extinction can be realized

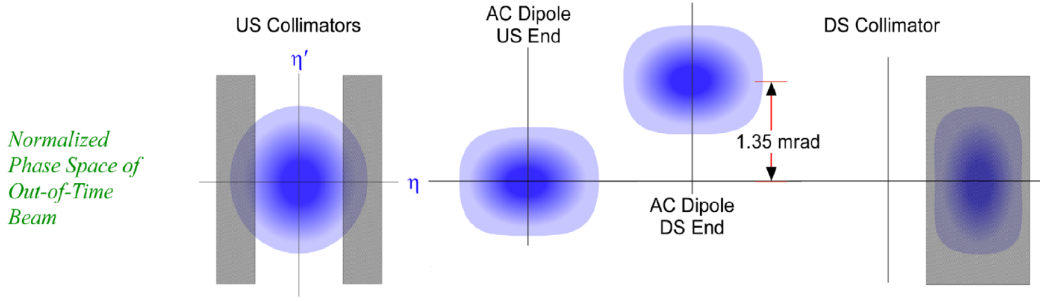


Figure 7.1: The phase space effects of the extinction system [6].

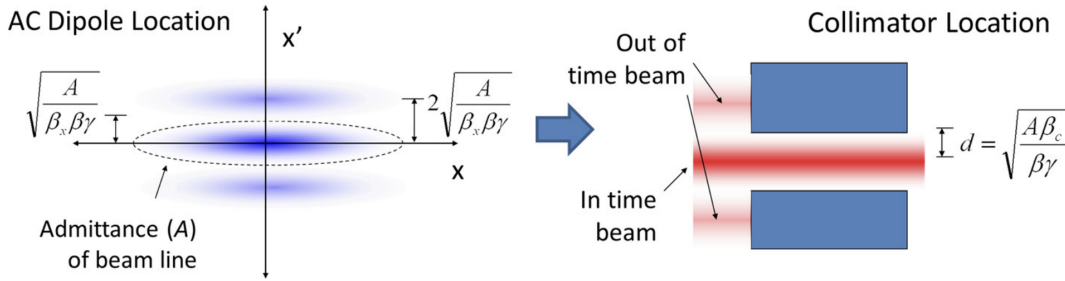


Figure 7.2: Effects of the AC Dipole in the bend plane phase space, where x' is the derivative of x as described in Section 4.1.3. The beam line admittance is indicated by the ellipse [15].

in terms of the angular deflection in the bend plane phase space by setting the admittance of the collimator, A , equal to the bounding emittance of the beam, previously discussed in Section 4.1.3,

$$\Delta\theta = 2\sqrt{\frac{A}{\beta_x\beta_\gamma}} \quad (7.1)$$

β and γ take their relativistic definitions and β_x is the horizontal betatron function, the significance of which is described in Section 4.1.3. This is actually twice the angular amplitude of the beam admittance, because a deflection of $\sqrt{\frac{A}{\beta_x\beta_\gamma}}$ would place the center of the beam at the edge of the collimator. A depiction of this angular distribution in phase space is shown in Figure 7.1 [15].

The required integrated field strength is given by the beam rigidity, which has been shown previously to be proportional to the particle momentum in Equation 4.2, multiplied

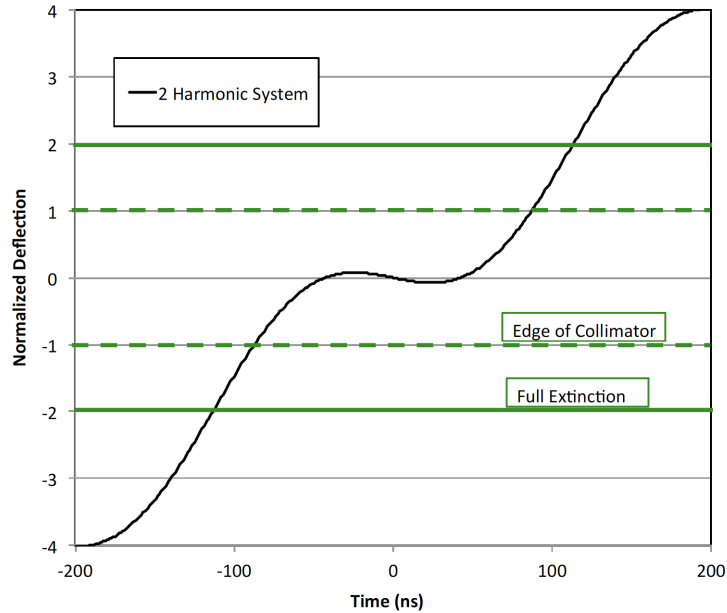


Figure 7.3: Normalized deflection amplitude as a function of time. The solid green line indicates the amplitude corresponding to total extinction, Equation 7.1, and the dotted green line indicates half this deflection. The black line represents a close up view at the zero crossing of the dual harmonic waveform used as the excitation [16].

by the angular deflection,

$$BL = (B\rho)\Delta\theta = 2(B\rho)\sqrt{\frac{A}{\beta_x\beta\gamma}} \quad (7.2)$$

Figure 7.3 shows the normalized angular deflection amplitude that is necessary to deflect the beam within the transmission window created by the excitation waveform.

7.1.1 AC Dipole Design

The design of the AC Dipole is constrained by many factors: bunch rate, transmission window, transmission efficiency for the proton beam, intensity of the proton pulses, cost and complexity. To satisfy the latter two requirements the stored energy of the magnet must be minimized as much as possible while maintaining the required field strength to deflect the beam [67]. The stored energy of a dipole magnet is,

$$U = \frac{1}{2\mu_0} B_0^2 g w L \quad (7.3)$$

Where g is the vertical gap size, L is the length and w is the full aperture of the magnet. w should take into account the beam size as well as the sagitta of the beam path as it is

deflected,

$$w = 2 \left(\sqrt{\frac{A\beta_x}{\beta\gamma}} + \frac{1}{2}\Theta L \right) \quad (7.4)$$

where Θ is the full amplitude of the angular sweep, described in Equation 7.1, scaled by the live window, τ , and period of the 300 kHz excitation, T . The live window is 250 ns and will occur at the zero crossings of the excitation. The angular sweep becomes,

$$\Theta = 2\sqrt{\frac{A}{\beta_x\beta\gamma}} \left(\frac{T}{\pi\tau} \right) \quad (7.5)$$

Plugging this into Equation 7.4,

$$w = 2\sqrt{\frac{A}{\beta\gamma}} \left(\sqrt{\beta_x} + \frac{L}{\sqrt{\beta_x}} \frac{T}{\pi\tau} \right) \quad (7.6)$$

The vertical gap g can be described by the vertical beta function, β_y , at a position s . For a large beta function in the horizontal plane there must be a “waist” in the beta function in the vertical plane. Ideally the minimum of the waist would occur in the center of the magnet, at $L/2$, so as to produce the minimum vertical beam size over the entire length of the magnet. These are the conditions expected at the AC dipole as will soon be shown. The evolution of the vertical beta function at a waist as a function of longitudinal distance, s , is,

$$\beta_y(s) = \beta_{y0} + \frac{s^2}{\beta_{y0}} \quad (7.7)$$

minimizing this at the center ($L/2$) of the magnet produces $\beta_{y0} = \frac{L}{2}$, $\beta_y(L/2) = L$. Producing a vertical gap equal to,

$$g = 2\sqrt{\frac{AL}{\beta\gamma}} \quad (7.8)$$

Plugging Equations 7.8 and 7.6 into Equation 7.3 we can see the relationship of the stored energy to the length of the magnet and the horizontal beta function,

$$U = \frac{8(B\rho)^2}{\mu_0} \left(\frac{A}{\beta\gamma} \right)^2 \left(\frac{T}{\pi\tau} \right)^2 \left(\frac{1}{L^{1/2}\beta_x^{1/2}} + \frac{L^{1/2}}{\beta_x^{3/2}} \left(\frac{T}{\pi\tau} \right) \right) \quad (7.9)$$

Where $B\rho$ is the beam rigidity and has been previously shown to be proportional to the beam momentum. Examining this equation we can see that the stored energy is inversely

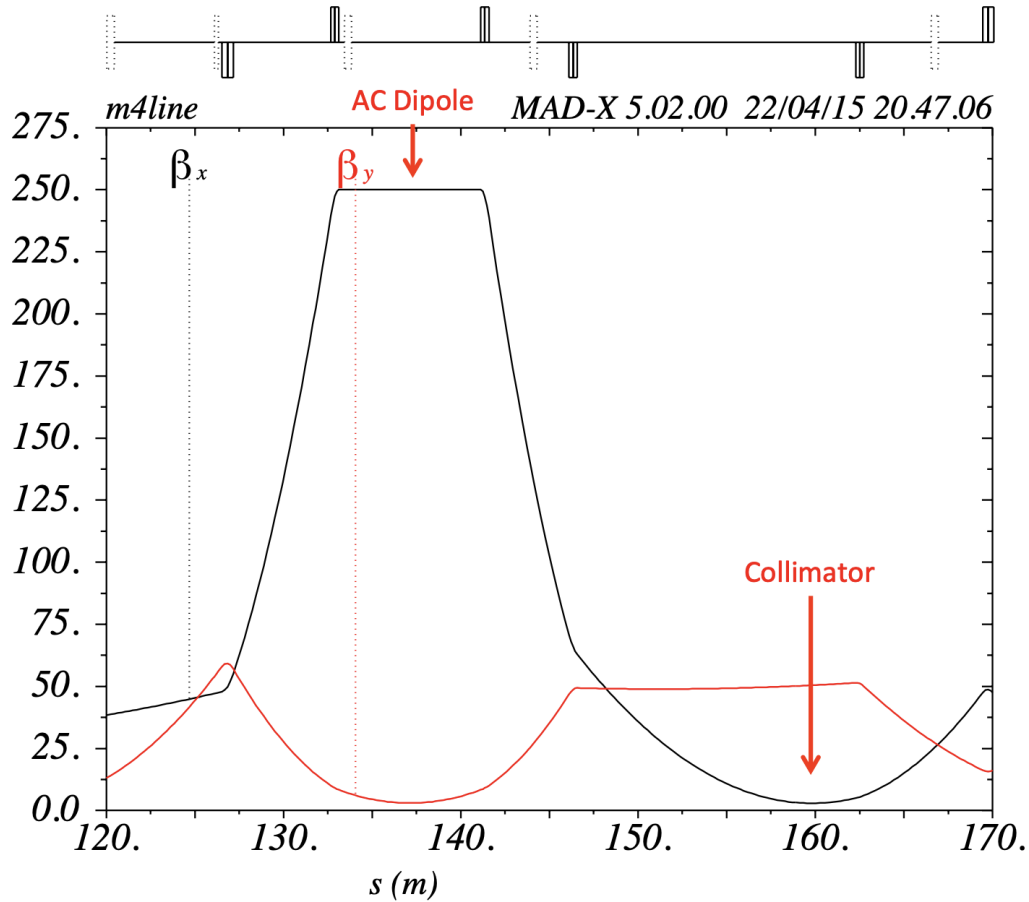
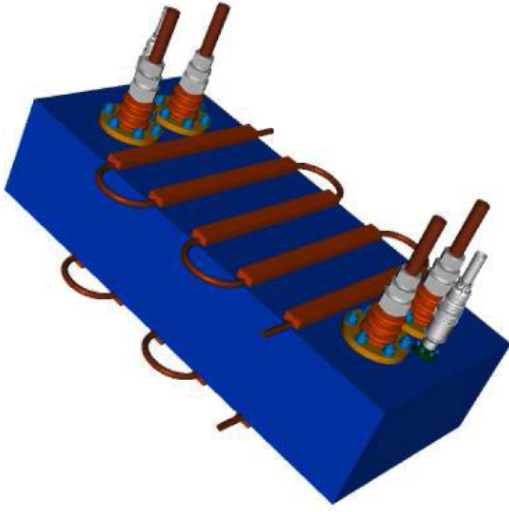
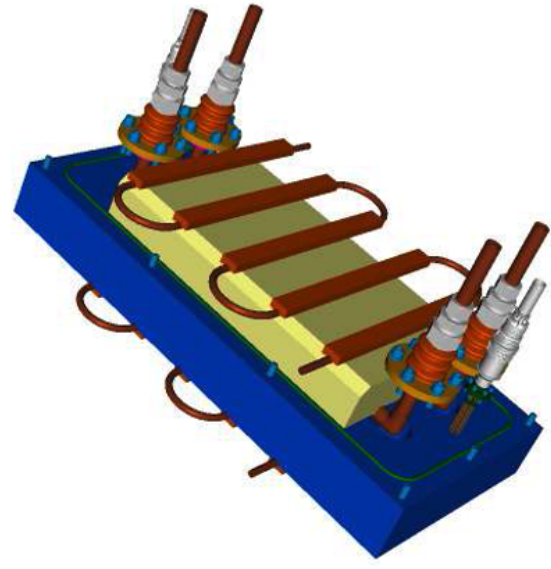


Figure 7.4: Beam optics in the region of the AC dipole and collimator [15].

proportional to the square root of the beta function, so the larger this quantity the less the stored energy. The stored energy has a weaker dependence on the length of the magnet, but because the field is inversely proportional to the length of the magnet, the larger the magnet the lower the stored energy. However, impractically large magnets are not feasible from a price or construction standpoint (regular dipole magnets are around 2 m in length). In addition, the beta function is constrained by the beamline which can produce a maximum beta function of 250 m. Figure 7.4 shows the output of a software program called MADX that has been used to tune these optics at the location of the AC Dipole producing a waist in the vertical plane, β_y , and a large beta function (250 m) in the horizontal plane [67]. The length of each of the magnets that make up the AC Dipole has been chosen to be 3 m with a field strength of 138 Gauss for the 300 kHz excitation and 12 Gauss for the 4.4 MHz excitation [16].



(a) Mock-up of the one meter AC Dipole prototype with the aluminum vacuum box in dark blue.



(b) Mock-up of the one meter AC Dipole prototype interior with the ferrites in dark blue.

Figure 7.5: Technical drawings of the AC Dipole prototype with (a) and without (b) the vacuum box. The four copper tubes on either side of the box act as the magnet coil and the water leads that cool the ferrites inside the box [17].

7.1.2 Prototypes

Half-meter and one meter magnet prototypes were constructed and are shown in Figures 7.5 and 7.6. The individual magnets in the AC Dipole itself will be divided into one meter segments with resonant caps between each section to reduce the voltage to ground level to 750 V [17]. While calculations of the magnet behavior during operation, such as power loss due to heating in the ferrite material, are possible using the manufacturers specifications, it was found early-on that these specifications were not accurate and unpredictable at the operating frequencies. In fact, identifying a ferrite that satisfies our requirements has proven surprisingly challenging and further testing was needed at this point to determine the correct material and magnet design.

Each of the prototypes confirmed a reasonable power loss, which for one-meter is around 1.6 kW at 300 kHz. Nevertheless, the measured power loss in both cases was higher than calculated using the vendor's material loss data. The field distribution was also measured as a function of brick and was found to be relatively flat for 4.4 MHz.

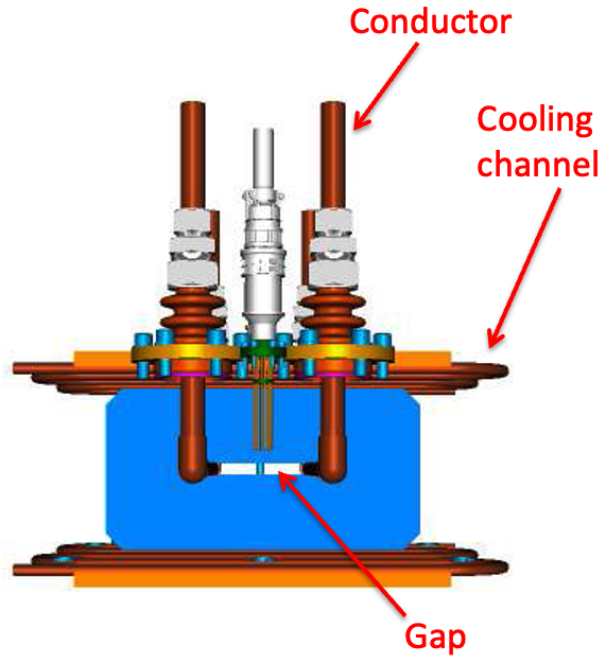


Figure 7.6: Beam-eye view of the AC Dipole prototype interior. The ferrites are in blue, the gap is 1.8 cm [17].

However, the field was found to concentrate around the copper leads and was further studied using simulation [18].

The main mechanism for predicting losses in magnetic material can be described by the magnetic permeability. The magnetic flux density, B , and the magnetizing field, H , are related by the magnetic permeability,

$$B = \mu\mu_0 H \quad (7.10)$$

Where μ is the magnetic permeability of the ferrite material, sometime called the relative permeability, and μ_0 is the permeability of free space. $\mu = \mu' - j\mu''$ is a complex number that depends on frequency and excitation and is related to power loss,

$$Q = \frac{\mu'}{\mu''} \quad (7.11)$$

where Q is the quality factor that in general relates the energy stored to the average power loss. Ferrite losses depend on many factors but losses due to material heating can be contributed to eddy currents in the material. However, this behavior can be

unpredictable, especially at higher frequencies and excitation level. For this reason there is no robust way of predicting the power and heating in the material.

Both the real and the imaginary parts of the ferrite permeability can change significantly with the amplitude of the magnetic field in the material. Resulting both in difficulties in interpretation of the measurement results and the increase of the power loss in a given high flux area. Figure 7.8 shows a spike in the simulated magnetic flux density around the curved area of the ferrite through which the copper tubing sits. A spatial distribution of the loss is shown in Figure 7.7.

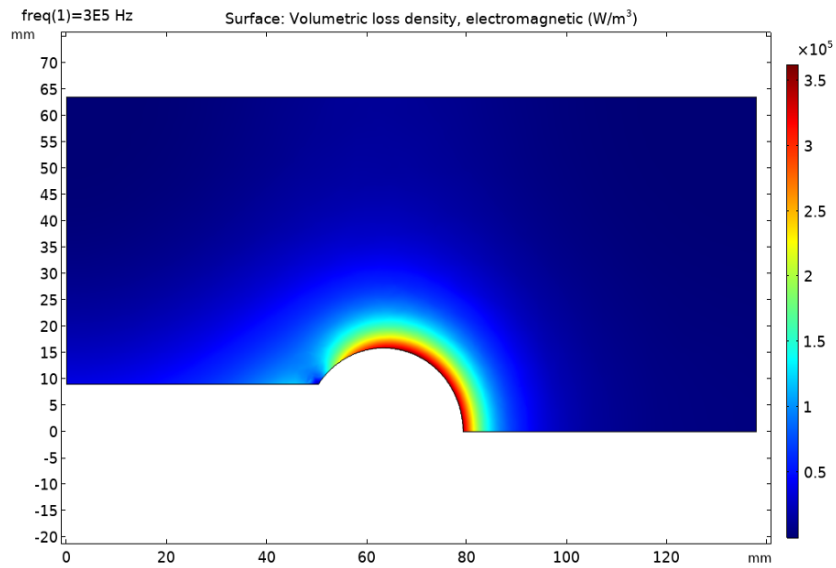


Figure 7.7: Volumetric loss density in Watts per cubic meter at 300 kHz as function of length in the one-meter magnet prototype simulation [18].

The spike in Figure 7.8 further motivates careful loss measurements and quality analysis of the selected ferrite material and provides a criterion for material selection. This criterion is described by the shape of the curve the permeability as a function of the magnetic field creates and the intersection with a line starting at the origin of the coordinate system tangent to a given permeability curve at a field strength, B . If the line is intersected only once the behavior of the material at higher field can be considered stable enough. Figure 7.9 shows three different permeability curves from three different ferrite samples. Ferrite material ‘E’ is the best candidate.

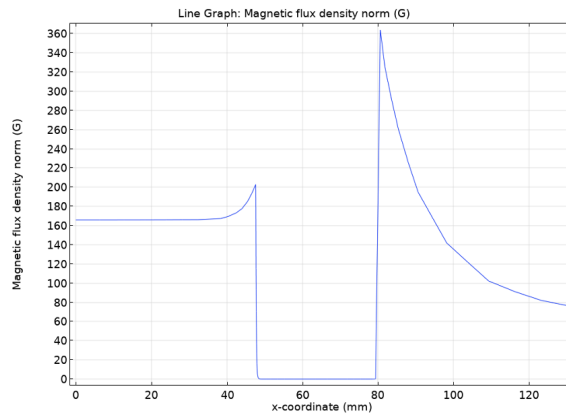


Figure 7.8: Magnetic flux density in Gauss as function of length at 300 kHz in the one-meter magnet prototype simulation [18].

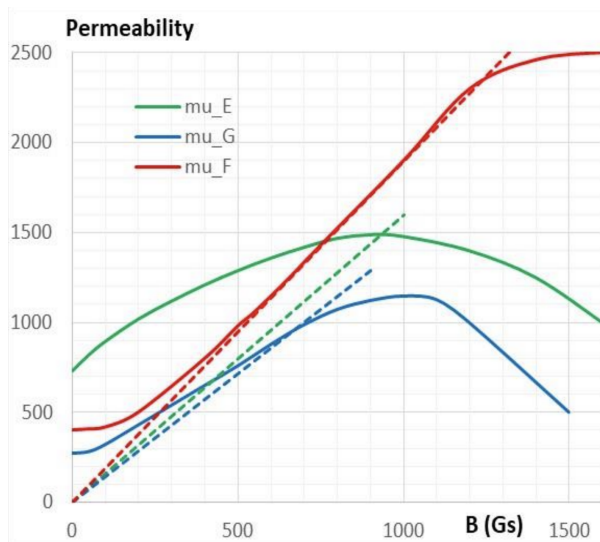


Figure 7.9: The real part of the measured permeability as a function of field strength for three different ferrite samples. The color coordinated dotted lines represent the lines through which the permeability may intersect only once [18].

Chapter 8

Ferrite Characterization

As previously mentioned excessive heating in a magnetic material can cause a severe change in its magnetic properties. While material E was previously found to be a viable candidate a new material with similar properties was selected for mass production of the bricks that will be used in the production magnets. A soft NiZn ferrite was chosen for its low coercivity and high curie temperature, resistivity and magnetic permeability. A rigorous characterization scheme of the magnetic properties of the bricks for each batch of ferrite material was devised.

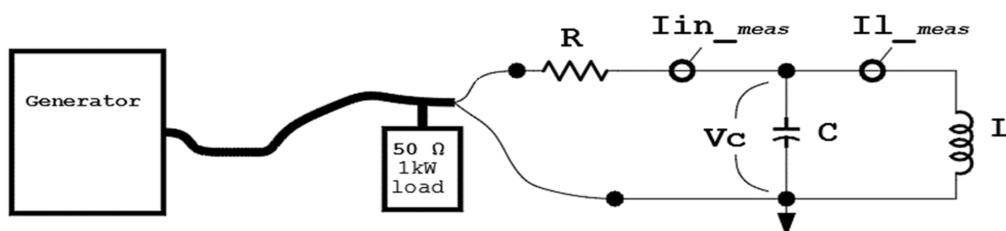


Figure 8.1: Circuit diagram for ferrite characterization.

Figure 8.1 describes the general circuit diagram used to measure the power loss in the ferrite material. It consists of a capacitor bank connected in parallel to the ferrite bricks that are arranged as shown in Figure 8.2 with a three turn copper coil. The resistor is used to reduce noise from the power amplifier. The 3500 W power amplifier and a signal generator were used to excite the ferrites.

The circuit can be made to resonate at the two relevant frequencies (300 kHz and



Figure 8.2: Overview of “dipole mode” circuit setup for ferrite characterization. A voltage, and two current probes in conjunction with an oscilloscope are used to measure the voltage across the capacitor bank, the current through the copper coil and the current into the circuit respectively.

4.5 MHz) by adjusting the capacitance,

$$\omega_0 = \frac{1}{\sqrt{LC}} \quad (8.1)$$

8.0.0.1 Dipole Mode

When the bricks are arranged in “dipole mode” as pictured in Figure 8.2, the power loss is calculated using the input current and the voltage. A point by point integration gives the power as a function of excitation. The excitation is calculated using the following

formula,

$$B_{pk-pk} = \frac{2NI_{ind-peak}}{\mu_0 g} \quad (8.2)$$

Where N is the number of turns in the copper coil, $I_{ind-peak}$ is the current in the copper coil and g is the gap between the ferrites which was 1.8 cm. This configuration is the closest to the actual arrangement of the bricks in the production magnet.

Figures 8.3 and 8.4 show the losses as a function of excitation field at each frequency. The power losses were found to be reasonable for the given field requirements and out of the over 300 bricks that will be used to make up the actual magnets, about 7% have been characterized in this way. Future work will include characterizing a larger percentage of the bricks as well as mechanically assessing the mating surfaces.

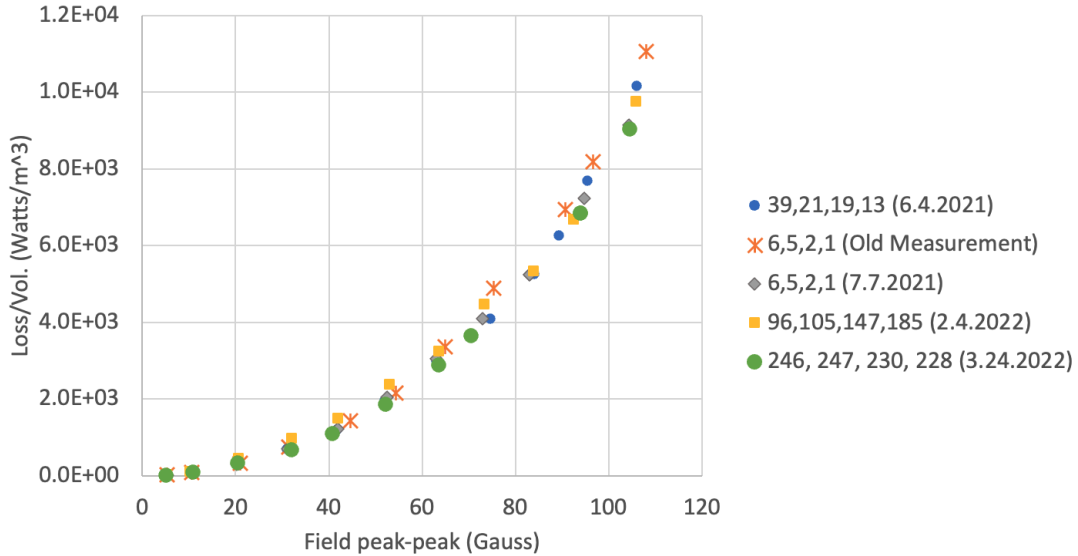


Figure 8.3: Dipole mode losses at 300 kHz, with 26.4 nF capacitance. The bricks were measured in groups of four and are labeled by their manufacturing number and date measured. At the field strength required by the magnet the ferrites will experience losses $\sim 15,000 \text{ W/m}^3$.

8.0.0.2 Toroid Mode and Permeability

In addition to the losses in “dipole mode” the losses and magnetic permeability measurements in “toroid mode” allow for further analysis at higher field and assessment in relation to the stability criterion. The toroid mode set-up differs only in general brick configuration, the same observables are measured as in dipole mode. Figure 8.5 (a) shows

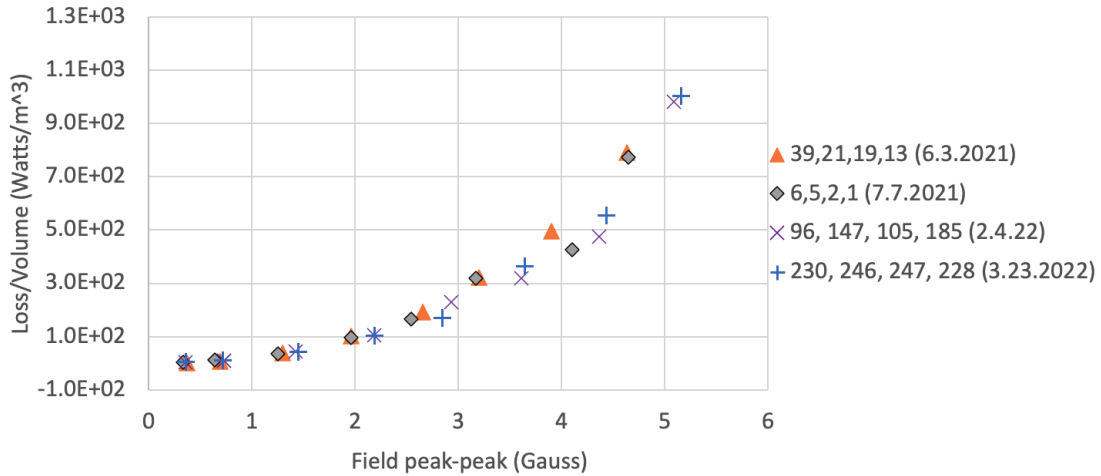


Figure 8.4: Dipole mode losses at 4.4 MHz, with 68 pF capacitance. The bricks were measured in groups of four and are labeled by their manufacturing number and date measured. At the field strength required by the magnet the ferrites will experience losses $\sim 1.000 \text{ W/m}^3$.

the toroid mode configuration. One procedural difference is the resonant frequency is much more sensitive to voltage increases and therefore the capacitance must be finely tuned at each step.

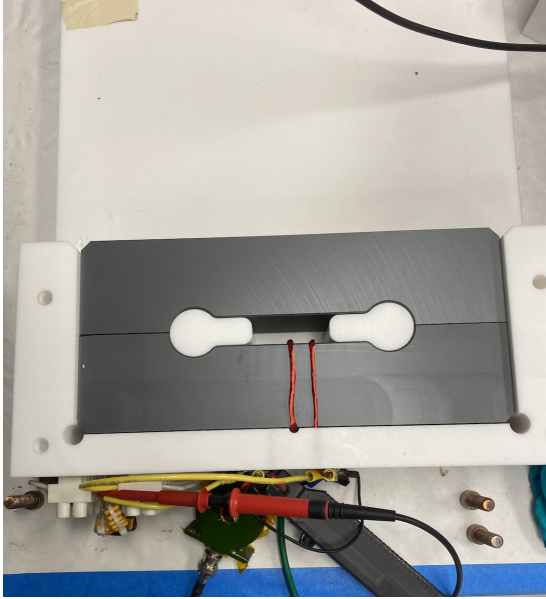
A non-magnetic measurement apparatus pictured in Figure 8.5 was constructed to hold the bricks in place and to make measurements easily repeatable. The red litz wire around the reference brick is connected to the capacitor bank. Again, voltage across the capacitors, current into the circuit and in the coil (or litz wire in this case) were measured and recorded using the same amplifier, signal generator and oscilloscope as in the dipole mode measurements.

The peak-to-peak magnetic field at a given voltage was calculated using the following formula.

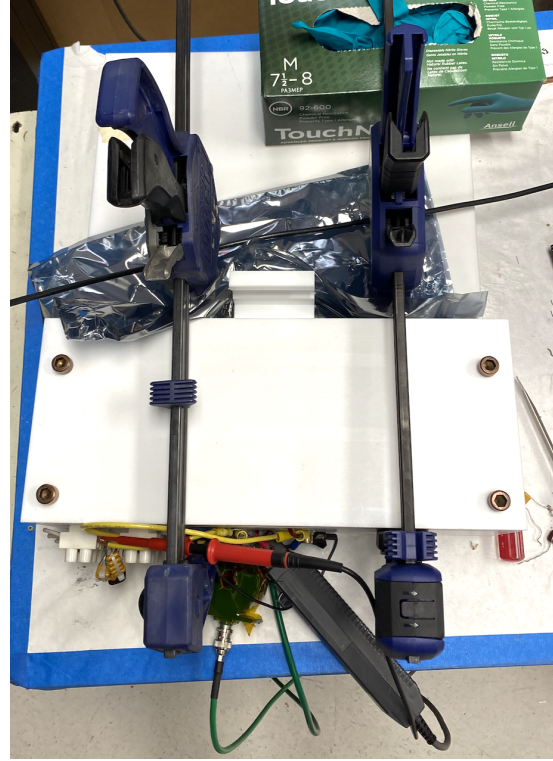
$$B_{pk-pk} = \frac{V_c N}{2\pi f A_{core}} \quad (8.3)$$

Where V_c is the peak-to-peak voltage across the capacitors, f is the frequency, N is the number of wire loops and A_{core} is the area of the core of the bricks configuration which was 30.4 cm^2 . The losses were calculated using the input current and the voltage across the capacitors, again using a point-by-point integration.

Figure 8.6 and Figure 8.7 show sample measurements of the toroid mode losses as a



(a) Top view with ferrite bricks inserted without lid. The red wire is litz wire and is looped twice around the reference brick.



(b) Top down view with lid and clamps holding the mating surfaces of the bricks firmly together.

Figure 8.5: Measurement apparatus that is used in toroid mode measurements. The ends of the litz wire were stripped and coated in solder for connection to the capacitor bank; which is located along with the current and voltage probes at the front of the apparatus.

function of field at the relevant frequencies. These are again reasonable in magnitude and display little deviation from one another.

The magnetic permeability is calculated by rearranging the formula for the inductance, L . For a true toroidal core the inductance would be,

$$L = \mu_0 \mu \frac{N^2 A_{core}}{2\pi R} \quad (8.4)$$

where μ is the relative permeability in which we are interested and R is the midpoint radius of the toroid core. For an approximation of the given geometry, ignoring the half

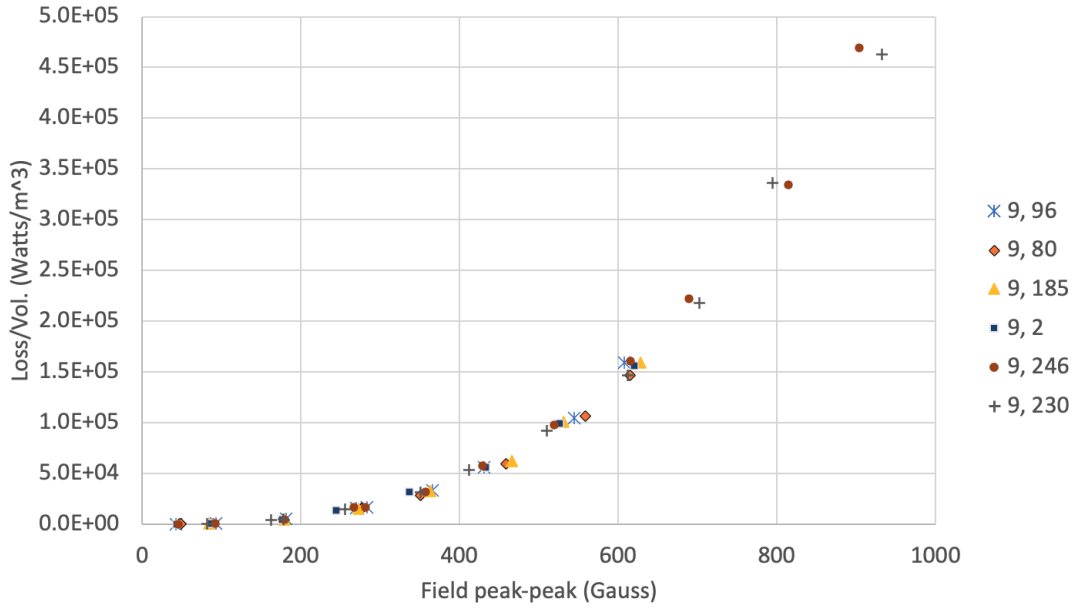


Figure 8.6: Sample of loss measurements at 300 kHz. The bricks were measured in groups of two in “toroid mode” and labeled by their manufacturing number. The reference brick was number 9. These measurements are in agreement.

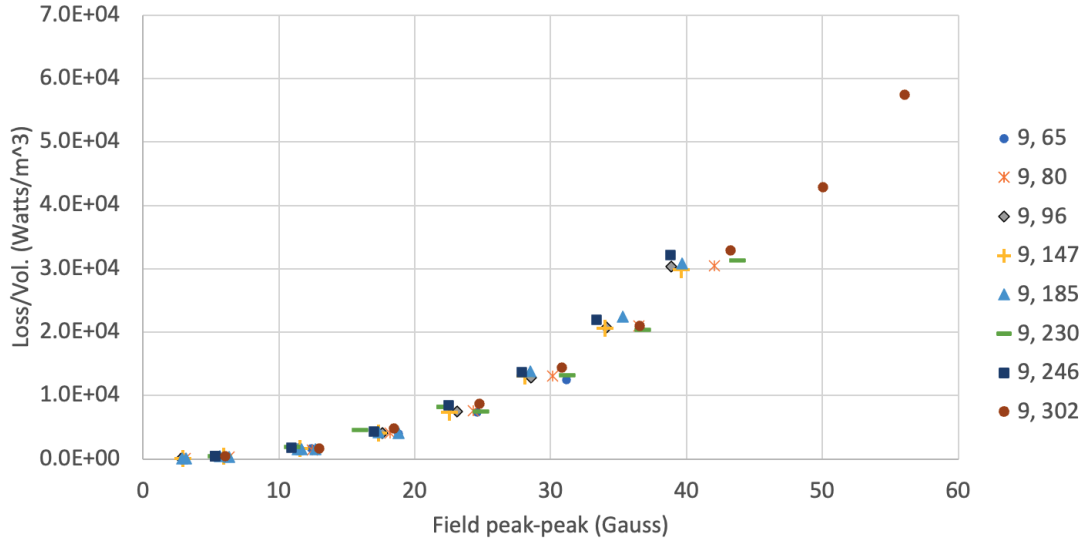


Figure 8.7: Sample of loss measurements at 4.4 MHz. The bricks were measured in groups of two in “toroid mode” and an labeled by their manufacturing number. The reference brick was number 9. These measurements are in agreement.

circle cut-outs in the bricks, the inductance can be written as,

$$L = \frac{\mu_0 \mu}{\pi} \left(-2(W + H) + 2\sqrt{H^2 + W^2} - H \ln \frac{H + \sqrt{H^2 + W^2}}{W} - W \ln \frac{W + \sqrt{H^2 + W^2}}{H} + H \ln \frac{4H}{d} + W \ln \frac{4W}{d} \right)$$

W	H	d
12.7 cm	27.6 cm	5.5 cm

Table 8.1: Two-brick toroid mode setup dimensions.

Where W is the width of the rectangular core shape, H is the height of the core and d is the thickness of the core. Table 8.1 displays the parameters used for this calculation.

The value of the inductance can be calculated from the measured parameters using the following formula,

$$L = \frac{V_c I_{coil}}{2\pi f} \quad (8.6)$$

Where I_{coil} is the measured current in the wire. Now, using Equation 8.5 and solving for $\mu_0\mu$ we can assess the bricks through the lens of the stability criterion. Figure 8.8 shows a small sample of the measured permeability of brick pairs as a function of magnetic field. The same reference brick was used for each measurement. It is clear from the flat almost concave shape of the measurement samples shown in Figure 8.8 that the stability criterion mentioned in Section 7.1.2 is satisfied.

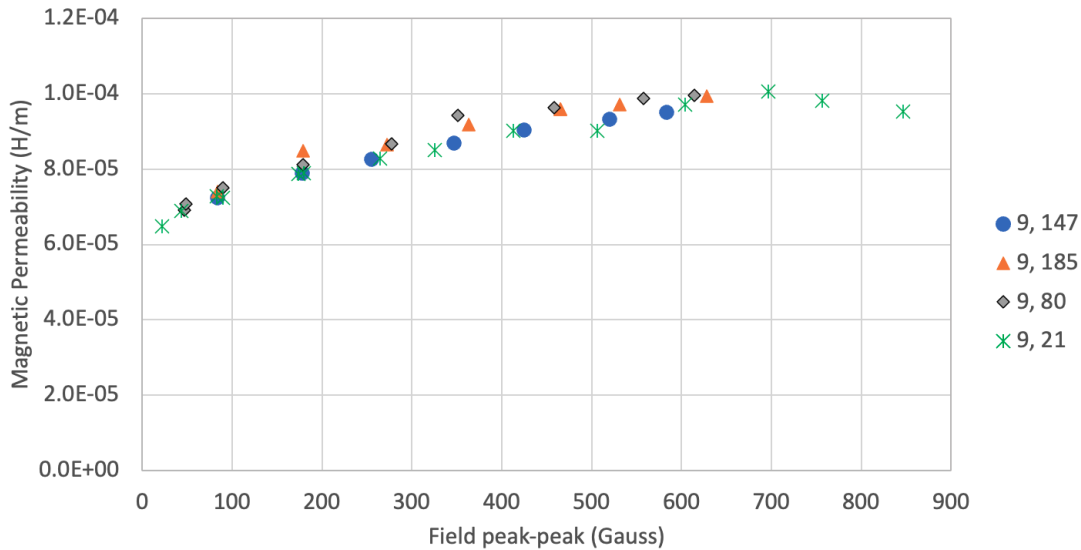


Figure 8.8: Sample of magnetic permeability measurements at 300 kHz. The bricks were measured in groups of two in “toroid mode” and an labeled by their manufacturing number. The flat almost concave shape clearly satisfies the stability criterion previously described in Section 7.1.2.

Chapter 9

BLoND Simulations

The bunch structure of the beam before the protons are extracted from the Delivery Ring, play a large role in the success of the extinction system and therefore the success of the Mu2e experiment as a whole. As mentioned in Section 5.1.3, there is strong evidence that the current state of the beam out of the DR does not exhibit the required extinction level of at least 10^{-5} . Understanding the bunch structure is the first step to mitigating any potential factors that may disrupt the extinction requirement. The current state of the beam is presented here as motivation for a novel simulation of the bunch structure in the Recycler Ring using the Beam Longitudinal Dynamics (BLonD) code [68]. The simulation includes new studies and comparative analysis of the machine impedance.

9.1 Current State

The longitudinal time profile of eight bunches after exiting the DR is pictured in Figure 9.1. The vertical black dotted lines in the figure indicate the 250 ns window that defines in-time beam. This data was recently taken from the T0 detector at the g-2 experiment, and provides insight into the current state of the proton beam that Mu2e will be using. The g-2 experiment uses the same general bunch structure that the Mu2e experiment will use and the experimental hall sits adjacent to the Mu2e building where the M4 beam line sits.

While we trust the timing structure of the beam profile from g-2 to be very similar to that expected in the Mu2e experiment, there are several differences in the g-2 beam

delivery that will be described here. Similar to Mu2e, protons with 8 GeV kinetic energy are transported to a muon production target at AP0. The AP0 target hall was formerly used to produce antiprotons for the Tevatron. 16 proton pulses, each with 10^{12} protons and 120 ns in length, arrive at the g-2 target. Positively charged particles with a momentum of 3.1 GeV/c are selected using a bending magnet. Secondary beam leaving the target will travel through the M2 and M3 lines which are designed to capture as many muons with momentum 3.094 GeV/c from pion decay as possible. The beam will then be injected into the Delivery Ring and the muon beam will be extracted into the M4 line, and finally into the M5 beamline which leads to the storage ring of the Muon g-2 Experiment [69].

Delivery of a clean muon beam that has a pion contaminant fraction below 10^{-5} , with no protons present, is a key requirement as these hadrons could cause a hadronic “flash” at injection. For this reason the DR is used to “clean” the beam by simply completing several revolutions before being sent to the storage ring. This provides enough time for all pions to decay into muons before being sent to the storage ring [69].

Although the g-2 beam consists of muons, the time structure accurately reproduces that of the proton beam used to create it. Additionally, the beam intensity for g-2 is four to five times less than that of Mu2e [20].

The T0 detector measures the time profile of the beam using a scintillator, a silicon photo multiplier (SiPM) detector and two vertically oriented photo-multiplier tubes at the entrance of the g-2 storage ring. Figure 9.2 shows the placement of the T0 detector relative to the g-2 storage ring and Figure 9.3 and Figure 9.4 show a diagram of the detector setup and the actual detector before installation, respectively. The PMTs are attached to guides that direct the light from the charged particles interaction with the scintillator. The two PMTs are tuned to be linearly sensitive to the main beam injection and the SiPM is tuned to be sensitive to low-intensity beam leakage during out-of-injection times. Neutral-density filters are inserted in front of each PMT, these allow a controlled amount of light to enter the PMTs.

The primary purpose of the T0 detector is to provide a time reference for the arrival of muons into the g-2 storage ring. By accurately measuring the muon arrival time, the

T0 detector helps synchronize the timing of various detectors in the experiment. The T0 detector also acts as a beam quality check for the experiment. The integral of the pulses in each PMT can be used to measure the number of muons entering the storage ring. If the arrival time or the intensity is low these events can be removed from the g-2 data.

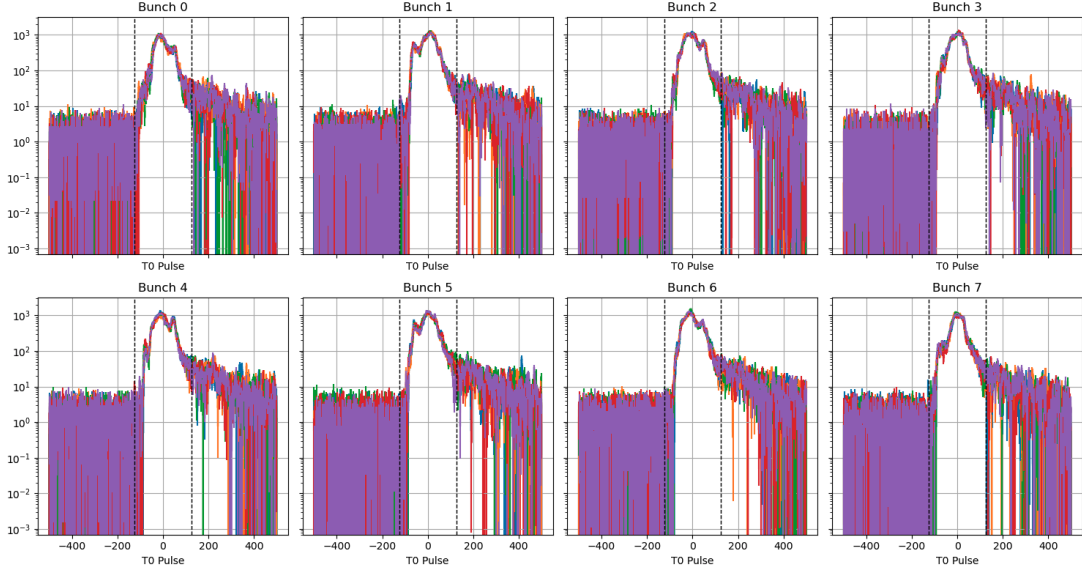


Figure 9.1: 8 bunches are extracted from the DR and then injected into the g-2 storage ring. The plots above show the time profile of these 3 GeV muon bunches just before they enter the storage ring as measured by the T0 detector. The detector consists of a scintillator attached to two vertically aligned PMTs. The y-axis is the PMT amplitude on log scale. The logarithmic scale better shows the magnitude of the out-of-time beam, which is indicated by the counts lying outside of the vertical dotted lines in each histogram. Each histogram has 11 traces overlaid [19] [20].

The current fraction of out-of-time beam as measured by the T0 detector lies around 10^{-2} , three orders of magnitude greater than the target level for Mu2e at this point, which is 10^{-5} . Figure 9.1 depicts the time profile of 8 bunches the y-axis

Results from a 2019 beam study in the Recycler are shown in Figure 9.5. This figure shows the longitudinal time profile and intensity of proton bunches in the Recycler over time. The y-axis can be thought of as the number of turns through the accelerator system scaled by an arbitrary factor. Where zero corresponds to the time when the beam is first injected into the RR and the rebunching cycle begins. The x-axis is the longitudinal (azimuthal) position of the bunches as they travel through the accelerator. This coordinate

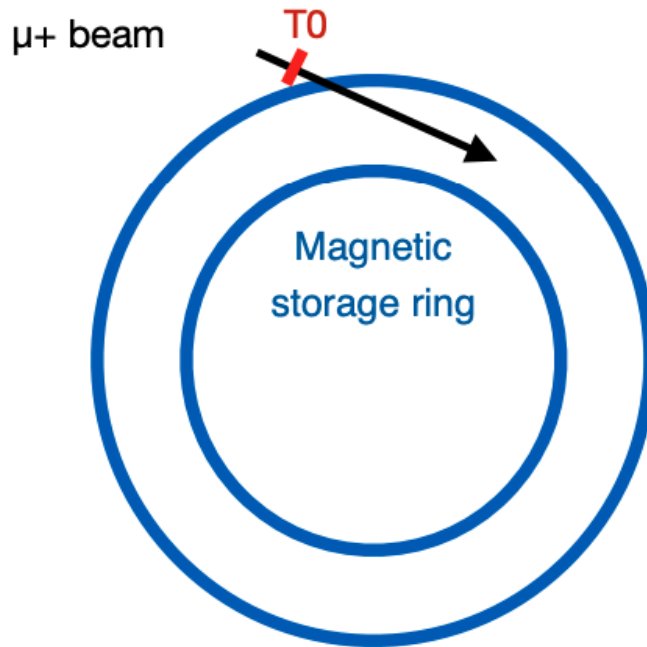


Figure 9.2: The T0 detector location. Just before entering the g-2 storage ring the muons will encounter the T0 detector [19].

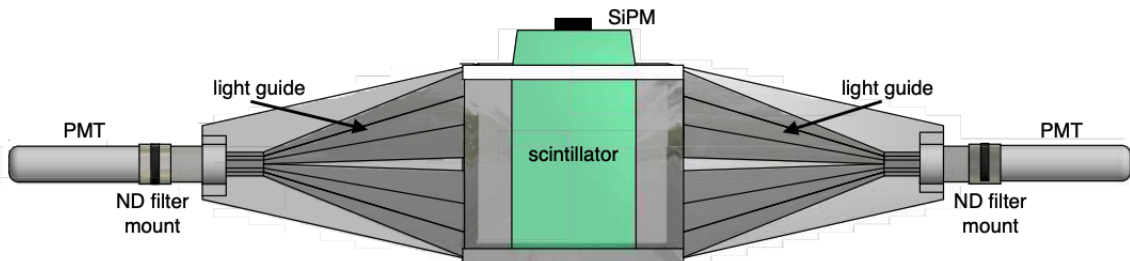


Figure 9.3: Diagram of the T0 detector [21]. Particles entering the ring pass through the scintillator (in green). Light guides on either side of the scintillator transport the scintillation light to the PMTs on each end.

is measured in time, and is the same as the longitudinal phase space coordinate ϕ . The z-axis is the intensity, or number of protons, again scaled by an arbitrary factor.

Ghost bunches can be seen bordering Batch 2 in the figure, and are thought to be a large contributor to out-of-time protons. There are many factors that could contribute to the out-of-time beam observed in Figure 9.1 and Figure 9.5. Further investigation with simulation and measurements performed closer to the Mu2e production target are necessary.



Figure 9.4: Picture of the T0 detector [21].

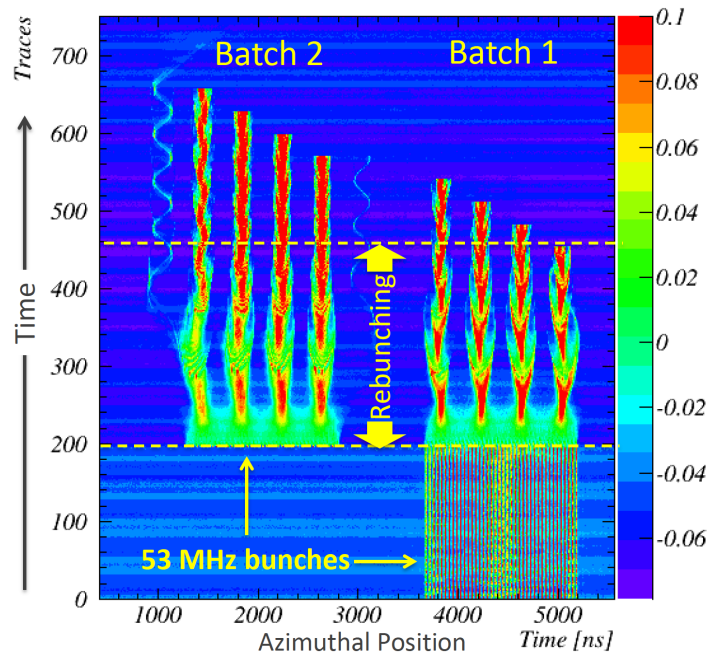


Figure 9.5: Waterfall plot showing the longitudinal time profile and intensity of proton bunches in the Recycler over time. Two batches consisting of four bunches each are present as well as additional “ghost” bunches that can be seen bordering Batch 2. While this bunch structure is satisfactory for g-2, it could potentially be detrimental to Mu2e [6].

9.2 Simulations

Major contributions to the out-of-time protons are caused by general limitations of the Fermilab accelerator complex such as frequency mismatch between the Booster and the Recycler, and by fundamental properties of all accelerators such as the machine impedance and space charge effects. Studies of the frequency mismatch as well as the machine

impedance will be presented here using a simulation framework called Beam Longitudinal Dynamics (BLonD) code [68]. Incorporating longitudinal impedance and space charge effects in the Recycler RF model is extremely important, because the Recycler has large longitudinal impedances at 2.5 MHz and 53 MHz. This type of study is the first of its kind to be done on the Recycler or any accelerator at the Fermilab complex using the BLonD framework.

9.2.1 Frequency Mismatch

The Booster has an RF frequency of 53 MHz and the Recycler has two RF systems one operating at the Booster frequency and one operating at 2.5 MHz. The Recycler must synchronously capture 21 53 MHz bunches into a 2.5 MHz bucket using an adiabatic voltage ramp depicted in Figure 9.6. Initially, the Booster bunches are injected into matched 53 MHz buckets. Then the 53 MHz voltage is switched off and the 2.5 MHz RF is turned on at 3 kV and adiabatically ramped to 80 kV over 90 ms. Adiabatic ramping minimizes the possibility of bunch rotations in mismatched 53 MHz and 2.5 MHz RF buckets [6].

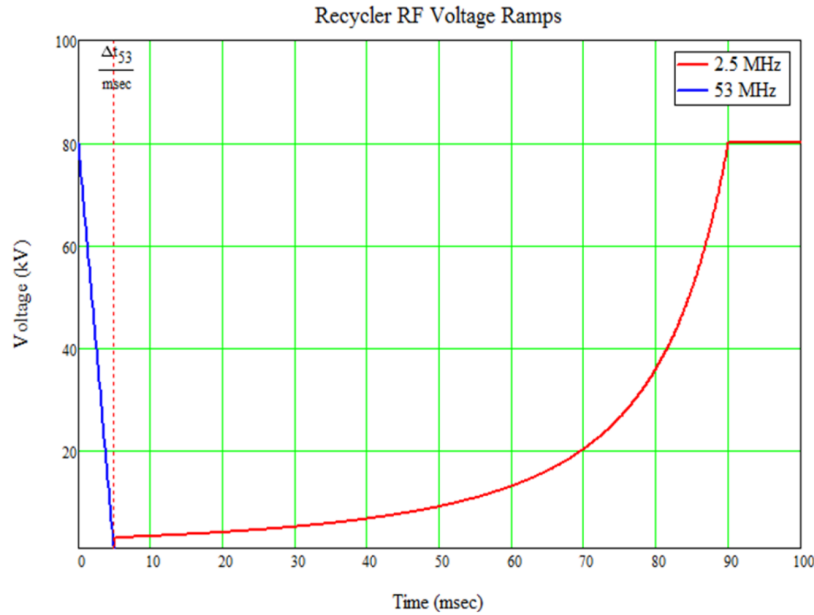


Figure 9.6: Re-bunching sequence of the Recycler [6].

Figure 9.7 shows the longitudinal phase space of the initial distribution from the Booster. This particle distribution was created using a python script that simulated

1,075,200 protons using a randomly generated gaussian distribution and the longitudinal equation for particle trajectories previously defined in Section 4.2.4. The momentum spread ($\Delta p/p$) is 1×10^{-3} , the harmonic number is 588 and the longitudinal emittance is 0.12 eVsec [6].

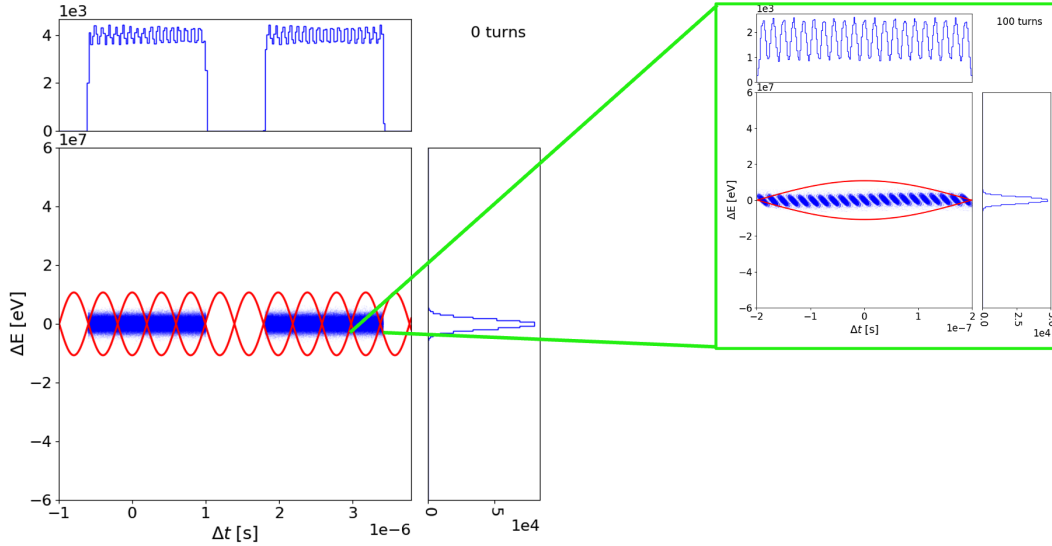


Figure 9.7: Initial distribution for input into the BLonD simulation of the Recycler. The green window depicts a zoomed in view of one 2.5 MHz bucket, the separatrix of which is drawn in red, where the individual 53 MHz Booster bunches can be discerned.

The 53 MHz bunches from the Booster are poorly matched to the 2.5 MHz buckets in the Recycler. This mismatch causes large deviations in the energy and phase of the particles. Particles at the center of the bucket experience a quicker rotation than those particles closer to the edge of the bucket. Due to the limited time window for the adiabatic re-bunching cycle, the beam never fully recovers until it is extracted from the DR. Figure 9.8 shows a simulation of one Recycler bunch in longitudinal phase space at a point in time after the re-bunching sequence of the 21 Booster bunches has taken place. This filamenting creates variations in the time distribution of the bunches that cause excess beam to extend outside the 250 ns window required for the in-time protons.

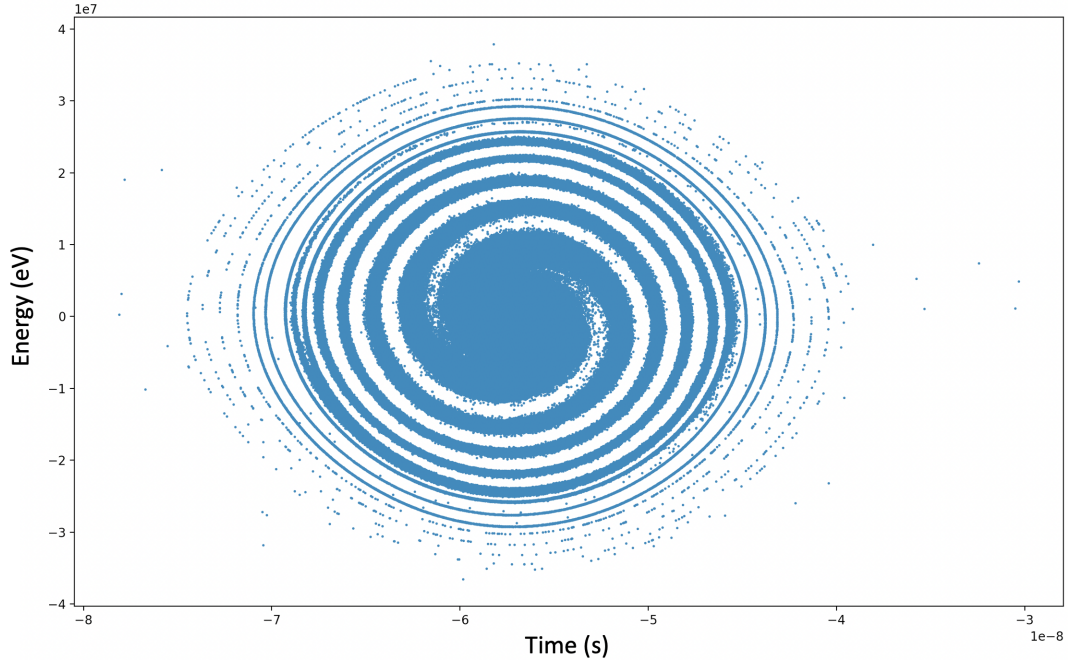


Figure 9.8: A view of the simulated eighth bunch in the Recycler in longitudinal phase space after the re-bunching sequence has been executed. In longitudinal phase space protons tend to rotate about the center of the RF bucket. Rotation near the center of the bucket is faster than that near the edge of the bucket. This gives rise to a filamenting of the beam in longitudinal phase space as the beam makes repeated revolutions around the bucket. This filamenting is clearly visible in the above plot.

9.2.2 Impedance and Space Charge

Direct space charge effects include coulomb interactions between particles of the same charge, and indirect space charge effects arise from the beams interaction with the surrounding beampipe and other conducting elements, which have been referred to here as impedance or collective effects. The indirect effect manifests as a decelerating voltage as the beam passes through the RF cavity [60].

In BLoND, space charge effects are calculated using a method that discretizes the beam into a large number of macroparticles, which represent groups of real particles. These macroparticles interact with each other and with the self-generated electric field.

The simulation begins by defining the initial distribution of macroparticles in the beam, including their positions, momenta, and charges as previously described. The electric field at a given point is the sum of the contributions from all macroparticles, taking into account

their positions, charges, and weights. The electric field obtained in the previous step is used to calculate the forces acting on each macroparticle. The forces are then used to update the momenta and positions of the macroparticles, simulating their motion in the electric field. The previous steps are repeated iteratively until a self-consistent solution is obtained [68].

In addition to the self-generated electric field, BLoND also considers the indirect effects or collective effects of the beam, such as wakefields and beam loading. While structures other than the RF cavities certainly contribute to longitudinal impedance effects, only the effects from the RF cavities are considered in the following simulations [60] [68].

BLoND allows the user to define the properties of the RF cavities. This includes specifying parameters such as the cavity geometry, resonant frequency, quality factor, and shunt impedance. These parameters for the Recycler’s 53 MHz cavities are displayed in Table 9.1. BLoND calculates the wakefield, which are a measure of the effect of the beam on the cavity’s electromagnetic fields, generated by the RF cavities. The wakefield can be divided into two components: the short-range or coherent wakefield, which decays rapidly with distance, and the long-range or incoherent wakefield. Based on the wakefield, BLoND calculates the complex impedance of the RF cavities. Again, BLoND takes into account the impedance forces by adding them to the forces already considered in the simulation, such as space charge forces and external fields. The particle trajectories and dynamics are then updated iteratively and accordingly [68].

Impedance measurements for the Recycler 53 MHz cavities are displayed in Table 9.1. Z_s is the shunt impedance which is best defined in the context of a circuit diagram that models the behavior of an RF cavity. Figure 9.9 shows this RLC circuit with the beam and driving current included. The shunt impedance is defined as the voltage across the cavity squared divided by the power dissipated,

$$Z_{shunt} = \frac{V_c^2}{P_{diss}} \quad (9.1)$$

At the resonant frequency of the cavity the impedance is purely resistive and equal to the shunt resistance, R_s . Q is a quantity previously mentioned that is the ratio of the power lost to energy stored, sometimes called the quality factor, that largely depends on

Frequency (MHz)	Q	Z_s (k Ω)	Q Correction	Z_s w/ Q Correction (k Ω)
52.893	6129.8	84.4635	6129.8	84.4635
155.227	1943.3	11.3495	10501	63.6447
250.38	1664.1	14.9947	13336.7	123.8602
337.217	3255.7	21.5207	15477.5	104.2822
429.016	5103.2	12.1914	17457.6	42.9785

Table 9.1: Recycler 53 MHz shunt impedance with Q correction [22].

the geometry of the RF cavity. Z_{shunt} with Q Correction or Z/Q does not depend on the power lost but instead is a purely geometrical factor. The value of Z_{shunt} with Q correction that was used for the 2.5 MHz cavity is 54 k Ω with a Q value of 120.

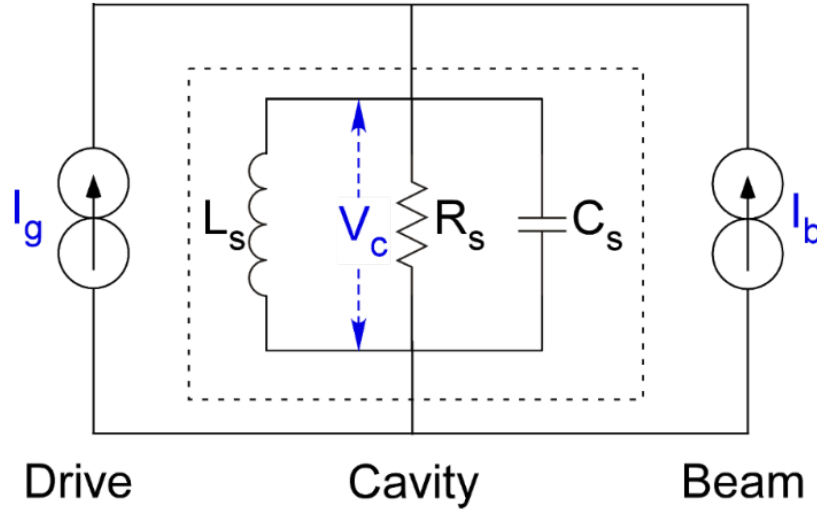


Figure 9.9: Circuit model for RF cavity including beam effects. The cavity presents itself as an RLC circuit that is excited by both the RF drive current (I_g) and the current induced by the beam (I_b). The shunt impedance of the cavity is characterized by an inductance, capacitance, and resistance given by L_s , C_s , and R_s respectively. For excitations at the resonant frequency the cavity impedance is only the resistance with $R_s = 84$ k Ω for 53 MHz. V_c is the resultant voltage across the cavity [6].

The effects of including impedance and space charge in the simulations can be seen in figures 9.10 and 9.11. The formation of ghost bunches can be clearly seen along side the two batches (each composed of four bunches), increasing the number of out-of-time

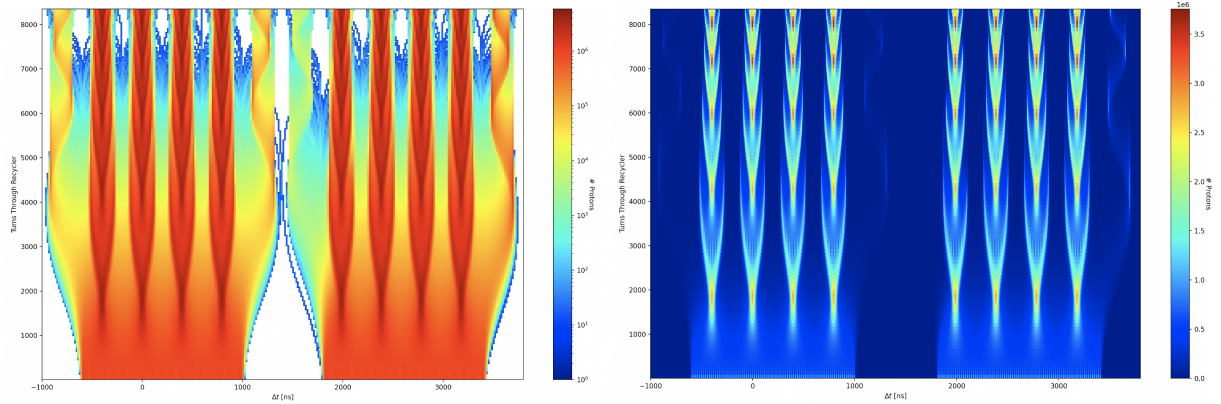


Figure 9.10: A simulation using BLoND of the re-bunching sequence in the Recycler with no space charge or impedance effects included. The y-axis is the number of turns through the Recycler, the x-axis is the longitudinal time coordinate and the z-axis is the number of protons. The z-axis on the right plot is on log scale and the left has a linear scale. Ghost bunches can be seen on either side of each batch which consists of 4 bunches.

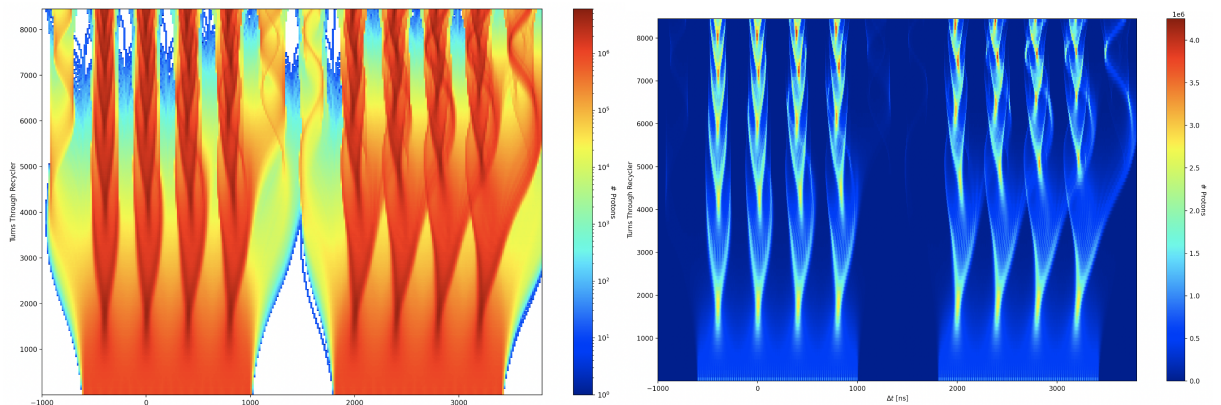
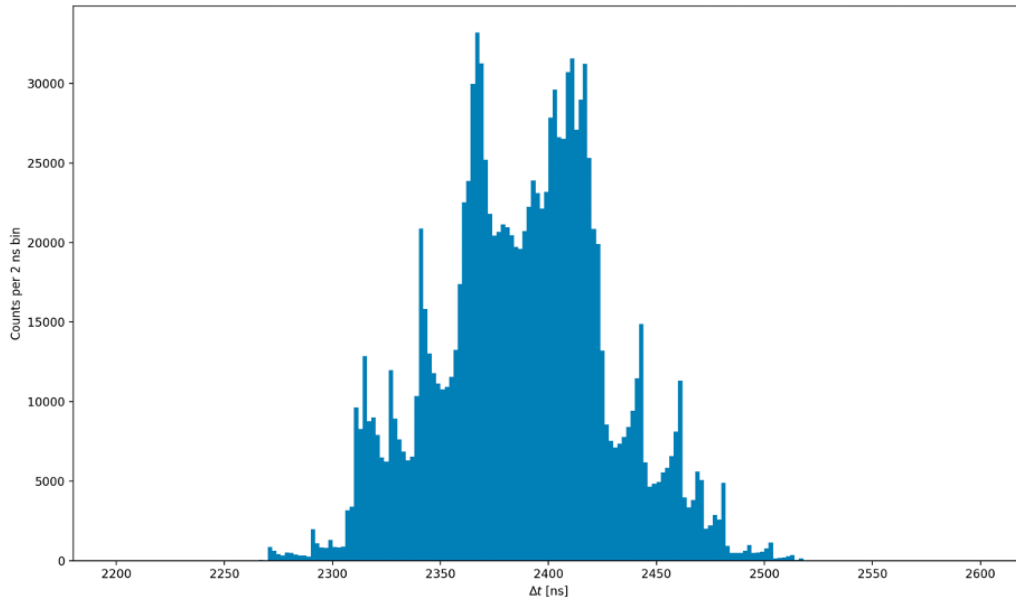


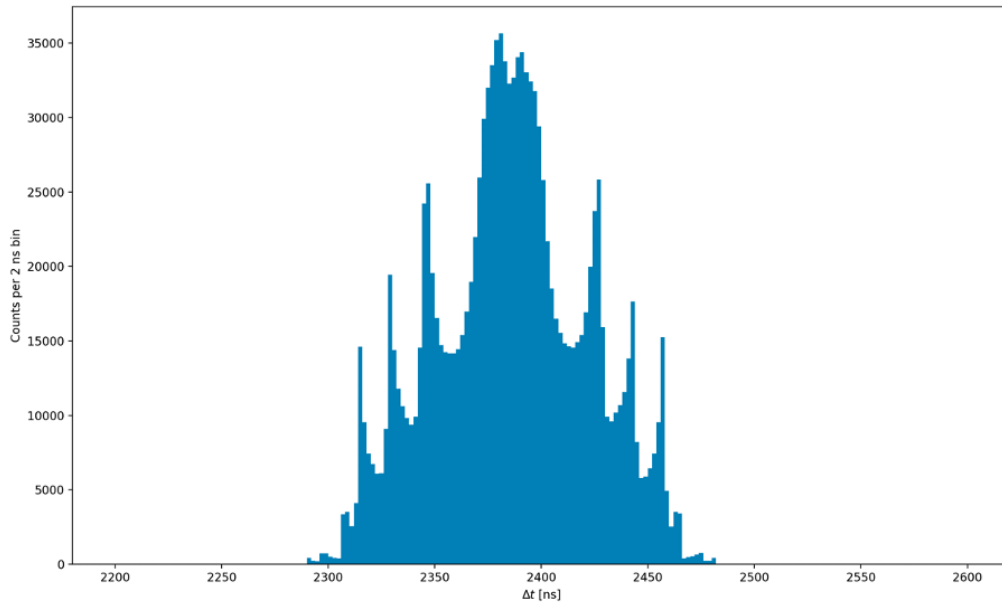
Figure 9.11: A simulation using BLoND of the re-bunching sequence in the Recycler with space charge and impedance effects included. Impedance was calculated using $6\times$ the shunt resistance. The y-axis is the number of turns through the Recycler, the x-axis is the longitudinal time coordinate and the z-axis is the number of protons. The z-axis on the right plot is on log scale and the left has a linear scale. Ghost bunches can be seen on either side of each batch which consists of 4 bunches.

protons significantly.

Figure 9.12 shows the longitudinal time profile of the eighth bunch of the simulated beam just prior to extraction from the Recycler to the Delivery Ring. At the end of the re-bunching cycle, the extinction level is simulated to be 2.01×10^{-4} , almost one order of magnitude above the requirement of 10^{-5} and two orders of magnitude higher than it would be without impedance and space charge effects included.



(a) Simulated extinction, with $6\times$ the measured shunt resistance as the impedance, as a function of time where $t = 2400$ ns is the center of the Recycler's RF bucket. The extinction level is 2.01×10^{-4} , an order of magnitude above the requirement for Mu2e.



(b) Simulated extinction, with no impedance, as a function of time where $t = 2400$ ns is the center of the Recycler's RF bucket. The extinction level is 10^{-6} , an order of magnitude below the requirement for Mu2e.

Figure 9.12: Histograms comparing the longitudinal time profile of the eighth bunch just prior to extraction. The y-axis has units of counts per 2 ns bin. As the impedance is increased, the irregular profile of the beam as well as increasing out-of-time beam are apparent.

The effects of the re-bunching cycle, impedance and space charge were described and results of simulations were presented here. While the extinction requirement of 10^{-5} is predicted to be out of reach for the Recycler due to these effects, future work simulating the Delivery Ring and making real measurements must be completed before conclusions can be made about achieving the full requirement.

9.3 M4DA Direct Measurement

The Mu2e experiment aims to observe the conversion of muons to electrons with as little interference from other particles as possible. The extinction monitor is a detector that will be located in the M4 diagnostic absorber line, pictured relative to the M4 line in Figure 9.13, that will measure the extinction level using an integration of many measurements over the course of the experiment. The extinction monitor will measure the background levels, from which the experiment will base the sensitivity measurement. It will also help optimize the operation of the extinction elements during the experiment in the M4 line by providing semi-real-time information about the beam structure and out-of-time beam. Ideally, the extinction monitor would provide single-event-sensitivity while maintaining a large dynamic range under bombardment from the full beam pulse of 10^7 protons. However, this is not a realistic scenario. Instead, the monitor will measure the beam outside of the primary proton pulse over several cycles of the experiment as a whole in order to gather enough statistics for the required sensitivity. The timescale for integration must be a few hours (much shorter than the actual duration of the experiment), hence semi-real-time, to prevent significant data loss due to an unexpected change in beam conditions or equipment failure.

A prototype of the monitor has been constructed recently to take preliminary bunch profile measurements. The prototype consists of three PMTs attached to an arm aligning them in a horizontal line, see Figure 9.14. The arm will be located behind a titanium vacuum window that will scatter the incoming charged particles into the quartz detectors. The PMTs will have quartz crystals mounted on them that will convert charged particles interaction with the medium into Cherenkov light. Figure 9.15 shows the shielding for the



Figure 9.13: Location of the M4 diagnostic absorber (M4DA) relative to the M4 line, which contains the extinction components including the AC Dipole [13].

PMT as well as how the crystals will be mounted on the detectors. This light will then be detected and the signal digitized by the PMTs and an oscilloscope. Quartz crystals are ideal for detecting fast charged particles with precision timing because the light produced is prompt and there is no afterglow, unlike many scintillating mediums [13].

Future work will include installation of the prototype arm in the M4DA. The resulting beam studies can be used to determine if the extinction level will be satisfactory for Mu2e, and if not, they can be used to determine potential solutions. In addition, the studies can be used to benchmark the simulations presented here.



Figure 9.14: The Upstream Extinction Monitor (UEM) prototype arm with mounted PMTs attached to quartz crystals [13].



(a) Square quartz crystal that will be used to detect charged particles for a beam profile measurement [13].



(b) PMT setup with metallic housing and quartz crystal mounted to an endcap. The item in the top of the picture is the metallic housing that will surround the PMT and the PMT with endcap is the bottom left item. The object on the bottom right is the had wrapped Tyvek crystal holder attached to an endcap [13].

Figure 9.15: Pictures of the detector setup that include a quartz crystal in Figure (a) and PMT with metallic housing and quartz crystal mount on an endcap in Figure (b).

Chapter 10

Conclusion

In summary, Mu2e will test the physics of flavor via the conversion process $\mu^- N \rightarrow e^- N$. This experiment pushes the boundaries of the intensity frontier and furthers the new physics potential using muon beams. Mu2e aims for $\times 10$ mass scale reach over existing experiments probing the same space, and 4 orders of magnitude advance on the conversion rate: $R_{\mu e}(Al) = 10^{-17}$ single-event-sensitivity as shown in Figure 2.1.

Theoretically, Mu2e covers a wide parameter space, setting it apart from some previous experiments that probed only loop level operators. Mu2e will allow experimenters to set limits on both the four-fermion operator and the dipole term shown in Equation 2.16. Even placing a limit on the parameter space using this conversion process will allow for great insight into existing theoretical models that extend the Standard Model.

Experimentally, Mu2e is lucky to be searching for a process with such a clean signature: a single electron at 104.973 MeV. Despite this, due to smearing and fake conversion signals from background processes, Mu2e must find ways to reduce prompt backgrounds which in the past have limited other experiments in the space. Section 3.1 outlines all of the backgrounds Mu2e must contend with. Some important backgrounds previously discussed are: electrons from RPC and electrons from muons/pions decaying in flight (μ/π - DIF) that can mimic the conversion signal. To achieve the lofty goal of a single-event-sensitivity of 10^{-17} , Mu2e has employed several novel techniques including a system of solenoids shown in Figure 3.6. The solenoids optimize the muon beam transport to accept only low energy, negative muons. The detectors are also specifically designed to be blind to muons

decaying in flight and to resolve the extremely fine experimental signature at ~ 105 MeV.

The success of the Mu2e Experiment hinges on a concept called “Extinction”, explained in depth in Chapter 6. Extinction is defined as the ratio of the number of protons outside the nominal 250 ns wide proton pulse to the number of protons inside the proton pulse shown in Figure 5.9. Keeping this fraction at or below the 10^{-10} level is a major requirement driving the main subject of this thesis.

The majority of the extinction process takes place in the M4 beam line, shown in Figure 5.8, located just before the muon production target. Two collimators and an AC dipole system will reduce the extinction level seven orders of magnitude to achieve the final goal of 10^{-10} . The AC dipole is the main feature of the extinction system. It consists of two dipole magnets, one operating at 300 kHz and one at 4.4 MHz. The repetition rates of the magnets has previously been a cause for concern, as the magnetic material, conventional or otherwise was found to heat excessively at these frequencies. Extensive studies and magnetic modeling have been performed for the ferrite material in question. In the work presented in Chapter 8, quality analysis tests were used to validate simulation results as well as choose a suitable magnetic material for the Mu2e experiment’s purposes.

The remaining reduction in the extinction level must be produced by the natural process of bunch formation in the accelerator complex upstream of the M4 beam line. Measurements of the current extinction level in the Recycler Ring can be estimated with temporal bunch data from the g-2 experiment that can be seen in Figure 9.1. While there are notable differences in the beam intensities between the g-2 experiment and the Mu2e experiment, the timing structure of the bunches are comparable. The data taken by the T0 detector, indicates an out of time fraction well above the 10^{-5} level expected at this point in the bunch formation process. Much of the out-of-time beam during the formation of bunches is due to collective effects and machine impedance effects introduced in Section 4.2 and further discussed and studied in Chapter 9. Chapter 9 presents original work using the Beam Longitudinal Dynamics (BLonD) code framework that for the first time models and compares the effects of machine impedance and space charge in the Fermilab Recycler. The culmination of these effects can most readily be seen by inspecting Figures 9.10 and

9.11. Specifically, using the concepts developed by [6] with the ESME framework, this work was able to verify that collective effects have a large bearing on beam loss and bunch formation as a whole in the Fermilab Recycler. Further development of the simulation presented here as well as a more robust experimental benchmark will make this analysis indispensable to the success of Mu2e and future intensity experiments at Fermilab.

REFERENCES

- [1] A. Perrevoort, “Searching for lepton flavour violation with the mu3e experiment,” 2018. [Online]. Available: <https://arxiv.org/abs/1802.09851>
- [2] L. Bartoszek and *et al.*, “Mu2e technical design report,” 2014, arXiv:1501.05241.
- [3] A. Czarnecki, X. Garcia i Tormo, and W. J. Marciano, “Muon decay in orbit: Spectrum of high-energy electrons,” *Phys. Rev. D*, vol. 84, p. 013006, Jul 2011. [Online]. Available: <https://link.aps.org/doi/10.1103/PhysRevD.84.013006>
- [4] E. Prebys, “Mu2e: Search for muon to electron conversion at fermilab,” 2017.
- [5] R. Bernstein, “The mu2e experiment,” *Frontiers in Physics*, vol. 7, 2019. [Online]. Available: <https://www.frontiersin.org/article/10.3389/fphy.2019.00001>
- [6] S. Werkema, “Mu2e proton beam longitudinal structure,” <http://mu2e-docdb.fnal.gov>, 2018, mu2e-doc-2771.
- [7] E. Prebys, “Motion in solenoids,” 2023.
- [8] M. T., “Presentation at 51st annual fermilab users meeting,” 2018. [Online]. Available: <https://indico.fnal.gov/event/16332/session/5/contribution/17/material/slides/0.pdf>
- [9] B. J. Holzer, “Introduction to transverse beam dynamics,” 2014. [Online]. Available: <http://cds.cern.ch/record/1693320>
- [10] D. A. Edwards and M. J. Syphers, *An Introduction to the Physics of High Energy Accelerators*. Wiley, 1993.
- [11] e. Welton, Robert, “Negative hydrogen ion sources for particle accelerators: Sustainability issues and recent improvements in long-term operations,” *Journal of Physics. Conference Series*, vol. 2244, no. 1, 4 2022.
- [12] S. Nagaitsev, “Fermilab antiproton source, recycler ring, and main injector,” 2014.
- [13] S. Boi, “Upstream extinction monitor (aka precision time profile monitor),” 5 2023, mu2e Collaboration Meeting, Extinction Monitor Workshop.
- [14] W. A. Barletta, “Beam loading,” 2009. [Online]. Available: https://uspas.fnal.gov/materials/09UNM/Unit_6_Lecture_13_Beam_loading.pdf
- [15] E. Prebys and S. Werkema, “Out of Time Beam Extinction in the Mu2e Experiment,” in *Proc. 6th International Particle Accelerator Conference (IPAC’15), Richmond, VA, USA, May 3-8, 2015*, ser. International Particle Accelerator Conference, no. 6. Geneva, Switzerland: JACoW, June 2015, paper THPF121, pp. 3996–3999, <https://doi.org/10.18429/JACoW-IPAC2015-THPF121>. [Online]. Available: <http://jacow.org/ipac2015/papers/thpf121.pdf>

- [16] E. J. Prebys and S. Werkema, “Out-of-time beam extinction in the mu2e experiment,” 6 2015. [Online]. Available: <https://www.osti.gov/biblio/1250511>
- [17] C. J. G. K. K. H. H. P. E. P. D. S. I. T. L. Elementi, C. Comino, “High frequency ni-zn ferrite characterization for mu2e ac-dipole magnet,” 2019.
- [18] I. Terechkine, “Extinction ac dipole system crr4: Interpretation of permeability measurements made using available material samples,” <http://mu2e-docdb.fnal.gov>, 2019, mu2e-doc-26439.
- [19] B. Casey, personal communication.
- [20] J. Grange and *et. al.*, “Muon (g-2) technical design report,” 2018.
- [21] H. Binney, “Muon g-2 experiment: first results and future prospects,” 2021, rising Star Symposium.
- [22] J. Dey, personal communication.
- [23] V. Shiltsev, “Considerations on energy frontier colliders after lhc,” 2017. [Online]. Available: <https://arxiv.org/abs/1705.02011>
- [24] S. Abachi and *et. al.*, “Observation of the top quark,” *Physical Review Letters*, vol. 74, no. 14, pp. 2632–2637, apr 1995. [Online]. Available: <https://doi.org/10.1103%2Fphysrevlett.74.2632>
- [25] F. Abe and *et. al.*, “Observation of top quark production in pbar-p collisions,” *Physical Review Letters*, vol. 74, no. 14, pp. 2626–2631, apr 1995. [Online]. Available: <https://doi.org/10.1103%2Fphysrevlett.74.2626>
- [26] S. W. Herb, D. C. Hom, Lederman, and *et. al.*, “Observation of a Dimuon Resonance at 9.5 GeV in 400-GeV Proton-Nucleus Collisions,” , vol. 39, no. 5, pp. 252–255, Aug. 1977.
- [27] C. Campagnari and M. Franklin, “The discovery of the top quark,” *Reviews of Modern Physics*, vol. 69, no. 1, pp. 137–212, jan 1997. [Online]. Available: <https://doi.org/10.1103%2Frevmodphys.69.137>
- [28] S. Chatrchyan and *et. al.*, “Observation of a new boson at a mass of 125 GeV with the CMS experiment at the LHC,” *Physics Letters B*, vol. 716, no. 1, pp. 30–61, sep 2012. [Online]. Available: <https://doi.org/10.1016%2Fj.physletb.2012.08.021>
- [29] G. Aad and *et. al.*, “Observation of a new particle in the search for the standard model higgs boson with the ATLAS detector at the LHC,” *Physics Letters B*, vol. 716, no. 1, pp. 1–29, sep 2012. [Online]. Available: <https://doi.org/10.1016%2Fj.physletb.2012.08.020>

- [30] U. D. of Energy. Energy frontier experiments. [Online]. Available: <https://science.osti.gov/hep/Research/Energy-Frontier/Experiments#:~:text=Energy%20Frontier%20researchers%20accelerate%20particles,the%20architecture%20of%20the%20universe.>
- [31] A. Abada and *et. al.*, “He-lhc: The high-energy large hadron collider,” *Eur. Phys. J. Spec. Top.*, vol. 228, pp. 1109–1382, jul 2019. [Online]. Available: <https://doi.org/10.1140/epjst/e2019-900088-6>
- [32] Davidson and *et. al.*, “Charged lepton flavor violation,” 2022. [Online]. Available: <https://arxiv.org/abs/2209.00142>
- [33] A. Bellerive and *et al.*, “The sudbury neutrino observatory,” *Nuclear Physics B*, vol. 908, pp. 30–51, jul 2016. [Online]. Available: <https://doi.org/10.1016%2Fj.nuclphysb.2016.04.035>
- [34] Y. Fukuda and *et. al.*, “Evidence for oscillation of atmospheric neutrinos,” *Physical Review Letters*, vol. 81, no. 8, pp. 1562–1567, aug 1998. [Online]. Available: <https://doi.org/10.1103%2Fphysrevlett.81.1562>
- [35] S. Abe and *et. al.*, “Precision measurement of neutrino oscillation parameters with kamland,” *Physical Review Letters*, vol. 100, no. 22, Jun. 2008. [Online]. Available: <http://dx.doi.org/10.1103/PhysRevLett.100.221803>
- [36] Y. Kuno and *et. al.*, “Muon decay and physics beyond the standard model,” *Rev. Mod. Phys.*, vol. 73, pp. 151–202, Jan 2001. [Online]. Available: <https://link.aps.org/doi/10.1103/RevModPhys.73.151>
- [37] J. Adam and *et. al.*, “New constraint on the existence of the $\mu^+ \rightarrow e^+ \gamma$ decay,” *Phys. Rev. Lett.*, vol. 110, p. 201801, May 2013. [Online]. Available: <https://link.aps.org/doi/10.1103/PhysRevLett.110.201801>
- [38] U. Bellgardt and *et al.* (SINDRUM Collaboration), *Nucl. Phys.*, vol. B299, 1988.
- [39] A. Baldini and *et al.*, “The design of the meg ii experiment,” *Eur. Phys. J. C*, vol. 78, pp. 1434–6052, 2018. [Online]. Available: <https://doi.org/10.1140/epjc/s10052-018-5845-6>
- [40] A. Blondel and *et. al.*, “Research proposal for an experiment to search for the decay $\mu \rightarrow eee$,” 2013. [Online]. Available: <https://arxiv.org/abs/1301.6113>
- [41] W. Bertl and *et al.*, “A search for $\mu - e$ conversion in muonic gold,” *Eur. Phys. J. C*, vol. 47, p. 337–346, 2006.
- [42] C. Dohmen and *et. al.*, “Test of lepton-flavour conservation in $\mu \rightarrow e$ conversion on titanium,” *Physics Letters B*, vol. 317, no. 4, pp. 631–636, 1993. [Online]. Available: <https://www.sciencedirect.com/science/article/pii/037026939391383X>

- [43] Honecker and *et al.*, “Improved limit on the branching ratio of $\mu \rightarrow e$ conversion on lead,” *Phys. Rev. Lett.*, vol. 76, pp. 200–203, Jan 1996. [Online]. Available: <https://link.aps.org/doi/10.1103/PhysRevLett.76.200>
- [44] Y. Kawamura, “Yukawa interactions, flavor symmetry, and non-canonical Kähler potential,” *Progress of Theoretical and Experimental Physics*, vol. 2019, no. 4, 04 2019, 043B05. [Online]. Available: <https://doi.org/10.1093/ptep/ptz018>
- [45] Particle Data Group, “Review of particle physics,” *Progress of Theoretical and Experimental Physics*, vol. 2020, no. 8, 08 2020, 083C01. [Online]. Available: <https://doi.org/10.1093/ptep/ptaa104>
- [46] T. K. Collaboration, “Direct neutrino-mass measurement with sub-electronvolt sensitivity,” *Nature Physics*, vol. 18, pp. 160 – 166, 2022. [Online]. Available: <https://doi.org/10.1038/s41567-021-01463-1>
- [47] K. Assamagan and *et. al.*, “Upper limit of the muon-neutrino mass and charged-pion mass from momentum analysis of a surface muon beam,” *Phys. Rev. D*, vol. 53, pp. 6065–6077, Jun 1996. [Online]. Available: <https://link.aps.org/doi/10.1103/PhysRevD.53.6065>
- [48] R. Barate and *et al.* (ALEPH Collaboration), “An upper limit on the τ neutrino mass from three- and five-prong tau decays,” *Eur. Phys. J. C*, vol. 2, p. 395–406, 1998. [Online]. Available: <https://doi.org/10.1007/s100529800850>
- [49] Y. Farzan and M. Tórtola, “Neutrino oscillations and non-standard interactions,” *Frontiers in Physics*, vol. 6, 2018. [Online]. Available: <https://www.frontiersin.org/articles/10.3389/fphy.2018.00010>
- [50] J. L. Diaz-Cruz, “The supersymmetric flavor problem,” *AIP Conference Proceedings*, vol. 917, no. 1, pp. 277–284, 2007. [Online]. Available: <https://aip.scitation.org/doi/abs/10.1063/1.2751967>
- [51] A. de Gouvea and P. Vogel, “Lepton Flavor and Number Conservation, and Physics Beyond the Standard Model,” *Prog. Part. Nucl. Phys.*, vol. 71, pp. 75–92, 2013.
- [52] A. M. Baldini and *et al.*, “Meg upgrade proposal,” arXiv:1301.7225v2.
- [53] R. M. Dzhilkibaev and V. M. Lobashev, “On the search for the $\mu \rightarrow e$ conversion process in a nucleus,” *Soviet Journal of Nuclear Physics (English Translation); (USA)*, vol. 49:2, 2 1989. [Online]. Available: <https://www.osti.gov/biblio/5665919>
- [54] M. Kargiantoulakis, “A search for charged lepton flavor violation in the mu2e experiment,” *Modern Physics Letters A*, vol. 35, no. 19, p. 2030007, Apr. 2020. [Online]. Available: <http://dx.doi.org/10.1142/S0217732320300074>
- [55] Y. Kuno and *et al.*, “Comet proposal,” 2007.

- [56] J. Miller, “Beam extinction requirement for mu2e,” <http://mu2e-docdb.fnal.gov>, 2014, mu2e-doc-1175.
- [57] E. Prebys, L. Bartoszek, A. Gaponenko, and P. Kasper, “Beam extinction monitoring in the mu2e experiment,” in *6th International Particle Accelerator Conference*, 2015, p. MOPWI017.
- [58] H. Chiang, E. Oset, T. Kosmas, A. Faessler, and J. Vergados, “Coherent and incoherent (μ^- , e^-) conversion in nuclei,” *Nuclear Physics A*, vol. 559, no. 4, pp. 526–542, 1993. [Online]. Available: <https://www.sciencedirect.com/science/article/pii/037594749390259Z>
- [59] L. Bartoszek and *et al.*, “Mu2e crv review,” 2015.
- [60] E. Metral, G. Rumolo, and W. Herr, “Impedance and Collective Effects,” pp. 105–181, 2020. [Online]. Available: <https://cds.cern.ch/record/2743945>
- [61] F. Tecker, “Longitudinal beam dynamics in circular accelerators,” 2020.
- [62] D. C. Faircloth, “Negative ion sources: Magnetron and penning,” 2014. [Online]. Available: <http://cds.cern.ch/record/1693328>
- [63] B. Worthel and *et. al.*, “Linac rookie book v2.3,” 2004. [Online]. Available: https://operations.fnal.gov/rookie_books/LINAC_RB_v2_3.pdf
- [64] ———, “Booster rookie book v4.1,” 2009. [Online]. Available: https://operations.fnal.gov/rookie_books/Booster_V4.1.pdf
- [65] R. Ainsworth and *et. al.*, “High intensity operation using proton stacking in the fermilab recycler to deliver 700 kw of 120 gev proton beam,” vol. 23, p. 121002, Dec 2020. [Online]. Available: <https://link.aps.org/doi/10.1103/PhysRevAccelBeams.23.121002>
- [66] M. T. Jones, “Resonant extraction and extinction measurement for the mu2e experiment,” *PoS*. [Online]. Available: <https://www.osti.gov/biblio/1839568>
- [67] E. Prebys, “Optimization of ac dipole parameters for the mu2e extinction system,” in *Proc. International Particle Accelerator Conference 2012 (New Orleans, Louisiana, USA, 2012)*, 2012, pp. 2714–2716. [Online]. Available: <http://accelconf.web.cern.ch/AccelConf/IPAC2012/papers/WEPPD081.PDF>
- [68] “Beam longitudinal dynamics code (blond),” <http://blond-admin.github.io/BLonD/>.
- [69] D. Stratakis, M. E. Convery, J. P. Morgan, M. J. Syphers, M. Korostelev, A. Fiedler, S. Kim, J. D. Crnkovic, and W. M. Morse, “Towards commissioning the fermilab muon g-2 experiment,” 2018.